The Mechanistic Basis of Dynein Microtubule Binding and Its Regulation

The mechanistic basis of dynein microtubule binding and its regulation

A dissertation presented

by

Sirui Zou

to

Department of Chemistry and Chemical Biology

In partial fulfillment of the requirements

for the degree of

Doctor of Philosophy

In the subject of

Chemistry

Harvard University

Cambridge, Massachusetts

November 2014

Dissertation Advisor: Samara Reck-Peterson Sirui Zou

The mechanistic basis of dynein microtubule binding and its regulation

Abstract

Eukaryotic cells use a diverse toolbox of cytoskeletal motors to transport and position cellular materials in space and time. Two microtubule-based motors—kinesin and dynein—transport organelles, RNA and protein cargos over long-distances. While multiple kinesin motors are used for long-distance plus-end-directed transport, a single type of dynein—cytoplasmic dynein 1— performs nearly all minus-end-directed tasks. Despite cytoplasmic dynein's role in such diverse activities, many aspects of its molecular mechanism remain poorly understood. My thesis work uses a combination of cryo-electron microscope (EM) structural biology and single-molecule approaches to provide novel insights into the mechanistic basis of how dynein interacts with its microtubule track and how microtubule binding is regulated by the ubiquitous co-factor, Lis1.

First, we solved a 9.7A structure of dynein's microtubule binding domain bound to microtubules. This structure allowed us to identify large conformational changes that occur in dynein's microtubule-binding domain upon track binding. We hypothesize that these conformational changes allosterically regulate the ATP hydrolysis cycle in dynein's motor domain, which is located over 25 nm from

the site of microtubule binding. Molecular dynamics simulations, followed by single-molecule assays, allowed us to identify dynamic salt bridge switches in dynein, which can tune its affinity for the microtubule. The native dynein, which has been selected for submaximal processivity, might allow a broader dynamic range for regulation.

Second, we identified how dynein is regulated by its ubiquitous co-factor, Lis1. Our three-dimensional cryo-EM structures of the dynein-Lis1 complex showed dynein's mechanical element, the linker, is in an altered position in the presence of Lis1. Fluorescence resonance energy transfer (FRET) and single-molecule studies indicated that Lis1 binding to dynein sterically blocks the dynein linker from reaching its normal docking site, which may interrupt dynein's mechanochemical cycle and prevent its release from microtubules.

Table of Contents

List of Figures

List of Tables

Acknowledgement

As the long journey of my graduate research is near the end, I would like to extend my great appreciation to my mentors, colleagues, friends and family. Without their support and contributions, my journey would not have been so enjoyable and rewarding.

Dr. Guangzhao Zhang from University of Science and Technology of China is my undergraduate research mentor. In his lab, I started to learn what is research. After studying polymer folding, I became very interested in proteins and biology. How do proteins fold? What is the relationship between their structures and functions? With Dr. Zhang's encouragement, my interest in science became a concrete desire to be a scientist and decided to pursue a PhD degree in the United States.

Department of Chemistry and Chemical Biology at Harvard University provided me with this great opportunity to work with frontier science and smart people. The department also supported me with great freedom and generous funding when I re-considered my interest and decided to switch labs. Especially, I would like to thank, the department director, Allen Alloise, who has been always very helpful in coordinating and making my transition smooth. I also owe my thanks to the faculty members of my Graduate Advising Committee (GAC), Adam Cohen, David Pellman and Joseph Loparo, who offered critical feedback and support to my projects.

My colleagues from the Reck-Peterson lab are always very supportive, inspiring and pleasant to work with. Everyone has their own expertise, and is

always willing to help. Weihong Qiu introduced me into this wonderful group and taught me a lot of knowledge in microscopy and yeast genetics. I also enjoyed and benefited a lot from discussions with Anthony Roberts. Meanwhile, I also closely collaborated with Kat Toropova, Bret Redwine, and Rogelio Hernandez-Lopez from Dr. Andres Leschziner's lab, where we were able to combine structural biology, biophysics and biochemistry to tackle complex questions.

Importantly, I would like to thank my angel advisor, Sam Reck-Peterson. I met Sam at my most difficult time in the graduate school. She restored the interest and confidence in science back into me. By working with her, I learned how to do science, and more importantly, how to enjoy science. Sam is extremely helpful and supportive in all aspects, not only my research, but also improving my writing and presentations. Sam is not only my supervisor, but also my colleague, my friend and my role model.

My wonderful friends are always on my side, encouraging, comforting, supporting and inspiring me. Lu Wang and Xiaojie Duan are my "girlfriends" at Harvard, with who I share happy and sad moments throughout my PhD time. In earlier years of my PhD, I was closely working with Ping Xie, Bozhi Tian, and Xiaocheng Jiang, from whom I learned a lot in nanoscience. When I switched to biology, I often acquired inspiration by discussing with Zhen Shi, Jiang He, Jie Quan, Meisheng Lau, Wen Zhou, Liya Ding, Wei Wang. Moreover, I would like to thank my long-time friends, Huizhi Bao, Yan Liu, Jun Huang, who I have known from my high school and college time. They are always there to share ups and downs with me as a strong backing.

In the end, I would like to thank my wonderful family members—my dad, Peilin Zou, and my mom, Meiyu Du, as well as my maternal grandma, and paternal grandparents. Although I can't visit and take care of them very often, they are always there, supporting me with their endless understanding, encouragement and help. So I want to say, "I love you."

Chapter 1 : Introduction

Sirui Zou

The microtubule cytoskeleton

The cytoskeleton is a cellular skeleton in the cytoplasm of the cell. It provides internal support for the cell to maintain or change its shape. It also serves as a roadway to position and deliver intracellular components (organelles, proteins, and nuclei acids) to their destinations when the cell grows, divides and moves. The cytoskeleton and its associated proteins—including motor proteins—orchestrate these processes with spatial and temporal precision and high efficiency (Vale, 2003). Actin filaments and microtubules are two types of cytoskeletal tracks: short-range movements are mostly actin-based and near the plasma membrane; long-range transport occurs primarily along microtubules throughout the cell (Fig. 1.1A&B). In this dissertation, I will focus on the microtubule-based cytoskeleton.

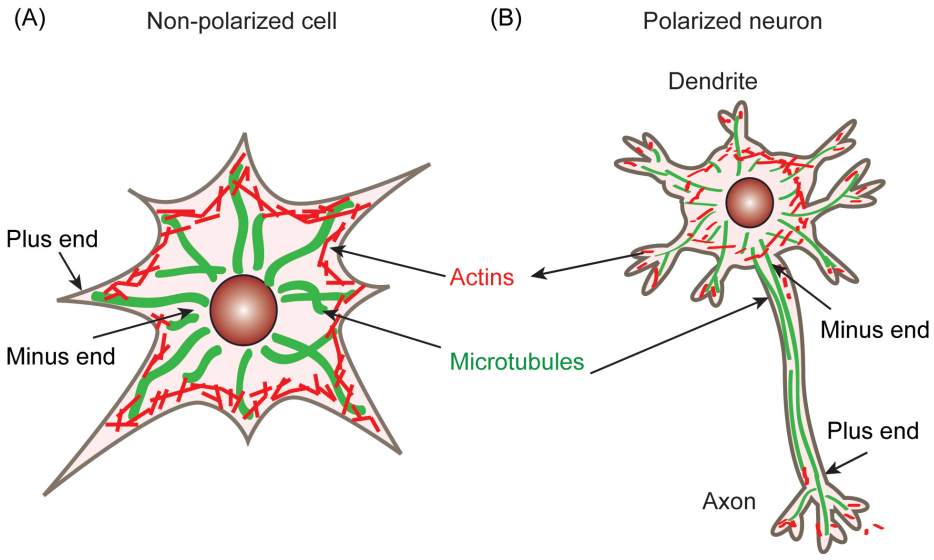

Figure 1.1 The cytoskeleton
(A) In non-polarized cells, actin filaments (red) are mostly concentrated in the cell cortex underlying the cell membrane, while microtubules (green) radiate outwards from the center of the cell to its periphery. **(B)** In polarized neurons, microtubules have a uniform directionality in axons, but mixed directionality in dendrites. Adapted from Fig. 1 of (Goodman et al., 2012).

Microtubules are long—up to tens of micrometers—and hollow tubes with an outer diameter of ~25 nm and an inner diameter of ~12 nm (Fig. 1.2). The basic unit is a heterodimer of α- and β-tubulin. The dimers polymerize into a long strand end-to-end (…αβαβαβ…), which is called a protofilament. Thirteen to fifteen protofilaments assemble side-by-side into a microtubule (Nogales, 2000) (Fig. 1.2). Moreover, the carboxyl-terminal tails (E-hooks) of αβ-tubulins are highly acidic. These disordered tails—at the outer surface of the microtubule—are exposed to diverse post-translational modifications, such as acetylation, phosphorylation, and polyglutamylation, which affect the interaction with associated proteins and provide the microtubule with functional diversity (Westermann and Weber, 2003; Sirajuddin et al., 2014). The microtubule has two notable properties. First, it has a distinct structural polarity. The α-tubulin-exposed end grows slower, called the minus end, while the β-tubulin-exposed end grows much faster, called the plus end. Microtubules are nucleated at microtubule-organizing centers (MTOCs) (called the spindle pole body in *S. cerevisiae*) near the nucleus and radiate out into the cytoplasm with their plus-ends near the periphery of the cell (Fig. 1.1A) (Mitchison et al., 1986). In more polarized neurons, axonal microtubules uniformly have their plus ends facing the axon tips and minus ends facing the cell body, while microtubules have mixed directions in dendrites (Fig. 1.1B) (Conde and Cáceres, 2009). Second, microtubules dynamically switch between growing and shrinking at their plus ends, which is called dynamic instability (Fig. 1.2). This is an emergent property of the GTP hydrolysis kinetics in β-tubulin, as the GTP- and GDP-bound forms

have different dissociation rates from the microtubule plus end (Mitchison and Kirschner, 1984). Microtubule dynamics are regulated by associated proteins *in vivo* (Nogales, 2000) and small molecules such as taxol *in vitro* (Xiao et al., 2006). Recent cryo-electron microscopy revealed the molecular differences found in dynamic microtubules (GDP-bound) versus stable microtubules (GTP-bound in the presence of taxol (Alushin et al., 2014).

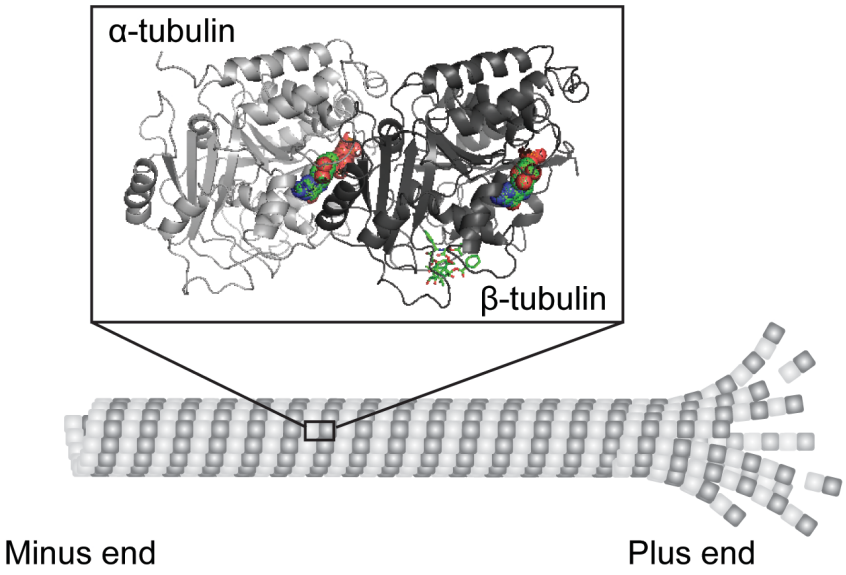

Figure 1.2 The structure of the microtubule
Microtubules are formed from heterodimers of α- (light gray) and β- (dark gray) tubulin (PDB ID: 1TUB). They consist of 13-15 protofilaments. GTP and GDP molecules (sphere mode) are bound to α- and β-tubulin, respectively. The more dynamic and outward-curved end is the plus end of the microtubule, and the other end is the minus end. A taxol molecule (stick mode) is bound to β-tubulin. Adapted from Fig. 1 of (Goodman et al., 2012).

As a result of the above properties, microtubules play important roles. During mitosis, microtubules, together with MTOCs and microtubule-associated proteins (MAPs), form the mitotic spindle, which pulls chromosomes to segregate into two daughter cells. When cells—especially polarized cells—migrate,

microtubules are asymmetrically distributed and regulated to affect cell protrusion and adhesion in making a leading edge (Etienne-Manneville, 2013). More importantly and relevantly in this dissertation, microtubules function as a track system for motor proteins to deliver cellular cargo to their proper destinations (Vale, 2003) .

Microtubule-based motor proteins: kinesin and dynein

Two families of motor proteins—kinesins and dyneins—walk along microtubules. They convert the chemical energy of ATP into mechanical movement. Most kinesins walk towards the plus end of the microtubule (towards the cell periphery), while dyneins walk in the opposite direction, towards the minus end (towards the cell center) (Fig. 1.3A). They are both involved in organelle positioning, cargo transport (Vale, 2003) and mitosis (Sharp et al., 2000). Despite some functional similarities and sharing the same microtubule track, dynein and kinesin are very different motors.

The kinesin superfamily is larger than the dynein superfamily. Forty-five mammalian kinesin genes have been identified in humans (Hirokawa et al., 2009; Miki et al., 2001). Alternative mRNA slicing generates additional kinesin isoforms (Cyr et al., 1991). Most kinesins transport cargo towards the plus end of the microtubule, but other kinesins can depolymerize or slide microtubules. There are fifteen dynein motor genes in the human genome (Yagi, 2009). However, most of these are involved in generating the beating motions of cilia and flagella,

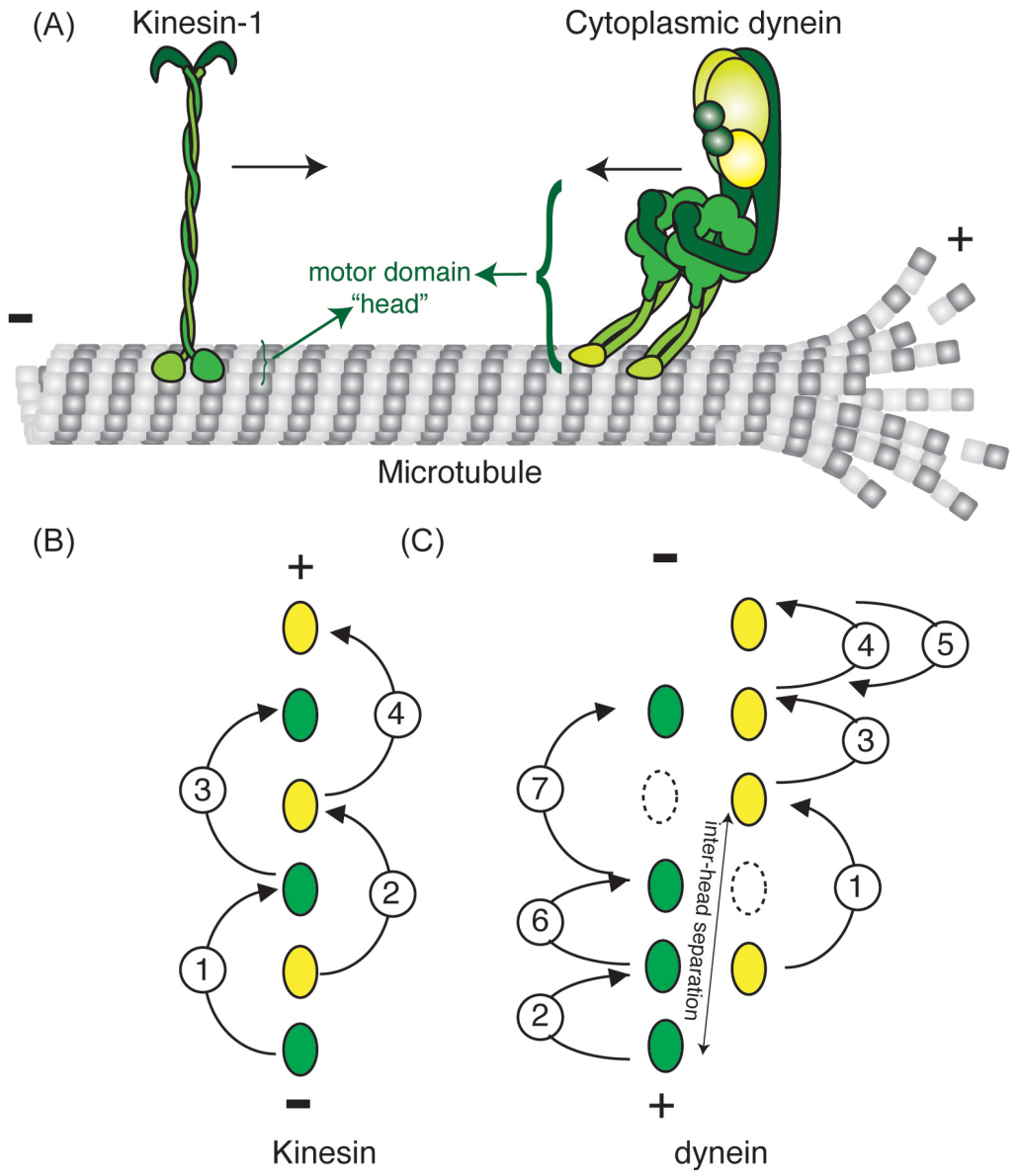

Figure 1.3 Kinesin and dynein are distinct motors
(A) Most kinesins, such as kinesin-1, walk towards the plus end of the microtubule, while cytoplasmic dynein walks towards the minus end. Kinesin has a more compact motor domain than dynein. (Adapted from Fig. 1 of (Goodman et al., 2012)). **(B)** Kinesin's hand-over-hand stepping on a single protofilament. One head (green) always follows the other head (yellow) to step and pass the other (Yildiz et al., 2004). The order of steps is shown in numbers. **(C)** Dynein's uncoordinated stepping on neighboring protofilaments includes larger steps (steps 1) and backwards steps (step 5). Dynein's two heads alternate more frequently when the head-to-head distance increases and sometimes step to neighboring protofilaments (not shown in the Fig.) (Fig. 1.2C) (DeWitt et al., 2012; Qiu et al., 2012). Adapted from Fig. 2 of (Kikkawa, 2013).

or performing transport within cilia and flagella. In contrast, there is only one gene copy of cytoplasmic dynein 1 (referred to here as 'cytoplasmic dynein' or 'dynein'), which powers almost all minus-end-directed motility in the cytoplasm. To achieve its many functions, cytoplasmic dynein must be highly regulated (Kardon and Vale, 2009; Vallee et al., 2012).

Dynein is larger and more complex than kinesin (Fig. 1.3A). Kinesin has two heavy chains and two light chains (molecular weight: ~380 kDa) (Hirokawa, 1998), while dynein has two heavy chains, two intermediate chains, two light intermediate chains and a few pairs of light chains (molecular weight: ~1.2 MDa) (Kardon and Vale, 2009). The motor domain of kinesin is compact with its catalytic and microtubule-binding sites close to each other; dynein has two sites separated far apart (Fig. 1.3A) and relies on long-range allosteric communication to produce movement (Roberts et al., 2013). Though sharing an overlapping microtubule-binding site (Mizuno et al., 2004), kinesins and dyneins differ structurally and belong to different protein superfamilies. Kinesin, like myosin, is related to the G protein superfamily (Kull et al., 1998). In contrast, dynein is a member of the AAA+ superfamily (an abbreviation for ATPases Associated with diverse cellular Activities) (Neuwald et al., 1999). Dynein is an unusual member in this family. Most AAA+ proteins are assembled with five or six identical subunits, while dynein has six AAA+ subdomains joined together in one polypeptide and only some subdomains can bind or hydrolyze ATP.

Kinesin and dynein have different stepping patterns along the microtubule. Two motor domains, "heads", of kinesin alternatively take 16 nm forward steps in

a “hand-over-hand” manner (Fig. 1.3B) (Asbury et al., 2003; Kaseda et al., 2003; Yildiz et al., 2004), where intramolecular strain coordinates two heads and prevents them from simultaneous detachment (Hancock and Howard, 1999; Spudich, 2006; Yildiz et al., 2008). In contrast, dynein often takes irregular steps: larger (32 nm or more), off-axis, and even backwards steps (Reck-Peterson et al., 2006). Two-color single-molecule microscopy with high-precision tracking further revealed dynein’s distinct stepping pattern: two heads take stochastic steps when they are close together, but more coordinated steps occur when the inter-head separation increases (Fig. 1.3C) (DeWitt et al., 2012; Qiu et al., 2012).

Because dynein is large, complex, and difficult to express and purify, dissecting its structure and function has been a challenge in the motor field, even though it was discovered a long time ago (Gibbons, 1963; Gibbons and Rowe, 1965). In the past decade, the development of two recombinant expression systems for dynein, *Dictyostelium* (Nishiura et al., 2004) and *S. cerevisiae* (Reck-Peterson et al., 2006), has allowed robust overexpression and extensive modification of dynein—mutation, truncation, insertion and site-specific labeling. These facilitated a succession of structural and *in-vitro* reconstitution studies, which greatly enriches and expands our understanding of dynein’s structure and unique intramolecular communication mechanism.

Cytoplasmic dynein structure and mechanism

The structural organization of dynein

Dynein is the largest and most complex cytoskeletal motor. Holo-dynein consists of two motor-containing heavy chains and multiple non-catalytic subunits (Fig. 1.4). The current understanding of dynein's structure and mechanochemical cycle is derived from electron microscopy studies (Burgess et al., 2003; Roberts et al., 2009), recent atomic and near-atomic resolution structures of the motor domain (Carter et al., 2011; Kon et al., 2011, 2012; Schmidt et al., 2012) and a wealth of single-molecule and biochemical data (Reck-Peterson et al., 2006; Kon et al., 2005, 2009; reviewed in Roberts et al., 2013).

The N-terminal third of the dynein heavy chain is called the tail domain (Fig. 1.4A). The tail contains sequences important for dimerization (Habura et al., 1999; Koonce, 1996; Reck-Peterson et al., 2006) and binding of dynein's associated subunits. The tail has also been proposed to coordinate dynein's two motor domains to enhance processivity (Ori-McKenney et al., 2010). Dynein's non-catalytic subunits assemble around the tail domain (Fig. 1.4B). They are all dimeric and include the dynein intermediate, light-intermediate, and one-three classes of light chains (TCTEX, LC8 and Roadblock) (Kardon and Vale, 2009; Pfister et al., 2006). Current evidence suggests that these non-catalytic subunits facilitate heavy chain dimerization, stability of the holo-enzyme (Rao et al., 2013) and are important for linking dynein to cargo (Vaughan and Vallee, 1995; Karki and Holzbaur, 1995; Purohit et al., 1999; Tai et al., 1999; Farkasovsky and Küntzel, 2001). These subunits are not essential for yeast dynein's motility *in vitro* (Reck-Peterson et al., 2006), but can add functional diversity to dynein *in vivo* (Ha et al., 2008).

The remaining C-terminal region of the dynein heavy chain comprises the motor domain, which consists of the AAA+ ring and additional functional units: the stalk containing the microtubule-binding domain (MTBD), the linker and C sequence (Fig. 1.4). The dimer of two motor domains is required and sufficient for dynein processivity (Reck-Peterson et al., 2006).

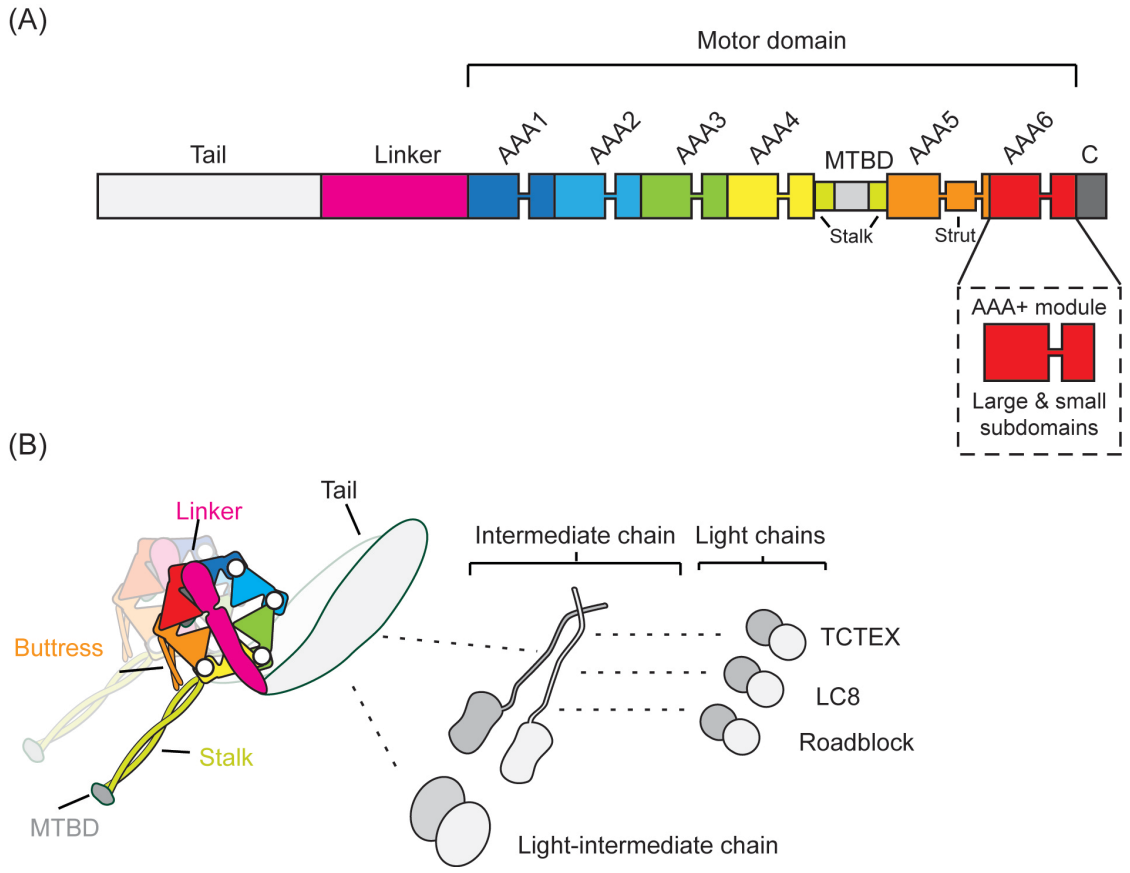

Figure 1.4 Overall composition and structure of dynein
(A) Sequence diagram of the dynein heavy chain, including its functional domains: the tail, linker, AAA+ ring (AAA1-AAA6), microtubule-binding domain (MTBD), stalk, buttress and C sequence domain. Each AAA+ module is made of a large subdomain and a small subdomain. The color code for each domain is used for all Fig.s in this chapter, unless noted. (B) Cartoon illustration of the dynein structure, including the dynein heavy chain and other non-catalytic subunits: intermediate chains, light-intermediate chains, and light chains. The white circles in the ring represent four nucleotide-binding sites. The dashed lines represent the interaction between different dynein chains. Adapted from Fig. 2 of (Roberts et al., 2013).

The AAA+ ring. Dynein's motor domain is a member of the AAA+ superfamily and contains six concatenated AAA+ modules (AAA1-AAA6). AAA1 is the main site of ATP hydrolysis; AAA1 mutants have no ATPase activity (Gibbons and Gibbons, 1987; Gibbons et al., 1987; Kon et al., 2004). Structural studies revealed that AAA2 binds, but can't hydrolyze ATP due to the missing catalytic glutamate, which suggests AAA2 may serve as a rigid structural connection between AAA1 and AAA3 (Kon et al., 2012; Schmidt et al., 2012). AAA3 and AAA4 have all residues required for ATP hydrolysis, and mutants that can't bind to or hydrolyze ATP show motility defects (Cho et al., 2008; Kon et al., 2004). AAA5 and AAA6 are highly divergent AAA domains and have no conserved Walker A/B motifs to bind ATP; rather they serve as structural components to complete the ring (Neuwald et al., 1999). Each AAA module consists of a large domain (AAAL) and a small domain (AAAs). Gaps between neighboring AAA domains open to release nucleotide, and close—bringing the arginine finger from the neighboring domain to contact the nucleotide—to hydrolyze ATP

The stalk and microtubule-binding domain. An insert from AAA4's small domain is called the stalk, composed of two α-helices that form an anti-parallel coiled coil (Carter et al., 2011; Kon et al., 2011). At the tip of the stalk is the microtubule-binding domain (MTBD), where dynein binds and releases from its track—the microtubule (Gee et al., 1997). AAA5's small domain contains another insert called the buttress (or strut) (Carter et al., 2011; Kon et al., 2011). One hypothesis suggests that the two helices of the coiled coil in the stalk can

slide relatively to each other as a communication pathway between the AAA+ ring and the MTBD (Carter et al., 2008; Gibbons et al., 2005; Kon et al., 2009). The buttress may interact with the stalk to affect this communication (Kon et al., 2011, 2012).

The linker. The N-terminal rod-like region of the dynein motor domain—a linkage between the tail and AAA1—is the linker domain (Burgess et al., 2003), which arches over the AAA+ ring (Carter et al., 2011; Kon et al., 2011). The linker moves in response to dynein's nucleotide hydrolysis cycle and is thought to generate force to pull cargo and another head of dynein forwards (Burgess et al., 2003; Kon et al., 2005).

The C sequence domain. The C-terminal region of the motor domain is referred to as the C sequence and forms a domain on the opposite side of the ring from the linker. Its length varies among species and it may modulate dynein processivity (Kon et al., 2012; Numata et al., 2011) and stabilize the interaction between the linker and the AAA+ ring on the other side (Roberts et al., 2012).

The mechanochemical cycle

Structural changes in dynein that drive motility and pull cargo are coupled to ATP binding and hydrolysis through long-distance intramolecular communication. In this section, I will introduce a current model of dynein's mechanochemical cycle (Fig. 1.5). The word, "dynein," in this section refers to one protomer of dynein, which means one dynein motor domain.

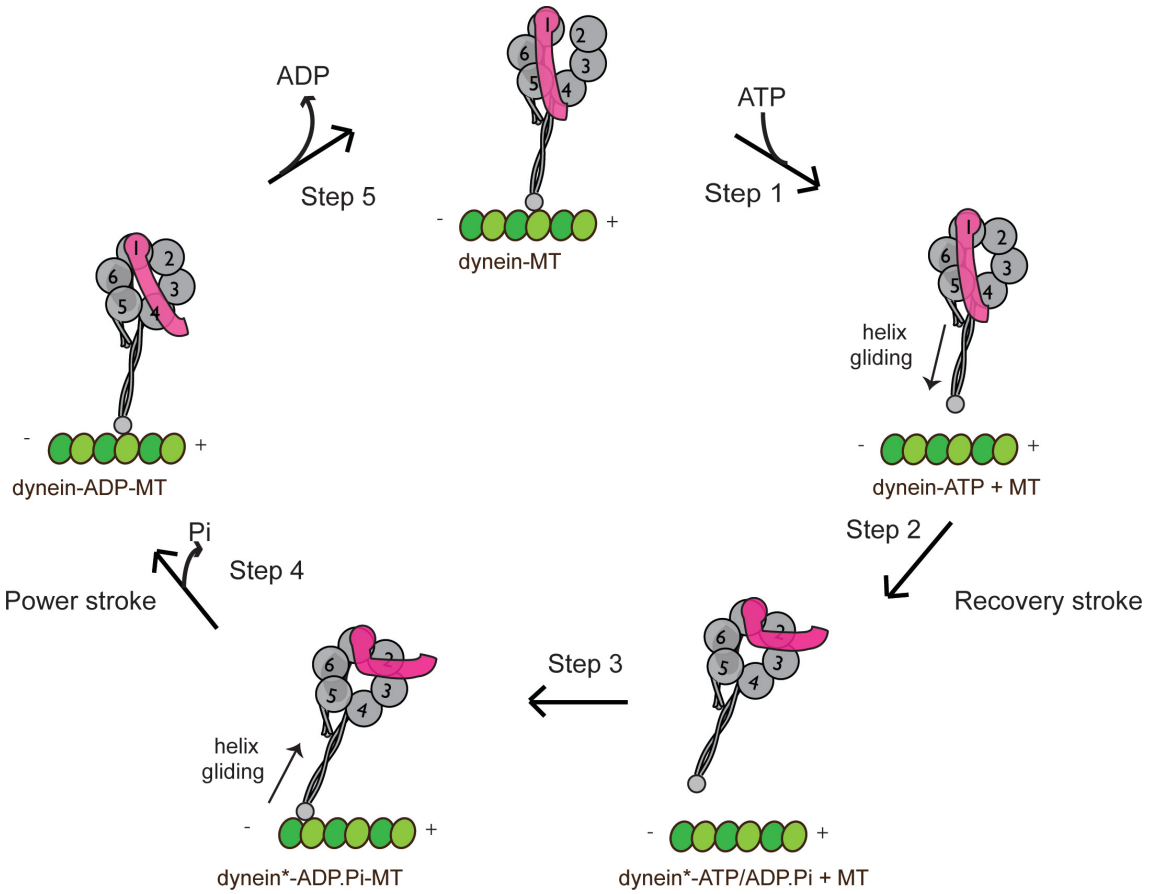

Figure 1.5 Model of dynein's mechanochemical cycle
A cartoon scheme of the ATPase cycle and the linker swing cycle, as well as the dynein affinity change with the microtubule. Here, dynein and dynein* represent molecules with the linker in the post-stroke and pre-stroke positions. MT represents the microtubule. The low affinity and strong affinities of dynein with the microtubule are shown by “dynein + MT” and “dynein-MT”, respectively. The gap between AAA1 and AAA2 in Step 1 indicates the open nucleotide-binding pocket before ATP binding.

In the nucleotide-free state (also called the apo state), dynein is tightly bound to the microtubule and its MTBD is in the high-affinity state. Steps 1 and 2: After an ATP molecule binds to AAA1—the main hydrolysis site of dynein—two major conformational changes are propagated from the closing of the nucleotide-binding pocket at AAA1 (Carter et al., 2011; Roberts et al., 2012; Schmidt et al., 2012). Step1: On one hand, the change propagates down to the MTBD through the sliding of two helices in the stalk. Consequently, the affinity of the MTBD for

the microtubule decreases releasing dynein from the microtubule. Dynein will then diffuse and search for the next binding site. Step 2: On the other side, as a slower process (Imamula et al., 2007), the linker swings across the ring to near AAA2, which is called the “pre-powerstroke” (Burgess et al., 2003; Kon et al., 2005). Step 3: Upon rebinding, the MTBD adopts a high-affinity interaction with the microtubule. Step 4: This binding information is transmitted through the sliding of the stalk back to the AAA ring, which promotes the release of the phosphate (Pi), a product of ATP hydrolysis. Meanwhile, the linker swings from near AAA2 to near AAA4, which is called the “powerstroke” (Burgess et al., 2003; Kon et al., 2005). The movement of the linker generates force and pulls the attached protomer (and cargo) towards the minus end of the microtubule. Phosphate release is a rate-limiting step in the entire mechanochemical cycle. Step 5: In the final step of the mechanochemical cycle, ADP is released from AAA1 and the linker moves from AAA4 back to AAA5 (Roberts et al., 2012). A new cycle will begin when dynein binds another molecule of ATP.

In the following sections, I will describe two important long-range communication events that occur in dynein in more detail, as they are critical to the new modes of dynein regulation established in Chapters 2 and 3.

The helix-sliding model

Unlike kinesin, dynein’s ATP-hydrolysis domain and MTBD are separated by a ~15 nm stalk. The leading hypothesis to explain how the two domains

communicate during the mechanochemical cycle is the “helix-sliding” model (Fig. 1.6).

Initially, Gibbons—the discoverer of dynein (Gibbons and Rowe, 1965)—and his coworkers developed a simplified system—a truncated construct (MTBD + stalk) stabilized by the fusion with Seryl-tRNA synthetase (SRS) as a base (Gibbons et al., 2005). Sequence analysis of the dynein stalk suggested that the hydrophobic residues of the two coiled coils in the stalk (CC1 and CC2) can potentially pack against each other in two different registries (α-registry or β-registry) (Fig. 1.6A&B). Gibbons et al then showed that the microtubule binding affinity of dynein could be modulated by inserting or deleting several residues on CC1, which would shift its position relative to CC2 (Fig. 1.6C&D). They proposed that dynein uses the sliding of the two helices in its stalk as a mechanism of communicating between the AAA+ ring and the MTBD.

Later, Kon et al. further tested this model in a functional dynein (Kon et al., 2009). They mutated one residue on each helix of the stalk to cysteine and crosslinked two cysteines to “lock” dynein in a specific registry. They found that the β-registry construct binds microtubules weakly and has a low ATPase activity, while the α-registry construct binds microtubules strongly and has a high ATPase activity. This work provided more evidence for the helix-sliding model.

However, the structural basis of sliding in the stalk and affinity modulation of the MTBD is still unclear. Determining this requires, at a minimum, a low-affinity free dynein and a high-affinity dynein bound to the microtubule. The SRS-MTBD chimeric system provides an excellent system for these experiments.

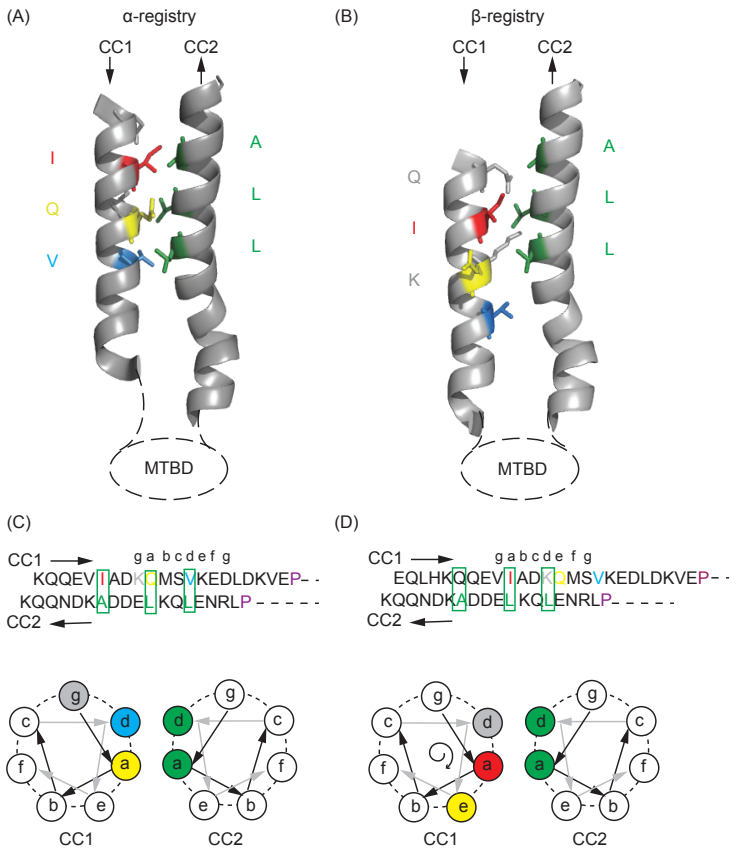

Figure 1.6 The helix-sliding model

(A) Close up view of half-heptad residues forming hydrophobic interaction between two coiled-coil helices (CC1 and CC2) in the stalk at the α registry. Ile-3269(I) (red), Gln-3273(Q) (yellow), Val-3276(V) (blue) on CC1 and Leu-3414(L), Leu-3417(L), Ala-3421(A) (green) on CC2 are shown in the stick mode with CC1 and CC2 backbones labeled in grey ribbons. **(B)** In the β registry, CC1 is rotated and shifted down by four residues: Ile-3269(I) (red) and two additional residues, Gln-3265(Q) (grey), Lys-3272(K) (grey) on the CC1 forming new interactions with the same residues (green) on CC2. **(C)** (Top) Sequence diagram showing residues on CC1 and CC2 at the α registry corresponding to (A). The position of each residue in the heptad repeat is labeled in the order of abcdefg. Hydrophobic interactions between two helices are labeled with green boxes at positions "a" and "d". The conserved prolines are labeled in purple as a boundary line between the stalk and the MTBD. (Bottom) Cross-section diagram of the helical CC1 and CC2 showing relative positions of residues in one heptad repeat, whose sequence is indicated by arrows. Residues connected by black arrows are farther from the MTBD than the ones connected by grey arrows. **(D)** Equivalent to (C) corresponding to the β registry in (B). The spiral arrow represents the rotation Gln-3273(Q) (yellow) takes from the α registry to the β registry, which is also the rotation CC1 takes.

The structure of a low-affinity MTBD was obtained by X-ray crystallography (Carter et al., 2008). In Chapter 2, I will describe our structural and functional work solving the high-affinity MTBD on the microtubule, and the new insights we made regarding how dynein's microtubule interactions are regulated.

The role of the linker domain

The linker has been proposed to amplify ATP-induced Angstrom-scale conformational changes in the AAA ring to generate force and processive movement. The molecular mechanism of this communication is beginning to emerge.

Recent structural studies revealed that the linker consists of four helical subdomains (Fig. 1.7A). The C-terminal subdomain (subdomain 4) extensively interacts with AAA1 and AAA6 and is considered to be a stable base connecting to the ring. The N-terminal subdomain (subdomain 1) is motile and can be located at multiple positions with respect to the AAA ring at different stages of the mechanochemical cycle (Roberts et al., 2012): AAA2 (Kon et al., 2005), AAA4 (Kon et al., 2012; Roberts et al., 2009) or AAA5 (Carter et al., 2011). The remaining subdomains (subdomains 2 and 3) only overlap with a single helix in the AAA+ ring, which may act as a hinge site (Fig. 1.7B) (Carter et al., 2011; Kon et al., 2012).

The linker is stiff over its length when unlocked from the ring, which suggests that the hinge is caused by interacting with the AAA ring (Roberts et al., 2012). One contact site—two conserved β-hairpins in AAA2—are proposed to

interact with the linker and induce its bending (Fig. 1.7C) (Kon et al., 2012; Schmidt et al., 2012). Another contact site is at AAA5, a highly conserved hydrophobic phenylalanine(Phe) and its surrounding electrostatic interactions (Fig. 1.7D). It is thought to be the linker-docking site that may be required to release ADP in the final step of dynein's mechanochemical cycle (Schmidt et al., 2012).

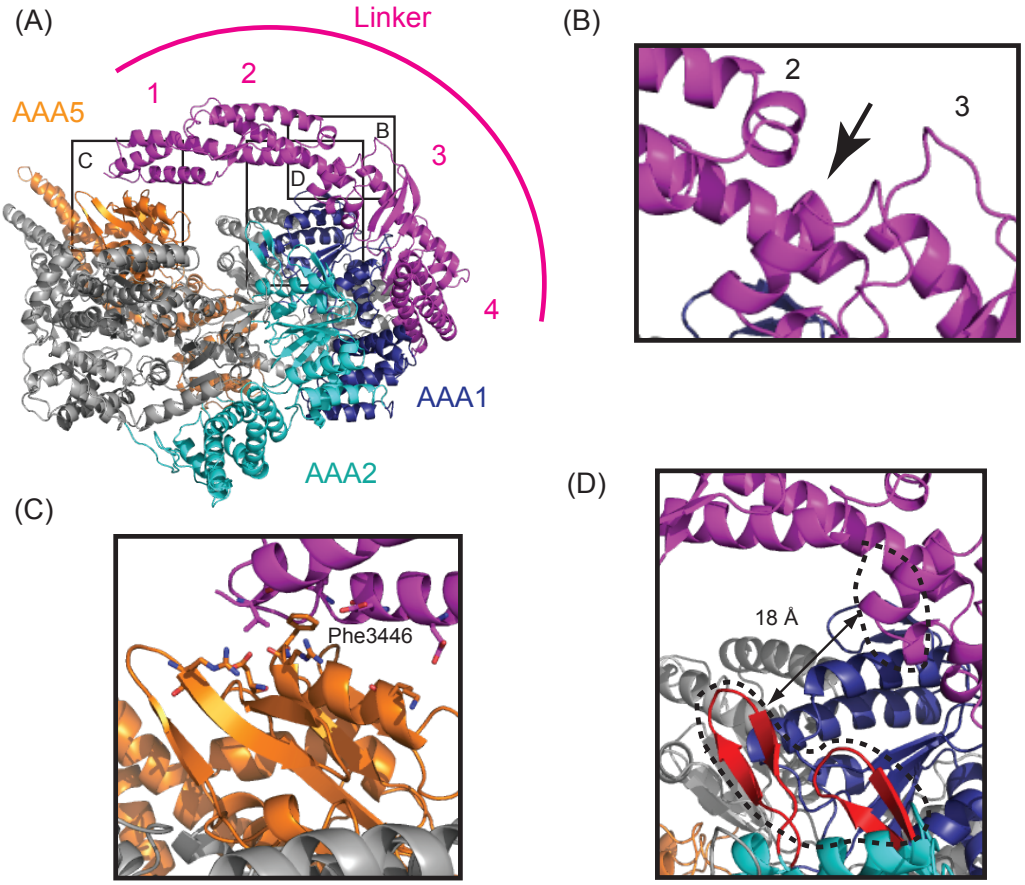

Figure 1.7 Dynein's linker and its interaction with the AAA ring
(A) Four subdomains of the linker are numbered. It arches above the AAA ring: subdomains 3 and 4 interact with AAA1 and subdomain 1 interacts with AAA5. (B) The hinge between subdomains 2 and 3 is labeled by a black arrow. (C) Two β-hairpins (red) at AAA2 are very close (~18 Å) to the linker hinge. Patches of conserved residues are shown by black dotted lines. Adapted from Fig. 2&3 of (Schmidt et al., 2012).

Studies using fluorescence resonance energy transfer (FRET) and presteady-state kinetic analysis added dynamic information to the linker swing model (Mogami et al., 2007). The recovery stroke proceeds fast (~180 s^{-1}) and is not affected by microtubules, while the powerstroke, a rate-limiting step, is very slow (~0.2 s^{-1}) in the absence of microtubules, and can be accelerated by microtubules.

Mutations disrupting the interaction between the AAA ring and the linker affect the ATPase activity and the affinity of the MTBD for the microtubule. Blocking or interfering with this interaction externally provides a possible mode for regulating dynein's activity. In Chapter 3, I will discuss our findings that show how dynein is regulated by the Lis1 protein. In this work the interaction between the ring and the linker plays an important role.

Lis1 and other regulators of cytoplasmic dynein

Dynein not only has complex allosteric communication within and between domains, but is also subject to complex external regulation. The dynactin and Lis1/Nudel complexes are two ubiquitous dynein regulators (Kardon and Vale, 2009; Vallee et al., 2012).

Dynactin is a large protein complex with a molecular weight of ~ 1 MDa, almost as large as dynein. Dynactin is highly asymmetric with a roughly L-shaped structure (Schafer et al., 1994; Hodgkinson and Peters, 2005; Imai et al., 2014). It has 11 subunits, including the largest subunit p150, a filament of actin-related protein 1 (ARP1), and other subunits (Schroer, 2004) (Fig. 1.8). It is still not clear

how those subunits are organized structurally. Dynactin has been found to be essential for nearly every cellular function of cytoplasmic dynein, including targeting dynein to microtubule plus ends, linking dynein to cargo, coordinating bidirectional transport, and increasing dynein processivity (reviewed in Schroer, 2004; Kardon and Vale, 2009). Recent work has shown that dynactin, together with a cargo-specific adaptor (e.g. BicD2, Rab11-FIP3, Spindly, Hook3), is required for mammalian dynein processivity (McKenney et al., 2014; Schlager et al., 2014).

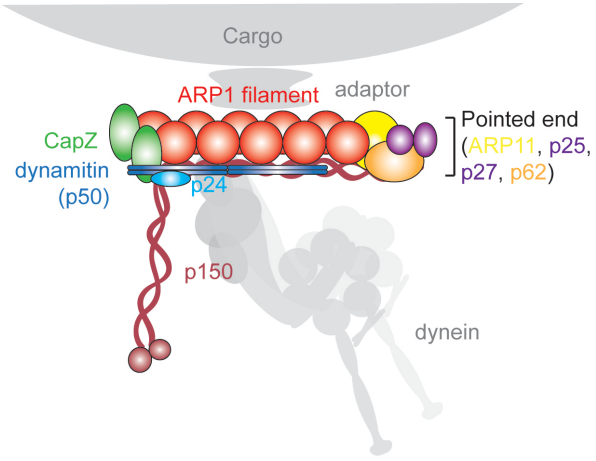

Figure 1.8 Composition and structure of the dynactin complex
Schematic illustrating the organization and approximate structural features of dynactin. Each subunit is labeled with its name in the same color. Dynein, cargo and a cargo adaptor are shown in grey, indicting their potential interactions with dynactin.

Lis1 was first identified in a rare human disease, lissencephaly, a brain developmental disorder where neurons are unable to migrate to their correct destination in the cerebral cortex and the brain lacks folds and grooves (Reiner et al., 1993). Later experiments showed that Lis1 functions in the dynein pathway (Xiang et al., 1995).

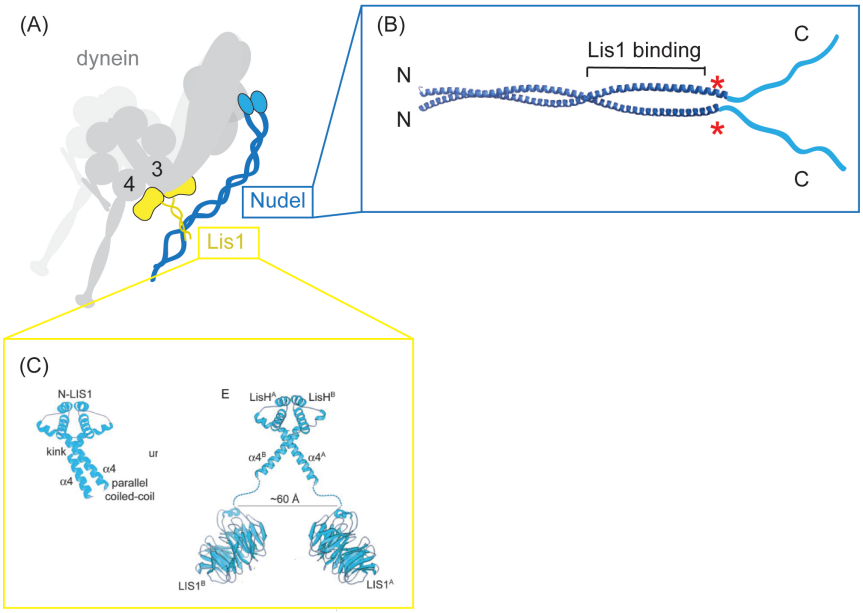

Figure 1.9 Composition and structure of Lis1-Nudel
(A) Lis1 and Nudel interact with dynein as a complex. Nudel serves as a tether linking Lis1 to dynein(Efimov, 2003; Huang et al., 2012; Li et al., 2005; McKenney et al., 2010; Wang and Zheng, 2011; Zyłkiewicz et al., 2011) Lis1 binds near AAA3 and AAA4 of dynein (Derewenda et al., 2007) Schematic representation of Nudel based on its crystal structure (PDB: 2V71). The N-terminal region (navy) contains the Lis1 binding site, while the unstructured C-terminal region (blue) binds to the dynein associated chains. The red asterisks mark the region containing phosphorylation sites. (C) Lis1 (yellow) may undergo conformational changes. Left: Lis1 crystalized alone (PDB: 1UUJ). Right: Lis1 crystalized with a cofactor protein (PDB: 1VYH). Adapted from Fig. 2 of Tarricone et al. (Tarricone et al., 2004).

This Lis1/Nudel complex is a heterotetramer (Fig. 1.9A) that is known to be involved in positioning the nucleus and microtubule organizing center, and targeting dynein to the microtubule plus end, cell cortex and kinetochore (Kardon and Vale, 2009; Vallee et al., 2012). Both *in vitro* and *in vivo* studies suggested that Nudel promotes the recruitment of Lis1 to dynein (Efimov, 2003; Huang et al., 2012; Li et al., 2005; McKenney et al., 2010; Wang and Zheng, 2011;

Zyłkiewicz et al., 2011). Nudel contains an N-terminal coiled-coil domain that interacts with Lis1 (Derewenda et al., 2007) and an unstructured C-terminus that interacts with the dynein intermediate chain and light chain LC8 (Stehman et al., 2007) (Fig. 1.9B). Several phosphorylation sites on Nudel are implicated in mediating Lis1-Nudel's interaction with dynein (Hebbar et al., 2008; Mori et al., 2009; Niethammer et al., 2000; Pandey and Smith, 2011; Shen et al., 2008; Zyłkiewicz et al., 2011).

In the absence of Nudel, Lis1 alone can bind dynein *in vitro* (Huang et al., 2012; McKenney et al., 2010). Lis1 is the only regulator known to bind the motor domain of dynein (Sasaki et al., 2000; Tai et al., 2002; Markus et al., 2009; Huang et al., 2012; McKenney et al., 2010). Thus, dynein regulation by Lis1 can be studied in the absence of dynein's tail domain or additional regulatory proteins. Like dynein, Lis1 is dimeric. Its N-terminal domain is composed of a LisH dimerization motif, followed by a linker and an alpha helix (Fig. 1.9C) (Kim et al., 2004). Lis1's C-terminal domain is a β-propeller made of seven WD repeats (Tarricone et al., 2004). The β-propeller alone can bind dynein (Huang et al., 2012). The top face of the β-propeller, which contains more conserved residues, is hypothesized to be the interface with dynein. Many disease-related mutations (deletions and missense point mutations) are also located on the top face of the Lis1 β-propeller (Tarricone et al., 2004).

How does Lis1 affect dynein motility? Recent work suggests that Lis1 slows down the movement of dynein (Yamada et al., 2008; McKenney et al., 2010; Huang et al., 2012;). How is this accomplished? Previous work

hypothesized that Lis1 might slow down dynein's ATPase activity by binding to AAA1 (Sasaki et al., 2000; Tai et al., 2002). Experiments on the molecular basis of Lis1 regulation of yeast dynein performed in our lab have led to a more in-depth understanding of Lis1's mechanism of regulation. In this work, 2D negative-stain electron microscopy (EM) revealed that Lis1 binds near dynein's AAA3/AAA4 rather than AAA1. Single-molecule functional studies showed that Lis1 prolongs dynein's attachment on the microtubule, while dynein continues to hydrolyze ATP at a similar rate. Thus, a "clutch" model was proposed, where Lis1 can alter the communication between the AAA+ ring and the MTBD. My thesis work used this previous work as a starting point to further understand the Lis1 mechanism (Chapter 3).

In metazoans, in addition to targeting dynein to the plus end, Lis1 may have additional roles. For example, Lis1 may help dynein work against high load (McKenney et al., 2010). This idea is supported by the findings in mammalian neurons that inhibition of Lis1 preferentially affects larger cargo (Pandey and Smith, 2011; Yi et al., 2011). However, this cargo-size dependence may be species- and/ or cell-type specific, since Lis1 is ubiquitously used to initialize transport of different sized cargos in the filamentous fungus *Aspergillus nidulans* (Egan et al., 2012).

These recent studies raise new questions. What is the 3D structure of the dynein-Lis1 complex? Can dynein's mechanical element, the linker, still swing when Lis1 binds to dynein? How does Lis1 disrupt the communcation between the MTBD and the ATPase ring? In Chapter 3, we use cryo-negative stain

electron microscopy to obtain high-resolution 3D structures of the dynein-Lis1 complex for the first time. We then use these structures to design FRET, single-molecule, and biochemical experiments. Our work provides new mechanistic insights for how dynein is regulated by Lis1.

References

Alushin, G.M., Lander, G.C., Kellogg, E.H., Zhang, R., Baker, D., and Nogales, E. (2014). High-resolution microtubule structures reveal the structural transitions in αβ-tubulin upon GTP hydrolysis. Cell *157*, 1117–1129.

Asbury, C., Fehr, A., and Block, S. (2003). Kinesin Moves by an Asymmetric Hand-Over-Hand Mechanism. Science *302*, 2130–2134.

Burgess, S.A., Walker, M.L., Sakakibara, H., Knight, P.J., and Oiwa, K. (2003). Dynein structure and power stroke. Nature *421*, 715–718.

Carter, A.P., Garbarino, J.E., Wilson-Kubalek, E.M., Shipley, W.E., Cho, C., Milligan, R.A., Vale, R.D., and Gibbons, I.R. (2008). Structure and functional role of dynein's microtubule-binding domain. Science *322*, 1691–1695.

Carter, A.P., Cho, C., Jin, L., and Vale, R.D. (2011). Crystal structure of the dynein motor domain. Science *331*, 1159–1165.

Conde, C., and Cáceres, A. (2009). Microtubule assembly, organization and dynamics in axons and dendrites. Nature Reviews. Neuroscience *10*, 319-332.

Cyr, J.L., Pfister, K.K., Bloom, G.S., Slaughter, C.A., and Brady, S.T. (1991). Molecular genetics of kinesin light chains: generation of isoforms by alternative splicing. Proceedings of the National Academy of Sciences of the United States of America *88*, 10114-10118.

Derewenda, U., Tarricone, C., Choi, W.C., Cooper, D.R., Lukasik, S., Perrina, F., Tripathy, A., Kim, M.H., Cafiso, D.S., Musacchio, A., et al. (2007). The structure of the coiled-coil domain of Ndel1 and the basis of its interaction with Lis1, the causal protein of Miller-Dieker lissencephaly. Structure *15*, 1467–1481.

DeWitt, M.A., Chang, A.Y., Combs, P.A., and Yildiz, A. (2012). Cytoplasmic dynein moves through uncoordinated stepping of the AAA+ ring domains. Science *335*, 221–225.

Efimov, VP (2003). Roles of NUDE and NUDF proteins of Aspergillus nidulans: insights from intracellular localization and overexpression effects. Molecular Biology of the Cell *14*, 871-888.

Egan, M.J., Tan, K., and Reck-Peterson, S.L. (2012). Lis1 is an initiation factor for dynein-driven organelle transport. The Journal of Cell Biology *197*, 971–982.

Etienne-Manneville, S. (2013). Microtubules in cell migration. Annual Review of Cell and Developmental Biology *29*, 471–499.

Gee, M.A., Heuser, J.E., and Vallee, R.B. (1997). An extended microtubule-binding structure within the dynein motor domain. Nature *390*, 636–639.

Gibbons, IR (1963). Studies on the protein components of cilia from Tetrahymena pyriformis. PNAS *50*, 1002–1010.

Gibbons, BH, and Gibbons, IR (1987). Vanadate-sensitized cleavage of dynein heavy chains by 365-nm irradiation of demembranated sperm flagella and its effect on the flagellar motility. The Journal of Biological Chemistry. *262*, 8354-8359.

Gibbons, I.R., and Rowe, A.J. (1965). Dynein: A Protein with Adenosine Triphosphatase Activity from Cilia. Science *149*, 424–426.

Gibbons, I., Lee-Eiford, A., Mocz, G., Phillipson, C., Tang, W., and Gibbons, B. (1987). Photosensitized cleavage of dynein heavy chains. Cleavage at the “V1 site” by irradiation at 365 nm in the presence of ATP and vanadate. The Journal of Biological Chemistry *262*, 2780–2786.

Gibbons, I.R., Garbarino, J.E., Tan, C.E., Reck-Peterson, S.L., Vale, R.D., and Carter, A.P. (2005). The affinity of the dynein microtubule-binding domain is modulated by the conformation of its coiled-coil stalk. The Journal of Biological Chemistry *280*, 23960–23965.

Ha, J., Lo, K.W., Myers, K.R., Carr, T.M., Humsi, M.K., Rasoul, B.A., Segal, R.A., and Pfister, K.K. (2008). A neuron-specific cytoplasmic dynein isoform preferentially transports TrkB signaling endosomes. The Journal of Cell Biology *181*, 1027–1039.

Habura, A., Tikhonenko, I., Chisholm, R.L., and Koonce, M.P. (1999). Interaction mapping of a dynein heavy chain. Identification of dimerization and intermediate-chain binding domains. The Journal of Biological Chemistry *274*, 15447–15453.

Hancock, WO, and Howard, J (1999). Kinesin’s processivity results from mechanical and chemical coordination between the ATP hydrolysis cycles of the

two motor domains. PNAS *96*, 13147–13152.

Hebbar, S., Mesngon, M.T., Guillotte, A.M., Desai, B., Ayala, R., and Smith, D.S. (2008). Lis1 and Ndel1 influence the timing of nuclear envelope breakdown in neural stem cells. The Journal of Cell Biology *182*, 1063–1071.

Hirokawa, N. (1998). Kinesin and dynein superfamily proteins and the mechanism of organelle transport. Science *279*, 519-26.

Hirokawa, N., Noda, Y., Tanaka, Y., and Niwa, S. (2009). Kinesin superfamily motor proteins and intracellular transport. Nat Rev Mol Cell Biol*10*, 682-96.

Hodgkinson, JL, and Peters, C (2005). Three-dimensional reconstruction of the dynactin complex by single-particle image analysis. PNAS *102*, 3667–3672.

Huang, J., Roberts, A.J., Leschziner, A.E., and Reck-Peterson, S.L. (2012). Lis1 acts as a “clutch” between the ATPase and microtubule-binding domains of the dynein motor. Cell *150*, 975–986.

Imai, H., Narita, A., Maéda, Y., and Schroer, T. (2014). Dynactin 3D Structure: Implications for Assembly and Dynein Binding. Journal of Molecular Biology *426*, 3262-3271.

Imamula, K., Kon, T., Ohkura, R., and Sutoh, K. (2007). The coordination of cyclic microtubule association/dissociation and tail swing of cytoplasmic dynein. Proceedings of the National Academy of Sciences of the United States of America *104*, 16134–16139.

Kardon, J.R., and Vale, R.D. (2009). Regulators of the cytoplasmic dynein motor. Nature Reviews. Molecular Cell Biology *10*, 854–865.

Kaseda, K, Higuchi, H, and Hirose, K (2003). Alternate fast and slow stepping of a heterodimeric kinesin molecule. Nat Cell Biol *5*,1079-1082.

Kikkawa, M. (2013). Big steps toward understanding dynein. The Journal of Cell Biology *202,* 15-23.

Kim, MH, Cooper, DR, Oleksy, A, and Devedjiev, Y (2004). The Structure of the N-Terminal Domain of the Product of the Lissencephaly Gene Lis1 and Its Functional Implications. Structure *12*, 987-98.

Kon, T., Nishiura, M., Ohkura, R., Toyoshima, Y.Y., and Sutoh, K. (2004). Distinct functions of nucleotide-binding/hydrolysis sites in the four AAA modules of cytoplasmic dynein. Biochemistry *43*, 11266–11274.

Kon, T., Mogami, T., Ohkura, R., Nishiura, M., and Sutoh, K. (2005). ATP

hydrolysis cycle-dependent tail motions in cytoplasmic dynein. Nature Structural & Molecular Biology *12*, 513–519.

Kon, T., Imamula, K., Roberts, A.J., Ohkura, R., Knight, P.J., Gibbons, I.R., Burgess, S.A., and Sutoh, K. (2009). Helix sliding in the stalk coiled coil of dynein couples ATPase and microtubule binding. Nature Structural & Molecular Biology *16*, 325–333.

Kon, T., Sutoh, K., and Kurisu, G. (2011). X-ray structure of a functional full-length dynein motor domain. Nature Structural & Molecular Biology *18*, 638–642.

Kon, T., Oyama, T., Shimo-Kon, R., Imamula, K., Shima, T., Sutoh, K., and Kurisu, G. (2012). The 2.8 Å crystal structure of the dynein motor domain. Nature *484*, 345–350.

Koonce, MP, and Samso, M (1996). Overexpression of cytoplasmic dynein's globular head causes a collapse of the interphase microtubule network in Dictyostelium. Mol Biol Cell. *7*, 935-48.

Kull, J.F., Vale, R.D., and Fletterick, R.J. (1998). The case for a common ancestor: kinesin and myosin motor proteins and G proteins. Journal of Muscle Research & Cell Motility *19*, 877–886.

Li, J., Lee, W.-L.L., and Cooper, J.A. (2005). NudEL targets dynein to microtubule ends through LIS1. Nature Cell Biology *7*, 686–690.

McKenney, R., Vershinin, M., Kunwar, A., Vallee, R., and Gross, S. (2010). LIS1 and NudE induce a persistent dynein force-producing state. Cell *141*, 304–314.

McKenney, R., Huynh, W., Tanenbaum, M., Bhabha, G., and Vale, R. (2014). Activation of cytoplasmic dynein motility by dynactin-cargo adapter complexes. Science (New York, N.Y.) *345*, 337–341.

Miki, H., Setou, M., Kaneshiro, K., and Hirokawa, N. (2001). All kinesin superfamily protein, KIF, genes in mouse and human. Proceedings of the National Academy of Sciences of the United States of America *98*, 7004–7011.

Mitchison, T., and Kirschner, M. (1984). Dynamic instability of microtubule growth. Nature *312*, 237 - 242.

Mitchison, T., Evans, L., Schulze, E., and Kirschner, M. (1986). Sites of microtubule assembly and disassembly in the mitotic spindle. Cell *45*, 515-27.

Mizuno, N., Toba, S., Edamatsu, M., Watai-Nishii, J., Hirokawa, N., Toyoshima, Y.Y., and Kikkawa, M. (2004). Dynein and kinesin share an overlapping microtubule-binding site. The EMBO Journal *23*, 2459–2467.

Mogami, T., Kon, T., Ito, K., and Sutoh, K. (2007). Kinetic characterization of tail swing steps in the ATPase cycle of Dictyostelium cytoplasmic dynein. The Journal of Biological Chemistry *282*, 21639–21644.

Mori, D., Yamada, M., Mimori-Kiyosue, Y., Shirai, Y., Suzuki, A., Ohno, S., Saya, H., Wynshaw-Boris, A., and Hirotsune, S. (2009). An essential role of the aPKC-Aurora A-NDEL1 pathway in neurite elongation by modulation of microtubule dynamics. Nature Cell Biology *11*, 1057–1068.

Neuwald, A.F., Aravind, L., Spouge, J.L., and Koonin, E.V. (1999). AAA+: A class of chaperone-like ATPases associated with the assembly, operation, and disassembly of protein complexes. Genome Research *9*, 27–43.

Niethammer, M., Smith, D.S., Ayala, R., Peng, J., Ko, J., Lee, M.S., Morabito, M., and Tsai, L.H. (2000). NUDEL is a novel Cdk5 substrate that associates with LIS1 and cytoplasmic dynein. Neuron *28*, 697–711.

Nishiura, M., Kon, T., Shiroguchi, K., Ohkura, R., Shima, T., Toyoshima, Y.Y., and Sutoh, K. (2004). A single-headed recombinant fragment of Dictyostelium cytoplasmic dynein can drive the robust sliding of microtubules. The Journal of Biological Chemistry *279*, 22799–22802.

Nogales, E. (2000). Structural insights into microtubule function. Annual Review of Biochemistry *69*, 277–302.

Numata, N., Shima, T., Ohkura, R., Kon, T., and Sutoh, K. (2011). C-sequence of the Dictyostelium cytoplasmic dynein participates in processivity modulation. FEBS Letters *585*, 1185–1190.

Ori-McKenney, K.M., Xu, J., Gross, S.P., and Vallee, R.B. (2010). A cytoplasmic dynein tail mutation impairs motor processivity. Nature Cell Biology *12*, 1228–1234.

Pandey, J.P., and Smith, D.S. (2011). A Cdk5-dependent switch regulates Lis1/Ndel1/dynein-driven organelle transport in adult axons. The Journal of Neuroscience : The Official Journal of the Society for Neuroscience *31*, 17207–17219.

Pfister, K.K., Shah, P.R., Hummerich, H., Russ, A., Cotton, J., Annuar, A.A., King, S.M., and Fisher, E.M. (2006). Genetic analysis of the cytoplasmic dynein subunit families. PLoS Genetics *2*, e1.

Qiu, W., Derr, N.D., Goodman, B.S., Villa, E., Wu, D., Shih, W., and Reck-Peterson, S.L. (2012). Dynein achieves processive motion using both stochastic and coordinated stepping. Nature Structural & Molecular Biology *19*, 193–200.

Rao, L., Romes, E.M., Nicholas, M.P., Brenner, S., Tripathy, A., Gennerich, A., and Slep, K.C. (2013). The yeast dynein Dyn2-Pac11 complex is a dynein dimerization/processivity factor: structural and single-molecule characterization. Molecular Biology of the Cell *24*, 2362–2377.

Reck-Peterson, S.L., Yildiz, A., Carter, A.P., Gennerich, A., Zhang, N., and Vale, R.D. (2006). Single-molecule analysis of dynein processivity and stepping behavior. Cell *126*, 335–348.

Reiner, O., Carrozzo, R., Shen, Y., Wehnert, M., Faustinella, F., Dobyns, W.B., Caskey, C.T., and Ledbetter, D.H. (1993). Isolation of a Miller-Dieker lissencephaly gene containing G protein beta-subunit-like repeats. Nature *364*, 717–721.

Roberts, A.J., Numata, N., Walker, M.L., Kato, Y.S., Malkova, B., Kon, T., Ohkura, R., Arisaka, F., Knight, P.J., Sutoh, K., et al. (2009). AAA+ Ring and linker swing mechanism in the dynein motor. Cell *136*, 485–495.

Roberts, A.J., Malkova, B., Walker, M.L., Sakakibara, H., Numata, N., Kon, T., Ohkura, R., Edwards, T.A., Knight, P.J., Sutoh, K., et al. (2012). ATP-driven remodeling of the linker domain in the dynein motor. Structure (London, England : 1993) *20*, 1670–1680.

Roberts, A.J., Kon, T., Knight, P.J., and Sutoh, K. (2013). Functions and mechanics of dynein motor proteins. Nature Reviews Molecular Cell Biology *14*, 713–726.

Schafer, D.A., Gill, S.R., Cooper, J.A., Heuser, J.E., and Schroer, T.A. (1994). Ultrastructural analysis of the dynactin complex: an actin-related protein is a component of a filament that resembles F-actin. The Journal of Cell Biology *126*, 403–412.

Schlager, M.A., Hoang, H., Urnavicius, L., Bullock, S.L., and Carter, A.P. (2014). In vitro reconstitution of a highly processive recombinant human dynein complex. The EMBO Journal *33*, 1855-68.

Schmidt, H., Gleave, E.S., and Carter, A.P. (2012). Insights into dynein motor domain function from a 3.3-Å crystal structure. Nature Structural & Molecular Biology *19*, 492–7.

Schroer, T.A. (2004). Dynactin. Annual Review of Cell and Developmental Biology *20*, 759–779.

Sharp, DJ, Rogers, GC, and Scholey, JM (2000). Microtubule motors in mitosis. Nature *407*, 41-7.

Shen, Y., Li, N., Wu, S., Zhou, Y., Shan, Y., Zhang, Q., Ding, C., Yuan, Q., Zhao, F., Zeng, R., et al. (2008). Nudel binds Cdc42GAP to modulate Cdc42 activity at the leading edge of migrating cells. Developmental Cell *14*, 342–353.

Sirajuddin, M., Rice, L.M., and Vale, R.D. (2014). Regulation of microtubule motors by tubulin isotypes and post-translational modifications. Nature Cell Biology *16*, 335–344.

Spudich, J.A. (2006). Molecular motors take tension in stride. Cell *126*, 242–244.
Stehman, S.A., Chen, Y., McKenney, R.J., and Vallee, R.B. (2007). NudE and NudEL are required for mitotic progression and are involved in dynein recruitment to kinetochores. The Journal of Cell Biology *178*, 583–594.

Vale, R.D. (2003). The molecular motor toolbox for intracellular transport. Cell *112*, 467–480.

Vallee, R.B., McKenney, R.J., and Ori-McKenney, K.M. (2012). Multiple modes of cytoplasmic dynein regulation. Nature Cell Biology *14*, 224–230.

Wang, S., and Zheng, Y. (2011). Identification of a novel dynein binding domain in nudel essential for spindle pole organization in Xenopus egg extract. The Journal of Biological Chemistry *286*, 587–593.

Westermann, S., and Weber, K. (2003). Post-translational modifications regulate microtubule function. Nature Reviews Molecular Cell Biology *4*, 938-948.

Xiang, X., Osmani, A.H., Osmani, S.A., Xin, M., and Morris, N.R. (1995). NudF, a nuclear migration gene in Aspergillus nidulans, is similar to the human LIS-1 gene required for neuronal migration. Molecular Biology of the Cell *6*, 297–310.

Xiao, H., Verdier-Pinard, P., Fernandez-Fuentes, N., Burd, B., Angeletti, R., Fiser, A., Horwitz, S.B., and Orr, G.A. (2006). Insights into the mechanism of microtubule stabilization by Taxol. Proceedings of the National Academy of Sciences of the United States of America *103*, 10166–10173.

Yagi, T. (2009). Bioinformatic approaches to dynein heavy chain classification. Methods in Cell Biology *92*, 1–9.

Yamada, M, Toba, S, Yoshida, Y, and Haratani, K (2008). LIS1 and NDEL1 coordinate the plus-end-directed transport of cytoplasmic dynein. The EMBO Journal *27*, 2471-83.

Yi, J.Y., Ori-McKenney, K.M., McKenney, R.J., Vershinin, M., Gross, S.P., and Vallee, R.B. (2011). High-resolution imaging reveals indirect coordination of opposite motors and a role for LIS1 in high-load axonal transport. The Journal of

Cell Biology *195*, 193–201.

Yildiz, A., Tomishige, M., Vale, R.D., and Selvin, P.R. (2004). Kinesin walks hand-over-hand. Science (New York, N.Y.) *303*, 676–678.

Yildiz, A., Tomishige, M., Gennerich, A., and Vale, R.D. (2008). Intramolecular strain coordinates kinesin stepping behavior along microtubules. Cell *134*, 1030–1041.

Zyłkiewicz, E., Kijańska, M., Choi, W.-C.C., Derewenda, U., Derewenda, Z.S., and Stukenberg, P.T. (2011). The N-terminal coiled-coil of Ndel1 is a regulated scaffold that recruits LIS1 to dynein. The Journal of Cell Biology *192*, 433–445.

Chapter 2 : Structural basis for microtubule binding and release by dynein

William Bret Redwine*, Rogelio Hernandez-Lopez*, Sirui Zou, Julie Huang,

Samara Reck-Peterson, Andres Leschziner

Contributions

Bret Redwine and Rogelio Hernandez-Lopez contributed equally. Bret Redwine initiated the project and performed biochemistry, sample preparation, and electron microscopy data collection. Rogelio Hernandez-Lopez and William Redwine performed 3D reconstruction. Rogelio Hernandez-Lopez performed molecular dynamics simulations. Sirui Zou performed single molecule motility experiments for dynamic salt bridge dynein mutants. Julie Huang tested wild-type dynein's salt-dependent motility properties. Andres Leschziner and Samara Reck-Peterson provided mentorship. This work was published in: Structural basis for microtubule binding and release by dynein. *Science* **337**, 1532-1536 (2012).

Abstract

Cytoplasmic dynein is a microtubule-based motor required for intracellular transport and cell division. Its movement involves coupling cycles of track binding and release with cycles of force-generating nucleotide hydrolysis. How this is accomplished given the ~25 nm separating dynein's track- and nucleotide-binding sites is not understood. Here, we present a sub-nanometer-resolution structure of dynein's microtubule-binding domain bound to microtubules by cryo-electron microscopy that was used to generate a pseudo-atomic model of the complex with molecular dynamics. We identified large rearrangements triggered by track binding and specific interactions, confirmed by mutagenesis and single molecule motility assays, which tune dynein's affinity for microtubules. Our results provide a molecular model for how dynein's binding to microtubules is communicated to the rest of the motor.

Introduction

Dyneins are ATP-driven molecular motors that move towards the minus ends of microtubules (MTs) (Gibbons, 1995). The superfamily includes axonemal dyneins, which power the movements of cilia, and those that transport cargo, which include cytoplasmic dyneins 1 ("cytoplasmic") and 2 ("intraflagellar") (Höök and Vallee, 2006). The transport of organelles, ribonucleoprotein complexes and proteins by cytoplasmic dynein is required for cellular homeostasis, cell-cell communication, cell division, and cell migration (Vale, 2003) and defects in these processes result in neurological disease in humans (Vallee et al., 2009). Despite cytoplasmic dynein's role in such diverse activities and recent advances in characterizing its structure and motility, many aspects of its molecular mechanism remain poorly understood.

The core of the cytoplasmic dynein holoenzyme is a homodimer of ~500 kDa motor-containing subunits (Fig. 2.1A). The major functional elements include: (a) a "tail" domain required for dimerization and cargo binding (Vallee et al., 2004); (b) the force-generating "head" or "motor domain" (Burgess et al., 2003; Roberts et al., 2009), a ring containing six AAA+ ATPase domains (Gibbons et al., 1991; Kon et al., 2004; Reck-Peterson and Vale, 2004); (c) a "linker" connecting the head and tail, required for motility (Burgess et al., 2003; Reck-Peterson et al., 2006; Roberts et al., 2009; Shima et al., 2006); (d) the "stalk", a long antiparallel coiled-coil that emerges from AAA4 (Carter et al., 2011; Kon et al., 2011), and (e) the MT-binding domain (MTBD), a small alpha-helical domain at the end of the stalk responsible for binding the MT track (Carter et al., 2008; Gee et al., 1997; Koonce, 1997). Unlike the other cytoskeletal molecular

motors, kinesin and myosin, dynein does not have its ATPase and polymer track binding sites located within a single domain. With 25 nm separating AAA1, the main site of ATP hydrolysis, and the MTBD, an unresolved question is how dynein coordinates the cycles of nucleotide hydrolysis and MT binding and release required for its motion.

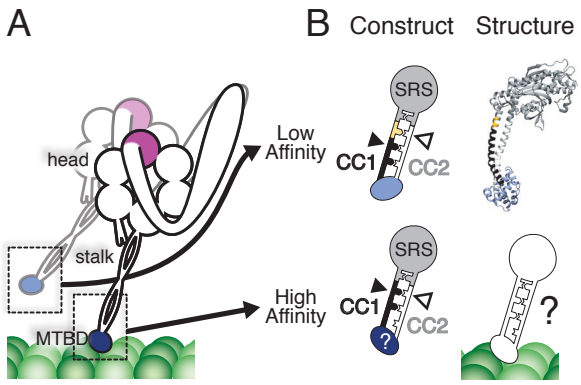

Figure 2.1 Towards a structural understanding of the helix sliding hypothesis
(A) Schematic of dimeric cytoplasmic dynein. Major features relevant to this study are indicated. The MTBD is depicted in its low- (light blue) and high- (dark blue) affinity states during a step along the MT. (B) Schematic of the fusion constructs between the MTBD and seryl-tRNA synthetase (SRS) that fix the heptad registry of the stalk. The low-affinity construct has an additional 4 amino acids (yellow) inserted in CC1 (black) relative to the high-affinity construct.

The mechanism coupling nucleotide hydrolysis to MT affinity has been suggested to be sliding in which the two helices in the stalk's coiled-coil adopt different registries by using alternative sets of hydrophobic heptad repeats (Carter et al., 2008; Gibbons et al., 2005; Kon et al., 2009). Dynein's stalk can be fixed in a specific registry by fusing it to a coiled-coil of known structure, such as that of seryl-tRNA synthetase (SRS) (Gibbons et al., 2005). Changing the length of the first stalk helix (CC1) relative to the second (CC2) shifts their alignment

between high-affinity ("α") and low-affinity ("β+") registries, and alters the affinity of the MTBD for MTs by up to twenty-fold (Fig. 2.1B) (Gibbons et al., 2005). Engineered disulfide cross-linking in the monomeric dynein motor domain showed that its stalk explores multiple registries in solution, and that a given registry is coupled to a specific MT affinity (Kon et al., 2009). Fixing the stalk registry also uncoupled the nucleotide state of the head from MT affinity (Kon et al., 2009).

Understanding the molecular mechanism by which stalk sliding is coupled to nucleotide hydrolysis and MT affinity would be aided by a structure of dynein's MTBD bound to MTs. Crystal structures are available for a low-affinity dynein MTBD fused to SRS through a short segment of the stalk (Fig. 2.1B) (Carter et al., 2008), and an ADP-bound, presumably high-affinity dynein monomer (Kon et al., 2012a). Only low-resolution structures of the MT-bound form have been reported (Carter et al., 2008; Mizuno et al., 2004). Here we describe a cryo-electron microscopy (cryo-EM) reconstruction of the MTBD bound to MTs at sub-nanometer resolution, using a high-affinity version of the SRS-MTBD construct (Gibbons et al., 2005).

Methods and Materials

SRS-MTBD purification

SRS-MTBD chimeric constructs were expressed in the *Escherichia coli* strain BL21 (DE3) containing the plasmid pLysS. Cells were grown in 8 L of LB broth at 37°C to an optical density at 600 nm of 0.5. The cells were chilled on ice with

periodic mixing until the temperature was 16°C. Protein expression was induced with 0.5 mM β-D-thiogalactopyranoside and the cells were further incubated at 16°C for 6 h. All subsequent steps were performed at 4°C or on ice. Cells were harvested by centrifugation and were resuspended in 70 mL lysis buffer (50 mM Tris-HCl, pH 8.0; 150 mM KOAc, 1 mM EDTA, 10% glycerol, 20 mM imidazole, 5 mM β-mercaptoethanol, 1 mM PMSF, and 1 μg/mL each pepstatin A, aprotinin, benzamidine, and leupeptin). The cells were lysed by sonication (6 continuous pulses at 80% power, with 2 minutes between pulses) and the resulting lysate was centrifuged at 120,000 x g in a Ti45 rotor (Beckman) for 30 min at 4°C. The cleared lysate was applied to a 10 mL Ni-NTA agaraose column (Qiagen) by gravity. The column was then washed with 300 mL lysis buffer. Bound protein was then eluted with a linear imidazole gradient from 50 mM to 500 mM. Peak fractions containing the SRS-MTBD fusion, as determined by SDS-PAGE analysis, were pooled, dialyzed for 4 h against lysis buffer, and concentrated to ~15 mg/mL with Ultracell concentration columns with a molecular weight cut-off of 30 kDa (Millipore). A fraction of this protein was then further purified on a Superdex 200 16/60 gel filtration column equilibrated in lysis buffer. A monodisperse peak was isolated and concentrated to ~4 mg/mL as described above.

Tubulin polymerization

Highly purified, glycerol-free tubulin (Cytoskeleton, Inc.) was resuspended in BRB80 (80 mM PIPES-KOH, pH 6.8; 1 mM $MgCl_2$, 1 mM EGTA, 1 mM DTT) to a

concentration of 10 mg/mL. The resuspended tubulin was centrifuged at 100,000 x g in a TLA 100 rotor (Beckman) for 30 min at 4 °C to remove aggregates, and the protein concentration was determined using an extinction coefficient of 1.15 $(mg/mL)^{-1}$. Tubulin was then polymerized with a stepwise addition of taxol as follows: 20 µL of tubulin stock was thawed quickly and placed on ice. To this 10 µL of BRB80 supplemented with 3 mM GTP was added and the mixture was transferred to a 37°C water bath. After 15, 30, and 45 minutes, additions of 0.5, 0.5, and 1.0 µL of 2 mM taxol were added by gentle swirling. The mixture was then incubated for an additional 1 h at 37°C.

Grid preparation and imaging

Purified SRS-MTBD protein was dialyzed for 4 h against lysis buffer without glycerol and added salts (cryo buffer: 50 mM Tris-HCl, pH 8.0, 1 mM $MgCl_2$, 1 mM EGTA, 1 mM DTT) in a spin dialyzer (Harvard Apparatus) fitted with a 10 kDa MWCO membrane. The protein was recovered and centrifuged at 20,000 x g in a TLA 100 rotor (Beckman) for 30 min at 4 °C to remove aggregates. C-flat 2/2-2C holey carbon grids (Protochips) were glow-discharged for 20 s at 30 mA in an Edwards carbon evaporator. MTs were diluted to 0.5 mg/mL in cryo buffer supplemented with 100 µM taxol, and 4 µL were added to a grid and allowed to absorb for 30 sec. The solution was manually blotted from the side with a torn Whatman #1 filter paper. Next, 4 µL of dialyzed SRS-MTBD was added and allowed to bind to the MTs for 1 min. The solution was blotted manually again, and the process of addition and blotting of SRS-MTBD was repeated for a total of

three times. The final blotting was done inside the humidity chamber of a Vitrobot Mark IV (FEI) set at 22°C and 100% humidity. The grids were then rapidly plunged into a liquid nitrogen-cooled ethane slush. Grids were stored in liquid nitrogen until imaging.

Grids were transferred to a Gatan 626 cryo-holder, and micrographs were collected on film (SO-163, Kodak) in a Tecnai F20 electron microscope (FEI) operating at 120 keV, and nominal magnification of 62,000. Final accumulated electron doses ranged between 15 and 20 electrons/Å^2. The actual magnification of 63,377 was calculated using tobacco mosaic virus layer lines as a standard. Film was developed using full strength D9 developer (Kodak) for 12 min. Each film was analyzed visually on a light box for drift; those without noticeable drift were digitized on an Aztek Plateau flatbed scanner (Aztek, Inc.) with a 6.35 micron step size, resulting in a final pixel size of 0.994 Å. Images were then selected for processing on the basis of high decoration, straight MTs, and the absence of crystalline ice and drift.

Image processing and three-dimensional reconstruction

Square segments of 720 pixels were extracted from micrographs containing straight MTs using BOXER (Ludtke et al., 1999) and the “helix” option with 240 pixel overlap. Pixel intensities were normalized and segments were decimated six-fold to a pixel size of 5.964 Å. Reference-free two-dimensional classification was performed as described (Alushin et al., 2010; Ramey et al., 2009). This method has been shown to sort MT segments on the basis of degree of

decoration and protofilament number (PF). After analyzing the power spectrum and one-dimensional projection of class averages, good quality boxes were assigned a PF number of 13, 14 or 15. We assigned PF number based on the consensus of PF number assignment for all boxes extracted from each individual MT. Out of 577 MTs, 189 13-PF and 375 14-PF MTs were selected for further processing.

The primary PF number population in our in vitro assembled MT preparations was 14. To maximize the data used for reconstruction, custom SPIDER scripts (Sindelar and Downing, 2007; 2010), previously used in subnanometer reconstructions of 13 PF MT complexes (Grigorieff, 2007; Sindelar and Downing, 2007), were adapted to 14 PF MTs. Initially, 13 PF and 14 PF MTs were independently processed to validate our implementation. We obtained essentially the same structure at a resolution of 20 Å, at which point the 13 PF reconstruction stopped improving (data not shown).

In our implementation, a PDB model of the SRS-MTBD-MT (PDB 3ERR (Carter et al., 2008) and 1JFF (Löwe et al., 2001)) complex was used to generate an initial low resolution volume from which a set of initial projection references was generated to assign the orientation of individual 80 Å experimental segments. The astigmatism and defocus values used to correct the contrast transfer function of the microscope were obtained from micrographs using CTFFIND3 (Mindell and Grigorieff, 2003) and were used during the reconstruction step. Three cycles of alignment using the SPIDER custom scripts with 3 rounds of reconstruction with FREALIGN (Grigorieff, 2007) in each cycle,

yielded a final 12.0 Å resolution structure (FSC at 0.143, a criterion shown to be reliable (Grigorieff and Harrison, 2011; Zhang et al., 2008) for structures refined with FREALIGN, Fig. A2.1C). Reconstructions in cycles 1 and 2 were done with data decimated three-fold. In the last cycle the reconstruction was carried out at finer pixel sampling (1.988 Å). Within each cycle the reconstruction with the highest resolution was used to create new references that were used for a subsequent cycle of alignment. Helical parameters for three-dimensional reconstruction were obtained using the hsearch_lorentz program (Egelman, 2000). The helical rise and angle converged to 9.26 Å and -25.76° respectively. For three-dimensional reconstruction, a recent implementation of a helical symmetry operator in FREALIGN was used (Alushin et al., 2010). In this algorithm, each 80 Å segment is included multiple times in the reconstruction, using the Euler angles and shifts, to generate symmetrically equivalent views. Due to the presence of the seam in the 14 PF MTs, each segment was inserted 14 times. As previously described (Sindelar and Downing, 2007; 2010), the symmetrization step causes the output reconstruction from FREALIGN to contain a single PF with all asymmetric subunits in registry. A SPIDER script was used to rebuild the MT containing the correct seam position, as described (Sindelar and Downing, 2010). Our final reconstruction contains data from 191 MTs equivalent to 10,419 80 Å segments or 145,866 individual tubulin dimers. Visual inspection of our reconstruction after sharpening the map revealed that the resolution for the portion of the map corresponding to the SRS is lower than the portion containing the MT-MTBD interface. We applied a cylindrical soft mask to exclude the density

corresponding to the SRS and measured the resolution of the map in its absence. The resolution of the MT-MTBD map calculated from half volumes of the final reconstruction is 9.7 Å (FSC 0.143 criterion, Fig. A2.1D), which is more consistent with our ability to see secondary structural elements in portions of the map. The final map was sharpened using Gaussian low-pass and high-pass filters at 9.75 and 30 Å, respectively, and the high-resolution amplitudes were scaled using a b-factor of -200 $Å^2$ using the program BFACTOR with the cosine edge mask option with a radius of 9.5 Å.

Flexible fitting and targeted molecular dynamics

Our Experimental 3D map was segmented to obtain a density comprising an asymmetric tubulin dimer unit using UCSF Chimera (Pettersen et al., 2004). The atomic resolution structures for the MTBD (PDB 3ERR (Carter et al., 2008)), excluding 4 residues (3360 to 3363); and tubulin, obtained after flexible fitting into a MT density (Wells and Aksimentiev, 2010), were used for rigid body docking using UCSF Chimera. Molecular dynamics flexible fitting (MDFF) (Trabuco et al., 2008; 2009) and targeted molecular dynamics (TMD) (Schlitter et al., 1994) were utilized to obtain a pseudo-atomic model of the high affinity MTBD-MT complex.

Initially, the MTBD-Tubulin system was minimized for 2000 steps and then a vacuum MDFF simulation was run for 100 ns at 300K, using a dielectric constant of 80 and a force scaling factor (ξ) of 0.5 kcal/mol. Restraints on secondary structure elements and chiral atoms were used as described (Trabuco et al., 2009). After the simulation in vacuum, the system was embedded in a box

of water molecules using the VMD plugin “Solvate” with a 10 Å distance from the closest protein atoms to the box edge. The VMD plugin “Autoionize” was used to randomly place potassium and chloride ions that simulate a final KCl concentration of 0.05 M. All-atom molecular dynamics simulations were performed using the software NAMD 1.7b2 (Phillips et al., 2005), the CHARMM27 force field with CMAP correction terms (Mackerell, 2004) and the TIP3P water model (Jorgensen et al., 1983). The same parameters for the GDP and GTP molecules were used as described (Wells and Aksimentiev, 2010). The system was minimized for 2000 steps followed by 10 ns of MDFF at 300 K using a force-scaling factor (ξ) of 0.5 kcal/mol and constraints on secondary structure elements and chiral atoms. During MDFF simulations, the temperature was kept constant at 300K using Langevin dynamics with a damping coefficient of 5 ps^{-1}. The long-range electrostatic interactions were calculated using the Particle Mesh Ewald method (PME) and the van der Waals interactions were computed with a 10 Å cutoff using periodic boundary conditions. After the MDFF simulation in explicit solvent the system was equilibrated for 10 ns in the NPT ensemble (see below).

After these simulations, we observed a rearrangement of the helices that form the MTBD, with no apparent shift in the registry of the stalk (Fig. A2.2C). As our cryo-EM data was collected with a construct known to exist in the high affinity registry, TMD (Schlitter et al., 1994) was performed on the Cα atoms of residues 3264-3280 using a 200 kcal/mol$Å^2$ force constant. In TMD, the positions of selected atoms are driven into the target positions by using an additional

potential energy term in which the root-mean-squared deviation between the simulated and target position is minimized during the simulation. Using this approach, the registry shift from low- to high-affinity was obtained, whereas the rest of the atoms were still driven by the cryo-EM map using MDFF. Fifteen ns of MDFF/TMD at 300 K using a force-scaling factor (ξ) of 0.5 kcal/mol and constraints on secondary structure elements and chiral atoms were carried out.

To confirm that the structure for the dynein high affinity MTBD state does not depend on the multistep simulations that we carried out, we ran additional simulations as follows: the starting crystal structures of tubulin and the low-affinity MTBD (described above) were rigid body docked into our density, the output system was solvated and ions were randomly placed as described above. The system was minimized for 1000 steps followed by 20 ns of MDFF/TMD at 300 K using a force-scaling factor (ξ) of 0.5 kcal/mol and constraints on secondary structure elements and chiral atoms. A similar high affinity MTBD structure (backbone RMSD 2.4 Å relative to structure on Fig. 2, not shown) was obtained.

Equilibration simulations

After the MDFF/TMD simulations, the system was equilibrated for 20 ns in the NPT ensemble at 300 K and 1 atm using the Nose-Hoover Langevin piston with a 200 fs decay period and a 50 ps^{-1} damping time constant for the pressure and 0.1 ps^{-1} for the temperature. PME was used for long-range electrostatic interactions and a 12 Å cutoff (switching function at 10 Å) for van der Waals interactions. A uniform integration step of 2 fs was used during these simulations.

The backbone coordinates of tubulin and residues 3411 to 3427 in the dynein MTBD were constrained using harmonic forces with a force constant of 1 kcal/mol$Å^2$ to keep fixed the center of mass of the molecules. During the 10 first ns of these simulations, TMD with 100 and 50 kcal/mol$Å^2$ force constants, on the same atoms described above, were used. All TMD constraints were released during the last 10 ns.

Additional simulations were run using the low-affinity MTBD and tubulin structures without any external force, and using TMD to induce the registry shift, both without the presence of our experimental map. The systems were prepared using the tubulin coordinates obtained after equilibration of the high-affinity MTBD-Tubulin complex (see above) and the crystal structure coordinates of the low-affinity construct (PDB 3ERR). The positions of residues 3388 to 3426 were used to align the dynein MTBD low- and high-affinity structures, as they were unchanged in both conformations. The MTBD-tubulin complex coordinates were embedded in a box of explicit water molecules and KCl ions as described above. In the case of the TMD simulations, restraints on secondary structure elements and chiral atoms were used to avoid structural distortions of the protein. Fifteen ns of TMD simulations were carried out with the same parameters as the MDFF/TMD simulation described above. The simulation of the low-affinity MTBD structure on MTs included 100 ps simulation with constraints in all backbone atoms with a force constant of 1 kcal/mol$Å^2$ followed by a 15 ns equilibration simulation in the NPT ensemble as described above. In the absence of the map forces, the repositioning of the helices H1, H3 and H4 was not observed during

the simulated time scale, though favorable interactions between the dynein low-affinity conformation and tubulin were detected (Table A2.2).

Analysis of trajectories

The last 10 ns of equilibration simulations were used to perform trajectory analysis using VMD (Humphrey et al., 1996). The RMSD of the high- and low-affinity MTBD equilibrated structures was measured and its convergence supports the stability of the conformers. Salt bridges were monitored if the donor-acceptor distance was less than 3.2 Å. Hydrogen bonds were counted if the donor-acceptor distance was less than 3.0 Å with a 20° cutoff for the angle formed by the donor, hydrogen, acceptor (Fig. A2.6, Table A2.1). Figures depicting molecular structures were created with UCSF Chimera (Pettersen et al., 2004) and VMD(Humphrey et al., 1996).

Comparison of our experimental high-affinity map with synthetic maps

To compare the conformational changes described by our MD-generated pseudo-atomic models with our experimental density, we generated 10 Å resolution synthetic maps of the low and high affinity conformations using SPIDER and fitted them into our experimental cryo-EM map. At this resolution secondary structure elements such as alpha helices are visible as discrete regions of density in both our synthetic and experimental maps (Fig. A2.3). We calculated the cross-correlation coefficient between each of the synthetic maps and our experimental cryo-EM map (Trabuco et al., 2009). The higher similarity

between the synthetic map of the high-affinity state and our experimental density (CCC 0.751) when compared to the low-affinity conformation (CCC 0.648) indicates that our map describes the large conformational changes seen in our pseudo-atomic models. In particular, the density corresponding to H1 in the low-affinity synthetic map is completely absent in our experimental EM density, whereas the high-affinity synthetic map shows a very good match to the experimental density.

Flexible fitting of Kon et al. MTBD

We performed MDFF using our EM map and the atomic coordinates of the MTBD of an ADP-bound dynein monomer (PDB 3VKH (Kon et al., 2012b)). This structure has the stalk's coiled-coil in the a registry but its MTBD has the same conformation as the low-affinity MTBD previously reported by Carter et al. (Carter et al., 2008). The crystal structures of MDFF tubulin (described above) and the MTBD (residues 3352 to 3491) were rigid-body docked into our density, the initial coordinates for the complex were solvated, and ions were randomly placed as described above. The system was minimized for 2000 steps followed by 12 ns of MDFF at 300 K using a force-scaling factor (ξ) of 0.5 kcal/mol and constraints on secondary structure elements and chiral atoms. A similar high-affinity conformation for the MTBD region (backbone RMSD 3.3 Å relative to residues 3285 to 3402 in the high-affinity conformation described above in this study) was obtained (Fig. A2.4). During this simulation we observed that the final position of CC1 deviates from the one observed in our previous simulations, likely because

of the absence of coordinates for the CC2 residues in the distal portion of the coiled-coil of the crystal structure reported by Kon et al.

Two-dimensional analysis of monomeric *S. cerevisiae* dynein bound to microtubules

Monomeric dynein protein was purified as described for dimeric dynein (Reck-Peterson et al., 2006), bound to MTs, and imaged under cryogenic conditions. MTs were polymerized and grids were prepared as described above. Images were collected on a US4000 4k x 4k CCD (Gatan) in a Tecnai F20 electron microscope (FEI) operating at 200 keV, and nominal magnification of 50,000. Square segments of 600 x 600 pixels with 80 % overlap were extracted and alignment and classification of data binned by 3 (final pixel size of 6.42 Å) was performed using a previously reported strategy (Ramey et al., 2009).

Estimating the conformation of monomeric dynein on microtubules

We noticed that rigid body docking of the Kon et al. dynein monomer crystal structure (Kon et al., 2012a) via its MTBD into our reconstruction results in the dynein head clashing with the MT (Fig. A2.4D). Using our MDFF-generated Kon et al. MTBD (described above) (Fig. A2.4B) we ran additional targeted molecular dynamics simulations to position CC1 according to our high-affinity model (to correct for the deviation in CC1 due to the absence of CC2 in the Kon et al. structure). We then modeled the structure of the entire monomer using the remaining portion of the monomer crystal structure (PDB 3VKH).

S. cerevisiae strain construction

Mutations were inserted into a truncated dynein construct that is dimerized with GST as described previously (Reck-Peterson et al., 2006). All mutations were verified by DNA sequencing. The wild type form of this construct has been shown to have near identical properties as full-length cytoplasmic dynein (Reck-Peterson et al., 2006).

Yeast dynein purification

Cultures of *S. cerevisiae* for protein purification were grown, harvested, and frozen as previously described (Reck-Peterson et al., 2006). Dynein constructs were purified via their ZZ tags and labeled with HaloTag-TMR (Promega) as described (Reck-Peterson et al., 2006).

Total Internal Reflection Fluorescence Microscopy (TIRF)

Fluorescently-labeled molecules were visualized using an Olympus IX-81 TIRF microscope with a 100X 1.45 N.A. oil immersion TIRF objective (Olympus) and two CW diode-pumped solid state lasers (491nm and 561nm, Cobolt). Laser power at the objective was 1.5 – 2 mW. Images were recorded with a 100 ms exposure on a back-thinned electron multiplier CCD camera (Hamamatsu), controlled by Metamorph software.

Single-molecule motility assays of mutant dyneins (Fig. 2.5) were performed with MTs containing HiLyte Fluor™ 488- and biotin-labeled tubulin

(Cytoskeleton, Inc.). MTs were prepared as described (Qiu et al., 2012). Single-molecule motility assays that addressed the effect of increasing ionic strength on dynein motility (Fig. A2.7) utilized Cy5-labeled axonemes prepared as described (Reck-Peterson et al., 2006). All assays utilized a flow chamber as described (Case et al., 1997; Reck-Peterson et al., 2006), with the following modification: TMR-labeled dynein motors were added to motility chambers in the presence of motility buffer [30 mM HEPES (pH 7.2), 2 mM MgOAc, 1 mM EGTA, 10% glycerol, 1 mM DTT, 1 mM Mg-ATP, and an oxygen scavenger system] (Reck-Peterson et al., 2006). To determine the effect of ionic strength on dynein motility, assay buffer was supplemented with 20, 40, 60, or 80 mM KAc (Fig. A2.7), or 50 mM KAc (Fig. 2.5A, B, and Fig. A2.9, A2.10), or 50 mM KAc + 50 mM KCl (Fig. A2.11). Images were recorded every 2 s for 10 min, and velocities and run lengths were calculated from kymographs generated in ImageJ (NIH) as described (Reck-Peterson et al., 2006). Run lengths were not corrected for photobleaching of fluorophores, as this rate was determined to be negligible (data not shown).

Preparation of tubulin lacking C-terminal E-hooks

Polymerized biotin-labeled MTs (described above) were incubated with subtilisin at the ratio of 5:1 (w/w of tubulin:subtilisin) for 1 h at 37°C. The reaction was stopped by adding 2 mM phenylmethylsulfonyl fluoride (PMSF). The digestion was monitored by SDS-PAGE to confirm complete cleavage. TIRF microscopy with subtilisin treated MTs was performed as described above.

Results and Discussion

We collected images of MTs highly decorated with the SRS-MTBD under cryogenic conditions (Fig. 2.2A, Fig. A1.1A), and adapted an image processing method (Sindelar and Downing, 2007; 2010) to solve its structure bound to 14-protofilament MTs. The SRS-MTBD binds to α-tubulin and β-tubulin at the intradimer interface and is positioned to the side of the protofilament, as previously reported (Carter et al., 2008; Mizuno et al., 2004) (Fig. 2.2B, Fig. A1.1B). In the reconstruction, the portion including the MT, the MTBD and the beginning of the stalk has a resolution of 9.7 Å (Fig. A1.1D), where α-helices become visible.

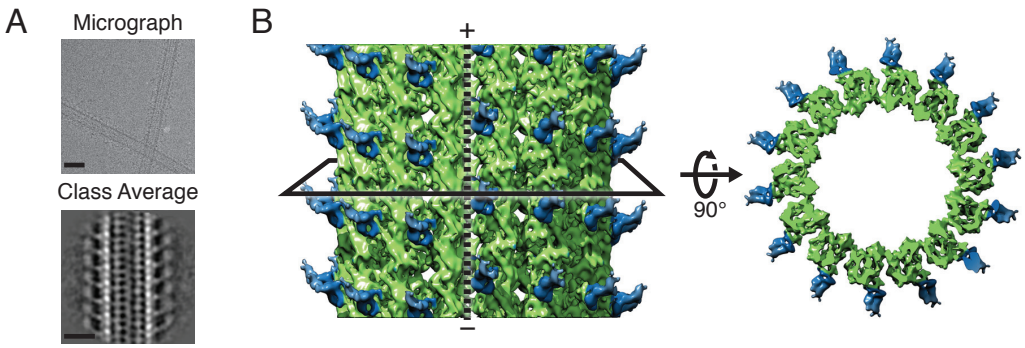

Figure 2.2 Cryo-EM reconstruction of the cytoplasmic dynein high-affinity MTBD bound to a MT
(A) Cryo-EM image of MTs highly decorated with the high-affinity SRS-MTBD construct (top) and a class average generated from segments of decorated 14-protofilament MTs (bottom). Scale bars: 25 nm. (B) Three-dimensional reconstruction of the MTBD-MT complex, filtered to the calculated resolution of 9.7 Å (Fig. A1.1). The black solid line represents a slice through the volume, which is shown on the right viewed from the minus end of the MT. The MT polarity is indicated and the dashed line shows the location of the MT seam. The SRS has been omitted due to its lower resolution (Fig. A1.1).

We used molecular dynamics (MD) and our cryo-EM reconstruction to obtain pseudo-atomic models of the low- and high-affinity states of the MTBD bound to MTs. First, we rigid-body docked the atomic-resolution structures of the tubulin dimer (Löwe et al., 2001; Wells and Aksimentiev, 2010) and the low-affinity MTBD into our map (Figs. 2A, C, and A2.2A) and used MD to resolve steric clashes between a helix (H1) in the MTBD and the MT (Figs. 2A, C and A2.2A, B). We then performed explicit-solvent molecular dynamics flexible fitting (MDFF) to shift the low-affinity MTBD structure to the high-affinity conformation in our reconstruction (Fig. A1.2C). In addition to the MD force field, MDFF uses a potential energy term derived from the experimental map and restraints on secondary structure to drive conformational changes that better fit the map (Trabuco et al., 2008; 2009). The initial MDFF model agreed well within the experimental density of the MTBD (Fig. A1.2C); however, the stalk remained in the low-affinity β+ registry present in the starting model. MDFF likely did not shift the registry of the coiled-coil due to the lower resolution at the tip of the stalk segment (Fig. A1.1); a movement of the CC1 helix to the α registry would make it protrude from the map, incurring a penalty in the simulations. We achieved the shift by applying targeted molecular dynamics (TMD) (Schlitter et al., 1994) to the tip of the coiled-coil (Fig. A1.2D), using the Cα coordinates of the half-heptad shift in our construct to guide the final position of the stalk during the simulations. This final model (Fig. 2.3B, D), which we refer to as the high-affinity MTBD, has the highest cross-correlation with the experimental map (Figs. A2.2 and A2.3).

We repeated the MDFF calculations using the MTBD from the recent

crystal structure of an ADP-bound dynein monomer (Kon et al., 2012a) (Fig. A1.4). The only difference in the resulting pseudo-atomic model is in the stalk, where the dynein monomer's structure is missing density for one of the helices next to the MTBD (Fig. A1.4A, B). The similarity in the crystal structures of the MTBD in the low-affinity and ADP-bound states is likely due to the absence of

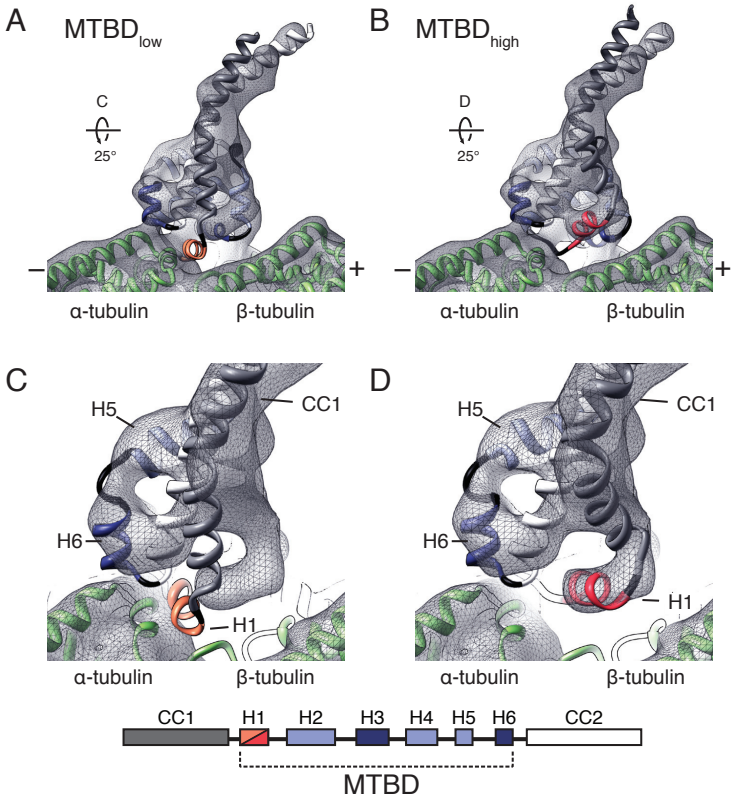

Figure 2.3 The high-affinity, MT-bound state of the dynein MTBD is characterized by the repositioning of helices H1 and CC1

(**A**) Rigid-body docking of the low-affinity MTBD structure into our cryo-EM density. (**B**) Pseudo-atomic model of the high-affinity MTBD bound to MTs generated by Molecular Dynamics Flexible Fitting (MDFF) and Targeted Molecular Dynamics (TMD) (see text for details). (**C**) Close-up of the structure shown in (A), with its orientation indicated in panel (A). (**D**) Close-up of the structure shown in (B), with its orientation indicated in panel (B). The cryo-EM map is shown as a transparent grey mesh. The MTBD is colored following the scheme shown at the bottom of the figure and structural elements are indicated in the different views. H1 (orange/red) is the element with the largest movement in the transition to the high-affinity conformation; H3 and H6 (dark blue) are major contact points with the MT (green). α- and β-tubulin are indicated (green). MT polarity is indicated in panels A and B. H1 protrudes from the cryo-EM map and clashes with the MT in the rigid-body docked low-affinity state (A and C).

MTs; our results suggest that the conformation we observe in our MT-bound high-affinity structure is stabilized by its interactions with β-tubulin (Fig. A1.5A, Tables A2.1 and A2.2). MDFF of the ADP-bound dynein monomer's MTBD into our cryo-EM map results in a large change in the angle between the MTBD and the stalk in the dynein monomer structure (Fig. A1.4A, B). This change makes the docking of the dynein monomer into our map compatible with previously reported measurements of the MT-stalk angle (Carter et al., 2008; Mizuno et al., 2004) and our two-dimensional analysis of images of monomer-decorated MTs (Fig. A1.4D, E).

The cryo-EM map shows three points of continuous density between the MT and dynein's MTBD: the H1-H2 loop and helices H3 and H6 (Fig. 2.3B). Several parts of the structure are unchanged by its interaction with the MT, especially helices H6, H5, and CC2, with root mean square deviations (RMSD) between the low- and high-affinity models of 1.4 Å, 1.4 Å, and 1.8 Å, respectively. The largest changes are the repositioning of H1 (RMSD = 10.1 Å) and an opening of CC1 in the coiled-coil next to the MTBD (RMSD = 8.1 Å) (Fig. 2.3A-D), a movement anchored at the proline kink present in CC1. The final position of H1 is stabilized by multiple interactions with an acidic patch in H12 of β-tubulin not fully occupied in the low-affinity state (Fig. A1.5A). This patch also stabilizes the high-affinity state of kinesin (Uchimura et al., 2010).

We monitored hydrogen bonds and salt bridges formed between the MTBD and the MT during MD simulations (Tables A2.1 and A2.2); the high-affinity MTBD formed more hydrogen bonds with the MT (Fig. A1.6) and

electrostatic interactions at H1, H3, and H6 (Fig. A1.5, Table A2.1). Nearly all of these residues are highly conserved, and mutating them results in defects in MT binding (Gibbons et al., 2005; Koonce and Tikhonenko, 2000) (Fig. A1.5). The importance of salt bridges to the MTBD-MT interaction is consistent with the sensitivity of dynein's motility to ionic strength (Fig. A1.7).

Our structural analysis suggested that the MTBD contains residues that lower its own affinity for the MT. In the MD simulations, basic residues in H1 and H6 formed salt bridges that alternated between intramolecular and intermolecular partners. In the MT-bound high-affinity conformation, H1-K3298 switched between a glutamate on β-tubulin and a conserved glutamate in CC1 (E3289) (Figs. 2.4A, A2.8A); neither contact can be formed by H1-K3298 in the low-affinity conformation (Fig. A1.5A). H6-R3382 switched from an intramolecular interaction with a conserved glutamate in the same helix (H6-E3378) in the low-affinity unbound state to an intermolecular interaction with a cluster of glutamates on α-tubulin upon binding (Fig. 2.4B, A2.8B); the intramolecular interaction might weaken the MTBD-MT interaction in both the low- and high-affinity conformations. The importance of the two MTBD glutamates involved in the intramolecular salt bridges had previously been recognized; substitution of CC1-E3289 and H6-E3378 with alanine increased dynein's MT-binding affinity (Gibbons et al., 2005; Koonce and Tikhonenko, 2000) and reduced its ATP-stimulated release from MTs, respectively (Koonce and Tikhonenko, 2000). We hypothesized that these phenotypes resulted from the competition between MT and MTBD residues in CC1 and H6 for salt bridge formation with the basic

residues K3298 and R3382 in the MTBD.

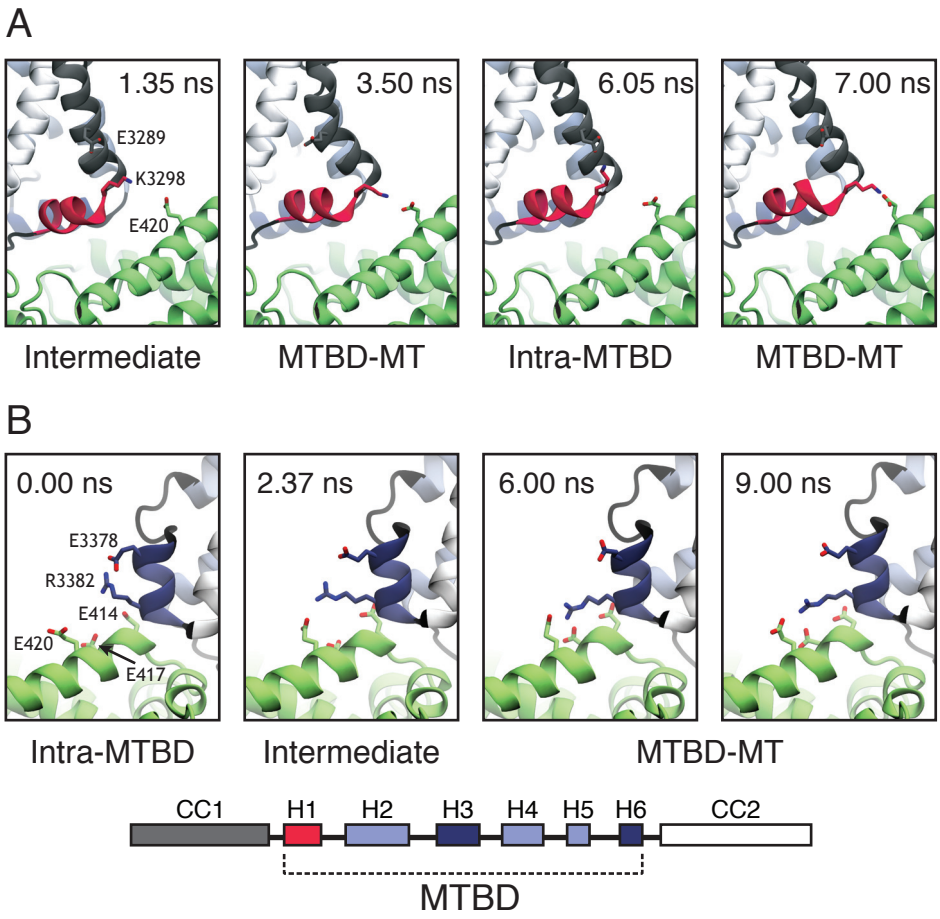

Figure 2.4 Behavior of dynamic salt bridges in the MTBD as determined by MD

(**A**) K3298 in H1 of the MTBD alternates between an intermolecular salt bridge with E420 on β-tubulin (MTBD-MT) and an intramolecular salt bridge with E3289 on CC1 of the MTBD (intra-MTBD). (**B**) R3382 in H6 of the MTBD alternates between an intermolecular salt bridge with E414 and E420 on α-tubulin (MTBD-MT) and an intramolecular salt bridge with E3378 in H6 (intra-MTBD). Single letter amino acid code and number are indicated for *Bos taurus* tubulin and *Mus musculus* cytoplasmic dynein. Time stamps for frames from MD simulations are indicated. Intermediate refers to a position midway between MTBD-MT and intra-MTBD salt bridges.

To test this prediction we mutated the residues equivalent to E3289 and E3378 in CC1 and H6 of *Saccharomyces cerevisiae* dynein to either an isosteric but neutral (Q) or a basic amino acid (K) to disrupt the salt bridge (Q) or introduce an intramolecular charge repulsion (K) that may favor intermolecular

interactions between H1-K3298 or H6-R3382 and acidic residues on the MT surface. Single molecule motility assays that monitored the movement of purified mutant dyneins showed significant increases in dynein's run length and small decreases in velocity that paralleled the severity of the mutation (E -> Q -> K) (Fig. 2.5A, B and Fig. A1.9). Most dramatically, the basic substitutions CC1-E3289K and H6-E3378K increased dynein's run length by five-fold and six-fold, respectively (Fig 4B), and the double mutant even further (Fig. A1.10). These results suggest that cytoplasmic dynein has been selected for sub-maximal processivity. The effects observed with the mutants are not due to a strengthened interaction with the unstructured carboxyl-terminal tails of tubulin (E-hooks). Although their removal decreased the run length of all constructs tested, in agreement with previous studies (Wang and Sheetz, 2000), the trend of increasing processivity (WT -> E3289K -> E3378K) remained (Fig. A1.11).

These findings provide a molecular model for how dynein couples its affinity for MTs with the nucleotide state of the motor domain (Fig. 2.5C-E). We describe the transition from low to high affinity, but suggest that the proposed changes are reversible. During a diffusive search for its next binding site (Fig. 2.5C) an unbound MTBD is in the low-affinity conformation with its stalk in the β+ registry, H1 oriented perpendicular to the MT axis and intramolecular salt bridges at key MT-binding residues. Consistent with this, an NMR study found that an unconstrained, minimal MTBD in solution exists in the β+ registry and displays low affinity for MTs (McNaughton et al., 2010). Upon binding (Fig. 2.5D), transition to a high-affinity conformation involves a large displacement of H1,

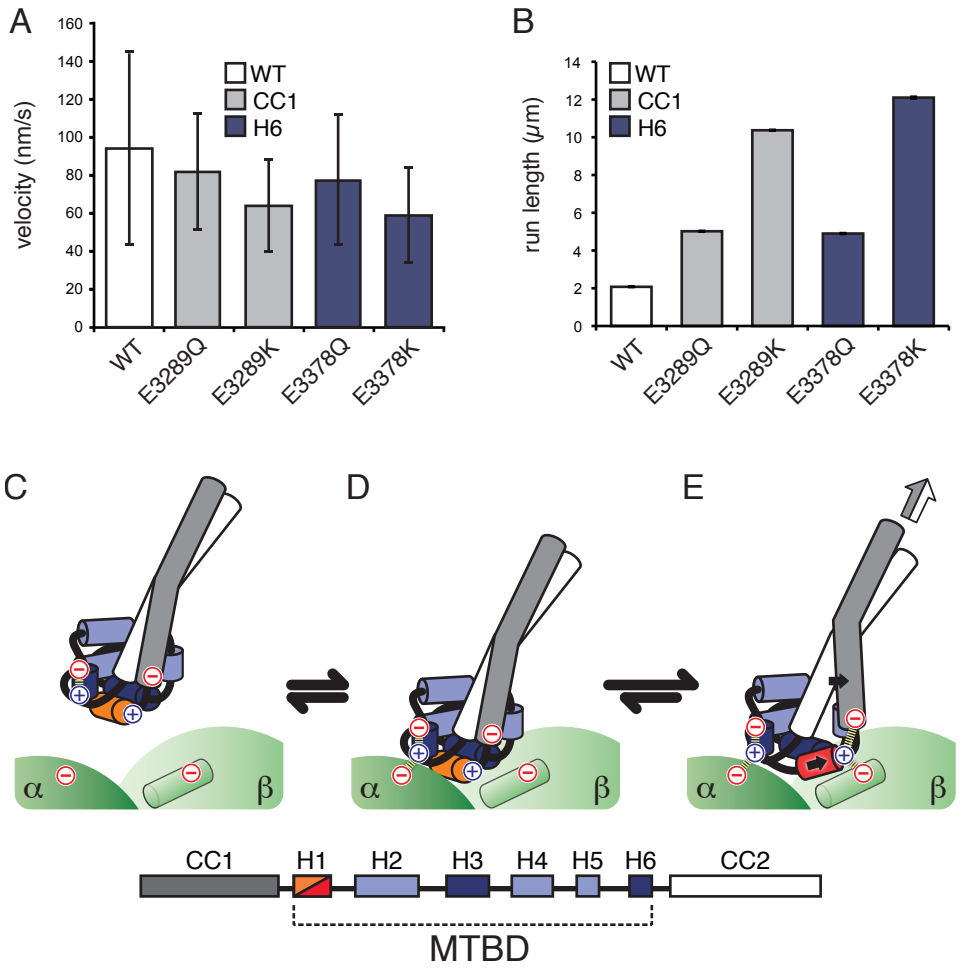

Figure 2.5 Dynamic salt bridges reduce dynein motility

Bar graphs of (**A**) mean velocities and (**B**) characteristic run lengths of fluorescently labeled *Saccharomyces cerevisiae* dynein bearing the equivalent of the indicated *Mus musculus* mutations moving on MTs. Error bars: standard deviation, SD (A) and standard error of the mean, SE (B). Velocity and run length differences between WT and Q mutants, as well as between Q and K mutations at the same position, are statistically significant (t-test, $P < 0.01$ for velocity, and two-tailed KS-test, $P < 0.01$ for run length). The data for the double mutant (E->K at both CC1 and H6) was omitted because run lengths could only be determined under more stringent motility conditions (Fig. A1.10). (**C-E**) Molecular model for the coordination of nucleotide state and MT binding by dynein (see text for details). (**C**) Unbound dynein in the low affinity conformation, H1 is colored orange. (**D**) Initial interaction with a new binding site. (**E**) Repositioning of H1 (now in red) leads to the formation of new ionic interactions with β-tubulin (green cylinder) that stabilize the high-affinity state of the MTBD. The repositioning of H1 is accompanied by a movement in CC1; both movements are indicated by solid black arrows. The conformational change in the MTBD biases the registry of the coiled-coil towards the high-affinity a state, a change that can propagate to the motor domain (white/grey arrow). Ionic interactions are indicated with dashed lines. The identities of the helices in the MTBD are indicated by the key.

stabilized by new salt bridges with β-tubulin, and an opening of CC1 at the base of the stalk (Fig. 2.5E). The movements of H1 and CC1 likely constraint the registries that can be explored by the stalk, biasing the distribution towards the high-affinity α registry (Fig. 2.5E). Propagation of this signal to the head would elicit conformational changes that produce a movement of the linker domain, and a displacement of dynein towards the MT minus end.

Our analysis of dynamic salt bridges reveals that cytoplasmic dynein has been selected for sub-maximal processivity. While kinesin has diversified its functional repertoire through gene duplication and divergence (Dagenbach and Endow, 2004), cytoplasmic dynein is expressed from a single locus and may have evolved sub-optimal processivity to increase the dynamic range of its regulation. High processivity could also be detrimental when multiple dyneins and kinesins must balance their actions on a single cargo (Welte, 2004). Consistent with this idea, intraflagellar dyneins, responsible for long, unidirectional transport within cilia (Iomini et al., 2001; Laib et al., 2009), contain neutral or basic residues at the equivalent of H6-E3378 (Fig. A1.12), which would likely increase their processivity.

Acknowledgements

We thank A. Carter (LMB-MRC) for reagents and advice, C. Sindelar (Yale), V. Ramey (UC Berkeley), E. Egelman (U of Virginia), and R. Sinkovits (UCSD) for sharing processing scripts and helpful advice, M. Sotomayor (Harvard) and R. Gaudet (Harvard) for advice concerning MD, J. Hogle (Harvard), M. Strauss

(Harvard) and M. Wolf (OIST) for help with film and the use of a film scanner, E. Nogales (UC-Berkeley), N. Francis (Harvard), and D. Pellman (Harvard) for critically reading the manuscript, as well as all the members of the Leschziner and Reck-Peterson Labs for advice and helpful discussions. EM data was collected at the Center for Nanoscale Systems (CNS), a member of the National Nanotechnology Infrastructure Network (NNIN), which is supported by the National Science Foundation under NSF award no. ECS-0335765. CNS is part of Harvard University. MD simulations were run on the Odyssey cluster supported by the FAS Science Division Research Computing Group, Harvard University. SRP is funded by the Rita Allen Foundation, the Harvard Armenise Foundation, and a NIH New Innovator award (1 DP2 OD004268-1). AEL was funded in part by a Research Fellowship from the Alfred P. Sloan Foundation. RHL was supported in part by CONACYT and Fundacion Mexico en Harvard. The cryo-EM map was deposited at the EM Data Bank (EMDB-5439) and pseudo-atomic models at the Protein Data Bank (PDB-3J1T and -3J1U).

References

Alushin, G.M., Ramey, V.H., Pasqualato, S., Ball, D.A., Grigorieff, N., Musacchio, A., and Nogales, E. (2010). The Ndc80 kinetochore complex forms oligomeric arrays along microtubules. Nature *467*, 805–810.

Burgess, S.A., Walker, M.L., Sakakibara, H., Knight, P.J., and Oiwa, K. (2003). Dynein structure and power stroke. Nature *421*, 715–718.

Carter, A.P., Cho, C., Jin, L., and Vale, R.D. (2011). Crystal structure of the dynein motor domain. Science *331*, 1159–1165.

Carter, A.P., Garbarino, J.E., Wilson-Kubalek, E.M., Shipley, W.E., Cho, C., Milligan, R.A., Vale, R.D., and Gibbons, I.R. (2008). Structure and functional role

of dynein's microtubule-binding domain. Science *322*, 1691–1695.

Case, R.B., Pierce, D.W., Hom-Booher, N., Hart, C.L., and Vale, R.D. (1997). The directional preference of kinesin motors is specified by an element outside of the motor catalytic domain. Cell *90*, 959–966.

Dagenbach, E.M., and Endow, S.A. (2004). A new kinesin tree. Journal of Cell Science *117*, 3–7.

Egelman, E.H. (2000). A robust algorithm for the reconstruction of helical filaments using single-particle methods. Ultramicroscopy *85*, 225–234.

Gee, M.A., Heuser, J.E., and Vallee, R.B. (1997). An extended microtubule-binding structure within the dynein motor domain. Nature *390*, 636–639.

Gibbons, I.R. (1995). Dynein family of motor proteins: present status and future questions. Cell Motil. Cytoskeleton *32*, 136–144.

Gibbons, I.R., Garbarino, J.E., Tan, C.E., Reck-Peterson, S.L., Vale, R.D., and Carter, A.P. (2005). The affinity of the dynein microtubule-binding domain is modulated by the conformation of its coiled-coil stalk. Journal of Biological Chemistry *280*, 23960–23965.

Gibbons, I.R., Gibbons, B.H., Mocz, G., and Asai, D.J. (1991). Multiple nucleotide-binding sites in the sequence of dynein beta heavy chain. Nature *352*, 640–643.

Grigorieff, N. (2007). FREALIGN: high-resolution refinement of single particle structures. J. Struct. Biol. *157*, 117–125.

Grigorieff, N., and Harrison, S.C. (2011). Near-atomic resolution reconstructions of icosahedral viruses from electron cryo-microscopy. Current Opinion in Structural Biology *21*, 265–273.

Höök, P., and Vallee, R.B. (2006). The dynein family at a glance. Journal of Cell Science *119*, 4369–4371.

Humphrey, W., Dalke, A., and Schulten, K. (1996). VMD: visual molecular dynamics. Journal of Molecular Graphics *14*, 33–38, 27.

Iomini, C., Babaev-Khaimov, V., Sassaroli, M., and Piperno, G. (2001). Protein particles in Chlamydomonas flagella undergo a transport cycle consisting of four phases. The Journal of Cell Biology *153*, 13–24.

Jorgensen, W.L., Chandrasekhar, J., Madura, J.D., Impey, R.W., and Klein, M.L. (1983). Comparison of simple potential functions for simulating liquid water. J. Chem. Phys. *79*, 926–935.

Kon, T., Imamula, K., Roberts, A.J., Ohkura, R., Knight, P.J., Gibbons, I.R., Burgess, S.A., and Sutoh, K. (2009). Helix sliding in the stalk coiled coil of dynein couples ATPase and microtubule binding. Nat. Struct. Mol. Biol. *16*, 325–333.

Kon, T., Nishiura, M., Ohkura, R., Toyoshima, Y.Y., and Sutoh, K. (2004). Distinct Functions of Nucleotide-Binding/Hydrolysis Sites in the Four AAA Modules of Cytoplasmic Dynein †. Biochemistry *43*, 11266–11274.

Kon, T., Oyama, T., Shimo-Kon, R., Imamula, K., Shima, T., Sutoh, K., and Kurisu, G. (2012a). The 2.8 Å crystal structure of the dynein motor domain. Nature *484*, 345–350.

Kon, T., Oyama, T., Shimo-Kon, R., Imamula, K., Shima, T., Sutoh, K., and Kurisu, G. (2012b). The 2.8 Å crystal structure of the dynein motor domain. Nature *484*, 345–350.

Kon, T., Sutoh, K., and Kurisu, G. (2011). X-ray structure of a functional full-length dynein motor domain. Nat. Struct. Mol. Biol. *18*, 638–642.

Koonce, M.P. (1997). Identification of a microtubule-binding domain in a cytoplasmic dynein heavy chain. The Journal of Biological Chemistry *272*, 19714–19718.

Koonce, M.P., and Tikhonenko, I. (2000). Functional elements within the dynein microtubule-binding domain. Molecular Biology of the Cell *11*, 523–529.

Laib, J.A., Marin, J.A., Bloodgood, R.A., and Guilford, W.H. (2009). The reciprocal coordination and mechanics of molecular motors in living cells. Proceedings of the National Academy of Sciences of the United States of America *106*, 3190–3195.

Löwe, J., Li, H., Downing, K.H., and Nogales, E. (2001). Refined structure of alpha beta-tubulin at 3.5 A resolution. Journal of Molecular Biology *313*, 1045–1057.

Ludtke, S.J., Baldwin, P.R., and Chiu, W. (1999). EMAN: semiautomated software for high-resolution single-particle reconstructions. J. Struct. Biol. *128*, 82–97.

Mackerell, A.D. (2004). Empirical force fields for biological macromolecules: overview and issues. Journal of Computational Chemistry *25*, 1584–1604.

McNaughton, L., Tikhonenko, I., Banavali, N.K., LeMaster, D.M., and Koonce, M.P. (2010). A low affinity ground state conformation for the Dynein microtubule binding domain. The Journal of Biological Chemistry *285*, 15994–16002.

Mindell, J.A., and Grigorieff, N. (2003). Accurate determination of local defocus and specimen tilt in electron microscopy. J. Struct. Biol. *142*, 334–347.

Mizuno, N., Toba, S., Edamatsu, M., Watai-Nishii, J., Hirokawa, N., Toyoshima, Y.Y., and Kikkawa, M. (2004). Dynein and kinesin share an overlapping microtubule-binding site. The EMBO Journal *23*, 2459–2467.

Pettersen, E.F., Goddard, T.D., Huang, C.C., Couch, G.S., Greenblatt, D.M., Meng, E.C., and Ferrin, T.E. (2004). UCSF Chimera--a visualization system for exploratory research and analysis. Journal of Computational Chemistry *25*, 1605–1612.

Phillips, J.C., Braun, R., Wang, W., Gumbart, J., Tajkhorshid, E., Villa, E., Chipot, C., Skeel, R.D., Kalé, L., and Schulten, K. (2005). Scalable molecular dynamics with NAMD. Journal of Computational Chemistry *26*, 1781–1802.

Qiu, W., Derr, N.D., Goodman, B.S., Villa, E., Wu, D., Shih, W., and Reck-Peterson, S.L. (2012). Dynein achieves processive motion using both stochastic and coordinated stepping. Nat. Struct. Mol. Biol. *19*, 193–200.

Ramey, V.H., Wang, H.-W., and Nogales, E. (2009). Ab initio reconstruction of helical samples with heterogeneity, disorder and coexisting symmetries. J. Struct. Biol. *167*, 97–105.

Reck-Peterson, S.L., and Vale, R.D. (2004). Molecular dissection of the roles of nucleotide binding and hydrolysis in dynein's AAA domains in Saccharomyces cerevisiae. Proceedings of the National Academy of Sciences of the United States of America *101*, 1491–1495.

Reck-Peterson, S.L., Yildiz, A., Carter, A.P., Gennerich, A., Zhang, N., and Vale, R.D. (2006). Single-molecule analysis of dynein processivity and stepping behavior. Cell *126*, 335–348.

Roberts, A.J., Numata, N., Walker, M.L., Kato, Y.S., Malkova, B., Kon, T., Ohkura, R., Arisaka, F., Knight, P.J., Sutoh, K., et al. (2009). AAA+ Ring and linker swing mechanism in the dynein motor. Cell *136*, 485–495.

Schlitter, J., Engels, M., and Krüger, P. (1994). Targeted molecular dynamics: a new approach for searching pathways of conformational transitions. Journal of Molecular Graphics *12*, 84–89.

Shima, T., Kon, T., Imamula, K., Ohkura, R., and Sutoh, K. (2006). Two modes of microtubule sliding driven by cytoplasmic dynein. Proceedings of the National Academy of Sciences of the United States of America *103*, 17736–17740.

Sindelar, C.V., and Downing, K.H. (2007). The beginning of kinesin's force-generating cycle visualized at 9-A resolution. The Journal of Cell Biology *177*, 377–385.

Sindelar, C.V., and Downing, K.H. (2010). An atomic-level mechanism for activation of the kinesin molecular motors. Proceedings of the National Academy

of Sciences of the United States of America *107*, 4111–4116.

Trabuco, L.G., Villa, E., Mitra, K., Frank, J., and Schulten, K. (2008). Flexible fitting of atomic structures into electron microscopy maps using molecular dynamics. Structure (London, England : 1993) *16*, 673–683.

Trabuco, L.G., Villa, E., Schreiner, E., Harrison, C.B., and Schulten, K. (2009). Molecular dynamics flexible fitting: a practical guide to combine cryo-electron microscopy and X-ray crystallography. Methods (San Diego, Calif.) *49*, 174–180.

Uchimura, S., Oguchi, Y., Hachikubo, Y., Ishiwata, S., and Muto, E. (2010). Key residues on microtubule responsible for activation of kinesin ATPase. The EMBO Journal *29*, 1167–1175.

Vale, R.D. (2003). The molecular motor toolbox for intracellular transport. Cell *112*, 467–480.

Vallee, R.B., Seale, G.E., and Tsai, J.-W. (2009). Emerging roles for myosin II and cytoplasmic dynein in migrating neurons and growth cones. Trends in Cell Biology *19*, 347–355.

Vallee, R.B., Williams, J.C., Varma, D., and Barnhart, L.E. (2004). Dynein: An ancient motor protein involved in multiple modes of transport. Journal of Neurobiology *58*, 189–200.

Wang, Z., and Sheetz, M.P. (2000). The C-terminus of tubulin increases cytoplasmic dynein and kinesin processivity. Biophysical Journal *78*, 1955–1964.

Wells, D.B., and Aksimentiev, A. (2010). Mechanical properties of a complete microtubule revealed through molecular dynamics simulation. Biophysical Journal *99*, 629–637.

Welte, M.A. (2004). Bidirectional transport along microtubules. Current Biology *14*, R525–R537.

Zhang, X., Settembre, E., Xu, C., Dormitzer, P.R., Bellamy, R., Harrison, S.C., and Grigorieff, N. (2008). Near-atomic resolution using electron cryomicroscopy and single-particle reconstruction. Proceedings of the National Academy of Sciences of the United States of America *105*, 1867–1872.

Chapter 3 : Lis1 regulates dynein by sterically blocking its mechanochemical cycle

Sirui Zou*, Katerina Toropova*, Anthony Roberts, William Redwine, Brian Goodman, Samara Reck-Peterson and Andres E. Leschziner

Contributions

Sirui Zou and Katerina Toropova contributed equally. Sirui Zou, Katerina Toropova, Anthony Roberts, Samara Reck-Peterson and Andres Leschziner designed the experiments. Sirui Zou performed and analyzed FRET experiments and single-molecule assays. Katerina Toropova performed and analyzed 3D EM-reconstitution, ATPase activity assay and mutagenesis identifying the interface of dynein-Lis1 complex. William Redwine performed and analyzed in-vivo spindle oscillation assay. Brian Goodman wrote the tracking scripts to analyze the data of spindle oscillation assay. This work was published in: Lis1 regulates dynein by sterically blocking its mechanochemical cycle, *eLIFE* 3:e03372 (2014).

Abstract

Regulation of cytoplasmic dynein's motor activity is essential for diverse eukaryotic functions, including cell division, intracellular transport and development. The dynein regulator Lis1 is known to keep dynein bound to microtubules; however, how this is accomplished mechanistically remains unknown. We have used three-dimensional electron microscopy, single-molecule imaging, biochemistry and *in vivo* assays to establish this mechanism. The three-dimensional structure of the dynein-Lis1 complex shows that binding of Lis1 to dynein's AAA+ ring sterically prevents dynein's main mechanical element, the "linker", from making critical interactions with the ring. Single-molecule experiments show that eliminating this block by shortening the linker to a point where it can physically bypass Lis1 renders single dynein motors insensitive to regulation by Lis1. Our data reveal that Lis1 keeps dynein in a persistent microtubule-bound state by directly blocking the progression of its mechanochemical cycle.

Introduction

Cytoplasmic dynein ("dynein" here), the largest and least understood of the cytoskeletal motors, uses the energy from ATP hydrolysis to move towards the minus ends of microtubules (Carter, 2013; Gibbons et al., 1987; Vale, 2003). As the major minus-end-directed motor in most eukaryotic cells, dynein's many roles include transporting a range of macromolecular cargo (Blocker et al., 1997; Driskell et al., 2007; Jordens et al., 2001; Kon et al., 2004; Kural et al., 2005; Pilling et al., 2006), constructing and positioning the mitotic spindle (Cho et al., 2008; Heald et al., 1996; Kiyomitsu and Cheeseman, 2013; Merdes et al., 1996), and polarizing and anchoring mRNAs during development (Schmidt et al., 2012; Wilkie and Davis, 2001). To perform its diverse biological functions, dynein partners with a range of regulatory co-factors, an important subset of which can alter dynein motility directly. Despite progress in understanding the architecture and mechanism of dynein's large motor domain, how this structure is acted upon by regulatory factors is not yet known.

Dynein is a homodimer of force generating units (~500 kDa each) (Fig. 3.1A,B). The N-terminal region of each monomer forms the "tail" domain, which mediates dimerization and cargo attachment via adaptor proteins. Removal of the tail yields the "motor", the minimal portion of dynein that can exert force. At the core of the motor are six AAA+ modules (AAA1–6) that fold into a ring. AAA1 is the main site of ATP hydrolysis for motility but AAA2, 3 and 4 can also bind ATP and AAA3 and 4 can hydrolyze it (Cho et al., 2008; Gibbons et al., 1991; Kon et al., 2004; 2012; Schmidt et al., 2012). AAA5 and AAA6 have lost the ability to bind nucleotide (Kon et al., 2012; Schmidt et al., 2012). Two

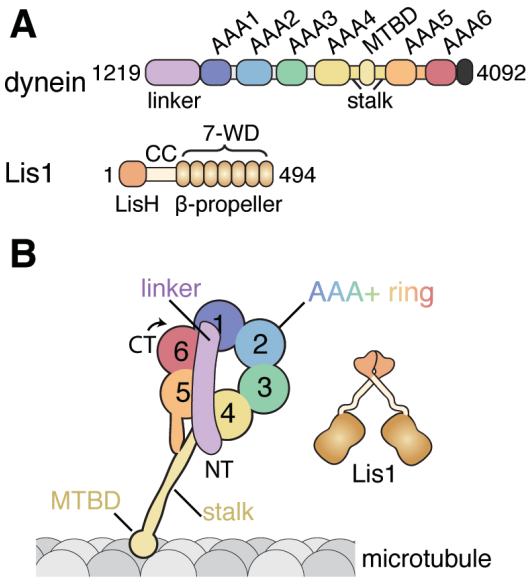

Figure 3.1 Overview of dynein and Lis1 structure
(A) Domain organization of dynein and Lis1 constructs used in this study. Dynein's AAA+ domains are labeled AAA1–6. MTBD: microtubule-binding domain; CC: coiled coil; LisH: Lis-homology (dimerization) motif. **(B)** Schematic representation of dynein and Lis1, color-coded as in (A) and throughout the paper. NT: N terminus; CT: C terminus.

appendages to the ring are essential for dynein function; the "stalk", an intramolecular coiled-coil at the end of which lies the microtubule-binding domain (Carter et al., 2008; Gee et al., 1997; Schmidt et al., 2012) and the "linker", which is dynein's key mechanical element and is an elongated structure N-terminal to AAA1. The linker spans the ring and moves in a nucleotide dependent manner that is thought to transmit force to dynein's cargo (Burgess et al., 2003; Huang et al., 2012; Kon et al., 2005; Roberts et al., 2012; 2009; Shima et al., 2006). In order for dynein to move along microtubules, ATP binding/hydrolysis at AAA1 must be coupled with linker motion and microtubule binding and release at the tip of the stalk, located 250 Å away (Gibbons et al., 2005; Huang et al., 2012; Imamula et al., 2007; Kon et al., 2005; 2009; Redwine et al., 2012).

Across a wide range of species, dynein interacts with a conserved regulator called Lis1 that is necessary for many dynein driven processes. Mutations in the Lis1 gene cause the neurodevelopmental disorder lissencephaly (Carter, 2013; Gibbons et al., 1987; Huang et al., 2012; Reiner et al., 1993; Vale, 2003). Lis1 is the only dynein regulator known to interact directly with its motor domain (Blocker et al., 1997; Driskell et al., 2007; Huang et al., 2012; Jordens et al., 2001; Kon et al., 2004; Kural et al., 2005; McKenney et al., 2010; Pilling et al., 2006). Like dynein, Lis1 acts as a dimer, with each monomer comprising an N-terminal dimerization domain followed by a coiled-coil, a flexible loop and a C-terminal β-propeller domain of 7 WD motifs (Cho et al., 2008; Heald et al., 1996; Kim et al., 2004; Kiyomitsu and Cheeseman, 2013; Merdes et al., 1996; Schmidt et al., 2012; Tarricone et al., 2004) (Fig. 3.1A,B). We previously showed that the propeller domain alone can regulate dynein *in vitro* and used negative stain electron microscopy (EM) and 2D image processing to show that Lis1 binds to dynein's motor domain near AAA3/4 (Egan et al., 2012; Huang et al., 2012; Lenz et al., 2006; Moughamian et al., 2013; Schmidt et al., 2012; Wilkie and Davis, 2001). We and others have shown that Lis1 induces a slow-moving, microtubule-attached state in dynein (Cho et al., 2008; Gibbons et al., 1991; Huang et al., 2012; Kon et al., 2004; 2012; McKenney et al., 2010; Schmidt et al., 2012; Torisawa et al., 2011; Yamada et al., 2008). Interestingly, Lis1 can accomplish this without substantially affecting dynein's overall ATP hydrolysis rate (Huang et al., 2012; Kon et al., 2012; Markus and Lee, 2011; McKenney et al., 2010; Schmidt et al., 2012; Yamada et al., 2008). This led us to propose that Lis1 acts

as a “clutch”, uncoupling dynein’s engine (AAA+ ring) from its track-binding region.

The previous 2D data indicating that Lis1 binds in the vicinity of AAA3/4 raised at least two possibilities for how Lis1 can affect dynein mechanochemistry. On the one hand, Lis1 may influence the structure or motions of AAA3 or AAA4 in the ring, in turn preventing the propagation of a signal for microtubule detachment to the stalk (“ring-centric regulation”). Alternatively, because the linker domain lies close to AAA4 in certain nucleotide-states, Lis1 may act by regulating the linker’s movement, and in turn dynein mechanochemistry (“linker-centric regulation”). Distinguishing between these modes of regulation is not possible without 3D data, as it is not known if Lis1 binds on the same face of the AAA+ ring as the linker, or if direct Lis1-linker interactions could occur. Moreover, it is not clear to what extent the Lis1 binding site encompasses AAA3, AAA4 or both these modules. Thus, 3D structural information is critical to advance our understanding of Lis1’s mechanism of action.

We set out to establish how Lis1 induces a persistent microtubule-bound state in dynein. Specifically, we wanted to distinguish between “ring-centric” and “linker-centric” modes of action. We obtained the 3D structure of *S. cerevisiae* dynein bound to Lis1 to determine which elements of the motor Lis1 directly affects. Our structure revealed that Lis1 sterically restricts the linker from making important interactions with the ATP hydrolyzing ring. Structure-based mutagenesis also allowed us to identify residues in Lis1 responsible for binding to dynein. Single molecule analysis of a dynein motor with a shortened linker that

can physically bypass Lis1 indicated that removing the steric block renders dynein insensitive to Lis1. Our combined data show that Lis1 directly blocks dynein's mechanochemical cycle, inducing a persistent microtubule-bound state, by acting on its linker domain.

Materials and Methods

Yeast Strain Construction

The *S. cerevisiae* strains used in this study are listed in Table A3.1. Deletions or modifications of endogenous genomic copies of the dynein heavy chain (*DYN1*) and Lis1 (*PAC1*) were done using PCR-based methods as previously described (Huang et al., 2012; Longtine et al., 1998), using the URA3/5FOA "pop-in/pop-out" method (Guthrie and Fink, 1991; Huang et al., 2012). Transformations were performed using the standard lithium acetate method (Gietz and Woods, 2002; Kon et al., 2012; Schmidt et al., 2012). Point mutants were generated using the PCR stitching method and verified by DNA sequencing.

Protein Expression and Purification

Cultures of *S. cerevisiae* for protein purification were grown, harvested, and frozen as described previously (Huang et al., 2012; Reck-Peterson et al., 2006). Dynein and Lis1 constructs were purified and labeled as described previously (Huang et al., 2012; Reck-Peterson et al., 2006; Tarricone et al., 2004), except that a modified TEV buffer for Lis1 purification was used; 50 mM Tris-HCl (pH

8.0), 150 mM potassium acetate, 2 mM magnesium acetate, 1 mM EGTA, 5% glycerol, 1 mM DTT and 1 mM PMSF.

EM Sample Preparation

4 µL of monomeric dynein (80-120 nM), or monomeric dynein pre-incubated for 10 min with Lis1 dimer at a 1.5-fold excess (120-180 nM), were applied to a glow discharged, continuous carbon coated, C-flat EM grids (Protochips). Dynein samples stated to be prepared in no nucleotide conditions were treated with apyrase (0.14 U/mL) for 15 min prior to grid application to hydrolyze residual ADP left over from the dynein purification procedure. Dynein samples stated to be prepared in ADP and ATP+Vi conditions contained 100 µM ADP and 500 µM Mg-ATP/$NaVO_4$ respectively. For the latter, nucleotide was added after the dynein-Lis1 pre-incubation step. Once applied to the grid, the samples were stained with 2% uranyl formate by floating the grid sample face down on a pool of stain. Samples were then sandwiched with a thin layer of freshly evaporated carbon, and grids were lightly blotted from the non-sample containing side and plunged into liquid nitrogen (De Carlo and Stark, 2010; Tarricone et al., 2004). Grids were then stored at liquid nitrogen temperatures.

EM Data Collection

Samples were imaged at liquid nitrogen temperatures using a Gatan 626 cryo holder on an Tecnai F20 TEM microscope (FEI), operating at 120 kV, equipped with a US4000 4k x 4k CCD camera (Gatan). Data was collected either manually

or automatically using Leginon (Carragher et al., 2000; Huang et al., 2012). Dynein alone samples (no nucleotide (strain RPY844) and ADP conditions (strain RPY844)) and dynein-Lis1 (ATP+Vi conditions (strains RPY1302 and RPY816)) were imaged at 62000X nominal magnification (1.73 Å/pixel). Dynein-Lis1 (no nucleotide (strains RPY1302 and RPY816)) was imaged at 50000X nominal magnification (2.14 Å/pixel). Short linker dynein-Lis1 (no nucleotide (strains RPY1436 and RPY816) was imaged at 80,000X nominal magnification (1.34 Å/pixel). Low-dose conditions during imaging (dose ~25 $e^{-}/Å^{2}$) were used for all datasets and micrographs were collected using a defocus range of -0.6 – -1.5 µm.

EM Image Pre-processing

For all datasets, ~1000 particles were initially selected manually in Boxer (EMAN1 (Huang et al., 2012; Ludtke et al., 1999)) and reference-free 2D classified in Imagic (Reck-Peterson et al., 2006; van Heel et al., 1996) to give class averages that were then used as templates for automated particle picking in Appion (Huang et al., 2012; Lander et al., 2009). Reference-free 2D classification in Imagic was subsequently used on the data sets to remove averages with blurred appearance or incorrect size. CTF determination and correction of image phases was carried out in Appion using Ace2 (NRAMM). Particles were band-pass filtered (high-pass = 250 Å, low-pass = 3 x sampling) in Imagic and normalized in Xmipp (Jaspersen and Winey, 2004; Sorzano et al., 2004). For 3D classification and initial 3D refinement particles were binned by 2;

final 3D refinements were carried out using unbinned data.

EM Image Processing

Dynein (no nucleotide)

An initial model was generated using the *S. cerevisiae* dynein motor domain crystal structure (PDB ID: 4AKG (Lee et al., 2003; Schmidt et al., 2012; Sheeman et al., 2003)) low-pass Fourier filtered to 80 Å. Initial 3D refinement was carried out in EMAN2 (Moore et al., 2009; Tang et al., 2007). The resulting map was filtered to 40 Å and used as an initial model for 3D classification in RELION. Five classes were generated. Particles from 4 of the classes were combined and refined in RELION against the class 5 map, filtered to 40 Å. 3D refinement converged after 18 iterations. The final map contained 31,839 particles (from 38,463 total) and the "gold-standard" resolution using an FSC cutoff of 0.143 was 14.8 Å. The final map was filtered according to local resolutions (Cardone et al., 2013; Yeh et al., 1995).

Dynein (ADP)

The linker domain has been shown to have a different position relative to the dynein ring in ADP conditions in *D. discoideum* dynein compared with that of *S. cerevisiae* dynein in no-nucleotide conditions (Kon et al., 2005; 2012; Roberts et al., 2009; 2012; Schmidt et al., 2012). To avoid initial model bias of linker position the domain was computationally removed from residue 1620 of PDB file 4AKG (Kon et al., 2012; Schmidt et al., 2012). The resulting map was filtered to 40 Å and used as an initial model for 3D classification in RELION. Five classes were

generated. Four of the classes showed the linker at the no-nucleotide position and 1 class at the shifted position seen with *D. discoideum* dynein in ADP conditions. The particles in this class were refined against the class map in RELION and the refinement converged after 10 iterations. The final map contained 3,983 particles (from 17,256 total) and the “gold-standard” resolution using an FSC cutoff of 0.143 was 19.5 Å. The final map was filtered according to local resolutions (Cardone et al., 2013; Schmidt et al., 2012).

Dynein-Lis1 (no nucleotide)

The same initial model as described for dynein (no nucleotide) above was used to 3D refine an initial dataset of dynein-Lis1 (RPY844, RPY816) in EMAN2. This map was then filtered to 60 Å and EMAN2 used to refine a larger dataset of dynein-Lis1 using a dynein lacking any tags on the end of the linker (RPY1302). The resulting map was filtered to 40 Å and used for 3D classification in RELION. This process was repeated with different requested class numbers. Linker position was observed to vary across classes (Fig. A2.1F–H). In a run with 5 generated classes, classes with most density for the linker (class 1 and 5) were combined and refined against the class 1 map filtered to 40 Å in RELION. Three-dimensional refinement converged after 16 iterations. The final map contained 10,129 particles (from 35,472 total) and the “gold-standard” resolution using an FSC cutoff of 0.143 was 21.4 Å. The final map was filtered according to local resolutions (Cardone et al., 2013; Kon et al., 2005).

Short linker dynein-Lis1 (no nucleotide)

The same initial model as described for dynein (no nucleotide) was used for

initial 3D classification of the dataset in RELION. Five classes were generated. Particles from 1 class were further refined against the class map in RELION. The refinement converged after 14 iteractions and contained 11,818 particles (from 34,805 total). The gold-standard resolution using an FSC cut-off of 0.143 was 17.3 Å. The final map was filtered according to local resolutions (Cardone et al., 2013; Yin et al., 2005).

Dynein-Lis1 (ATP+Vi)

The map of dynein-Lis1 (no nucleotide) filtered to 60 Å was used as a starting model for initial refinement in EMAN2. The resulting map was filtered to 40 Å and used for 3D classification in RELION. Most classes showed the linker position unresolved, indicative of variability in location as previously observed (Burgess et al., 2003; Huang et al., 2012; McKenney et al., 2010; Roberts et al., 2012; Yamada et al., 2008), but one class resolved the linker near AAA2 when viewed at lower contour levels. The particles in this class were refined against the class map in RELION and refinement converged after 9 iterations. The final map contained 2,120 particles (from 6,600 total) and the "gold-standard" resolution using an FSC cutoff of 0.143 was 23.1 Å.

Size Exclusion Chromatography

Dynein and Lis1 were tested for complex formation and Lis1 mutants were tested for structural integrity (Fig. A2.2C) by size-exclusion chromatography. Four hundred to 800 nM dynein and 475–800 nM Lis1 were loaded separately or after being mixed for 10 min at 4ºC. Samples were fractionated on a Superose 6 PC

3.2/30 column using an ÄKTAmicro system (GE Healthcare) that had been equilibrated with degassed gel filtration buffer (50 mM Tris-HCl pH 8.0, 150 mM potassium acetate, 2 mM magnesium acetate, 1 mM EGTA, 1 mM DTT). Fractions (50 µL or 90 µL) were analyzed by SDS-PAGE on 4%–12% Tris-Bis gels (Invitrogen) with SYPRO Red staining (Invitrogen), and imaged using an ImageQuant 300 (BioRad) or Typhoon (Amersham) gel imaging system.

Single-Molecule Microscopy

Single-molecule motility assays were performed using flow chambers as previously described (Case et al., 1997). Dynein was labeled with TMR (Promega), and microtubules contained ~10% biotin-tubulin for surface attachment and ~10% HyLite488-tubulin (Cytoskeleton) for visualization. For assays that included Lis1, dynein was incubated with 200 nM Lis1 for 10 min at 4 ºC prior to addition to the flow chamber. The imaging buffer consisted of 30 mM HEPES (pH 7.2), 50 mM potassium acetate, 2 mM magnesium acetate, 1 mM EGTA, 10% glycerol, 1 mM DTT, 20 mM taxol, 1.25 mg/mL casein, 1 mM Mg-ATP, and an oxygen scavenger system. Images were recorded every 2 s for 5 min, and dynein velocities and run-lengths were calculated from kymographs generated in ImageJ (National Institutes of Health).

In vitro motility assays were visualized on either a Zeiss Elyra PS.1 microscope with a 100x 1.46 N.A. oil immersion TIRF objective (Zeiss) with an Andor EM-CCD camera or an Olympus IX-81 TIRF microscope with a 100X 1.45 N.A. oil immersion TIRF objective (Olympus) with a Hamamatsu EM-CCD

camera. TMR-labeled dynein and HyLite488-microtubules were excited with 561 nm and 488 nm solid state laser lines, respectively. Images were recorded with a 100 ms exposure using Zen Black (Zeiss) or Metamorph software. Microtubule gliding assays and microtubule binding and release assays were performed as described (Huang et al., 2012). Control experiments for the microtubule release assays examined dynein release in buffer lacking ATP (Fig. A2.5E), where dynein remained bound to microtubules as expected (Huang et al., 2012) and with dynein lacking N-terminal tags (Fig. A2.5F,G), where untagged dynein behaved similarly to tagged dynein (Fig. 3.5E,F).

Spindle oscillation assay

To track the dynein-dependent movement of spindle pole bodies (SPBs), we used a strain containing a GFP labeled SPB marker, *SPC110*, and a tdTomato labeled cell membrane marker, *HXT1* (kindly provided by Jeff Moore, University of Colorado). Mutations were introduced into the *PAC1 (*Lis1) locus in this strain. For control experiments, strains containing deletions of the dynein heavy chain (*DYN1*) and *PAC1* loci were constructed. All strains were PCR verified and mutations were additionally verified by DNA sequencing.

For image analysis, saturated overnight cultures for each strain were diluted to an OD_{600} of 0.1 in a total volume of 5 mL YPD media. The dilution of cultures was staggered such that data could be collected for all strains during a single imaging session. Following dilution, each culture was incubated with rotation at 30 °C for 3 hours. Hydroxyurea (HU) was then added to a final

concentration of 200 mM, and the culture was incubated for an additional 2 hours with rotation at 30 °C. The cells were collected by centrifugation, the media was discarded, and the cells were resuspended in 250 µL of fresh YPD + 200 mM HU. The cells were loaded into a Y04C microfluidic yeast plate (CellASIC) and introduced into the viewing chamber with the ONIX controller (CellASIC). Imaging was performed at the Nikon Imaging Center at Harvard Medical School. All images were collected with a Yokagawa CSU-X1 spinning disk confocal with Borealis modification, on a Nikon Ti inverted microscope equipped with a Plan 60x 1.4 N.A. objective and the Perfect Focus System. GFP-labeled SPB and tdTomato-labeled cell membrane fluorescence was excited with the 488 nm and 561 nm lines, respectively, from a LMM-5 solid state laser merge module controlled with an ATOF (Spectral Applied Research). Images were acquired with a Hamamatsu ORCA-AG CCD controlled with MetaMorph 7.0 software. Images were collected for SPBs as 100 ms exposures spanning 9 x 500 nm Z-sections (4.5 µm total Z stack) every 30 seconds for a total duration of 20 minutes. Cell membranes were imaged as single central Z-sections at the first and last time point. Membrane image pairs were digitally merged to allow for drift analysis; those cells with visible drift were excluded from analysis.

Image processing and particle tracking

Maximum intensity projections were calculated for Z-series at each time point for GFP-labeled SPBs. At each time point, SPBs were independently detected in the Z-projection using a wavelet detection algorithm (Aguet et al., 2013), and the two

spindles were tracked throughout the course of the movie using a nearest neighbor tracking method (unpublished Matlab (Mathworks) scripts). The location of the bud neck and the mother-daughter orientation were determined using the first tdTomato-labeled cell membrane exposure. The locations of tracked SPBs were used to calculate the number of budneck crossings.

FRET

To generate the dynein FRET construct, eGFP (the FRET donor) was inserted at the dynein N-terminus and the acceptor site was inserted after L2241 in AAA2. We used the ybbR tag (GGGTVL**DSLEFIASKLA**GGG (Yin et al., 2005) labeled with TMR-CoA (NEB) as the FRET acceptor. Dynein was incubated with or without Lis1 for one hour on ice, followed by apyrase (6.6 U/mL) or 200 μM ATP.Vi for 2 min at room temperature (RT). For some experiments, dynein was first incubated with 200 μM ATP.Vi for 2 min at RT, followed by Lis1 for 1 hour on ice. Assays were performed in 30 mM HEPES (pH 7.2), 50 mM potassium acetate, 2 mM magnesium acetate, 1 mM EGTA, 1mM DTT and the final concentrations of dynein and Lis1 were 84 nM and 840 nM, respectively. The sample was excited with 485 nm (eGFP) light and the emitted light was detected from 505 nm to 650 nm in a SpectraMax M5 fluorimeter (Molecular Devices) at RT. In order to normalize across experiments, the samples were also excited with 535 nm (TMR) light and the emitted light was detected from 555 nm to 700 nm. To analyze the FRET data, we first subtracted the fluorescence background from the buffer alone. We then used the emission spectra of dynein labeled with

eGFP and free TMR dye alone to decompose each channel in the experimental spectra. FRET efficiencies (E) were calculated using the method of Clegg(Clegg, 1995): $E = \{F^a_{FRET} / F^a_{DIR} - \varepsilon^a(485) / \varepsilon^a(535)\}\varepsilon^a(535) / \varepsilon^d(485)$, where the superscripts “d” and “a” refer to the donor (eGFP) and the acceptor (TMR), respectively. F^a_{FRET} is the fluorescence intensity of the acceptor excited at 485 nm and F^a_{DIR} is the fluorescence intensity of the acceptor excited at 535 nm. $\varepsilon^d(485)$ $\varepsilon^a(485)$ and $\varepsilon^a(535)$ are the molar extinction coefficients at the designated wavelengths. In our experiments $\varepsilon^a(535) / \varepsilon^d(485) = 37{,}900\ M^{-1}\ cm^{-1} / 40{,}000\ M^{-1}\ cm^{-1}$ and $\varepsilon^a(485) / \varepsilon^a(535) = 0.2$.

ATPase Assays

Dynein constructs used in ATPase assays were tested for complex formation with Lis1 by size-exclusion chromatography (Fig. A2.4). ATPase assays were performed using an EnzChek phosphatase kit (Molecular Probes) as previously described(Cho et al., 2008; Reck-Peterson et al., 2006). The final reaction consisted of 10-20 nM dynein (monomeric constructs, see Fig. 3.4), 0 or 140 nM Lis1, 0-7.5 μM taxol-stabilized microtubules, 2 mM Mg-ATP, 200 mM MESG (2-amino-6-mercapto-7-methyl-purine riboside), 1 U/mL purine nucleoside phosphorylase, and assay buffer (30 mM HEPES (pH 7.2), 50 mM potassium acetate, 2 mM magnesium acetate, 1 mM EGTA, 1 mM DTT, and 10 mM taxol). A SpectraMax384 plate reader (Molecular Devices) was used to monitor the coupled reaction at OD360 every 12 s for 10 min. Data were fit according to (Nishiura, 2004)

Results

Structure of the dynein-Lis1 complex

In order to visualize the spatial relationship between Lis1 and dynein's multiple structural elements and to better understand the mechanism by which Lis1 regulates dynein we used cryo-negative stain (cryo-NS) EM and single-particle image processing to obtain the 3D structure of the dynein-Lis1 complex (Fig. 3.3A). Cryo-NS combines the structural preservation of vitrification with the high contrast provided by the negative stain (Carter et al., 2008; De Carlo and Stark, 2010; Gee et al., 1997; McKenney et al., 2010; Schmidt et al., 2012). We also determined a 3D map of dynein alone, as a reference, to establish whether Lis1 alters dynein's structure (Fig. 3.3B). We used a well-characterized monomeric dynein construct (Burgess et al., 2003; Huang et al., 2012; Kon et al., 2005; Longtine et al., 1998; Roberts et al., 2009; 2012; Shima et al., 2006) but chose to use dimeric rather than monomeric Lis1 for our reconstructions. This takes advantage of the increased avidity of the Lis1 dimer; we previously showed that while a Lis1 monomer is sufficient to slow down dynein, a much higher concentration of it is required (Gibbons et al., 2005; Guthrie and Fink, 1991; Huang et al., 2012; Imamula et al., 2007; Kon et al., 2005; 2009; Redwine et al., 2012).

Both dynein and Lis1 were expressed from *S. cerevisiae* at their genomic loci (Table A3.1). We imaged dynein-Lis1 and dynein alone in the absence of nucleotide and obtained structures at resolutions of 21 Å for the

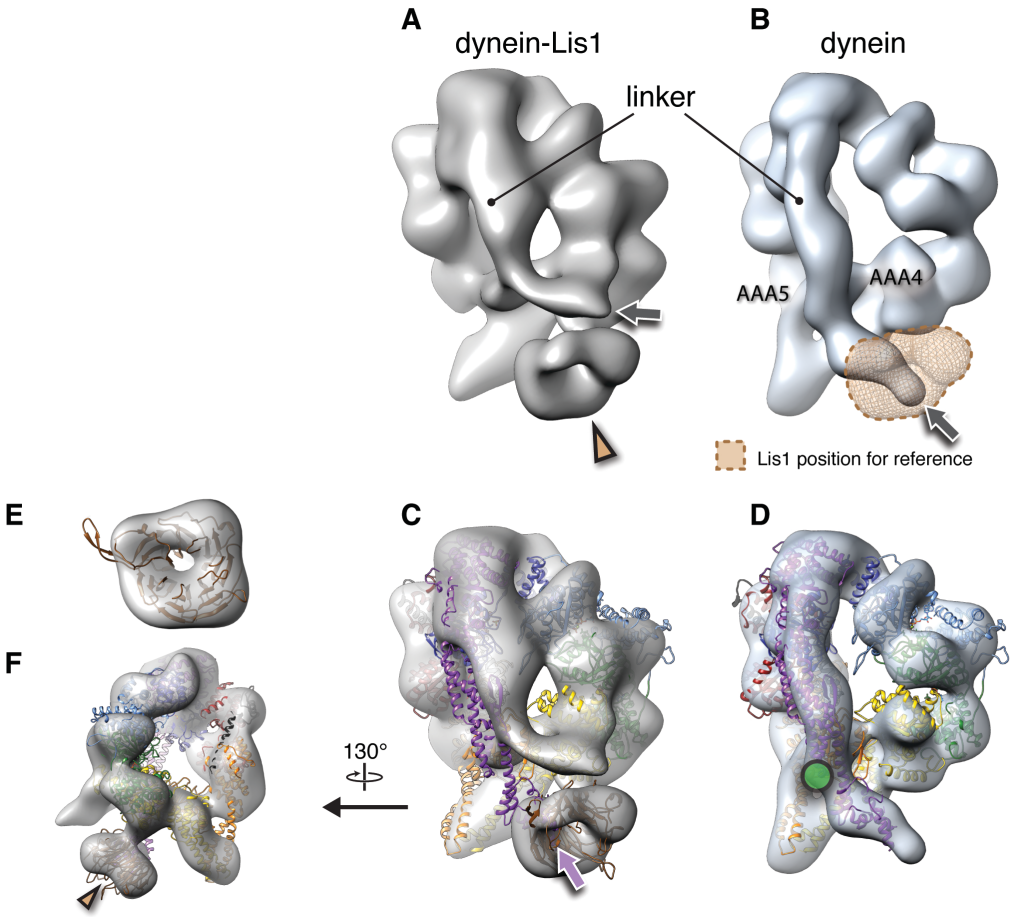

Figure 3.2 The binding of Lis1 to dynein changes the position of dynein's linker domain

(A) Cryo-NS EM reconstruction of the dynein motor domain in complex with Lis1 and **(B)** of the motor domain alone. AAA4 and AAA5 are labeled. A density present only in the dynein-Lis1 map is highlighted in (A) (brown arrowhead). The linker occupies different positions in the two maps (compare labeled densities and grey arrows) and its position in the dynein alone map is sterically incompatible with Lis1, as indicated by a semi-transparent Lis1 density. **(C)** Structural model of dynein's motor domain docked into the EM maps of dynein-Lis1 and **(D)** dynein alone. The model was built from crystal structures of the *S. cerevisiae* dynein ring (PDB ID: 4AKG (Schmidt et al., 2012) and *D. discoideum* linker aligned to the yeast linker position (PDB ID: 3VKG (Kon et al., 2012)), the *D.discoideum* linker being closer in length to that in our EM construct. In (C) a homology model of the *S. cerevisiae* Lis1 β-propeller (brown) has been docked into the new density highlighted in (A). The linker domain in the EM map (grey arrow) is shifted away from its position in the crystal structure (purple arrow), which protrudes from the EM density and clashes with the Lis1 density. In contrast, the linker is within the EM density in the dynein alone map (D). Green circle: location of known interactions between the linker and AAA5 module in dynein (Schmidt et al., 2012). **(E)** Close-up view of the Lis1 density with docked in homology model viewed along the axis indicated by the arrowhead in (A). **(F)** A rotated, smaller view of (C), showing the interface between Lis1 (brown arrowhead) and dynein.

complex (Fig. 3.1A,C, Fig. A2.1C) and of 15 Å for dynein alone (Fig. 3.1B,D, Fig. A2.1C). The dynein alone map accommodates the crystal structure of the dynein motor domain well (Gietz and Woods, 2002; Kon et al., 2012; Schmidt et al., 2012) (Fig. 3.1D).

The dynein-Lis1 map shows two major differences relative to the dynein alone reconstruction. First, a prominent, donut-shaped density is resolved in contact with the dynein ring, adjacent to the stalk (Fig. 3.1A, orange arrowhead). This extra density matches the dimensions of a β-propeller, including the hole at its center (Fig. 3.1C,E,F). We thus conclude that the density corresponds to Lis1. The 3D structure also allowed us to hone in on the region of dynein interacting with Lis1 compared to our previous 2D analysis (Huang et al., 2012; Reck-Peterson et al., 2006). The second, and striking difference between the two maps is in dynein itself: Lis1 binds on the same face of the ring where dynein's linker domain is located and the linker is displaced by ~44 Å in the dynein-Lis1 map relative to the dynein alone reconstruction (Fig. 3.1A-D).

One dynein ring binds one Lis1 β-propeller

The extra density in our dynein-Lis1 map fits well a homology model of the *S. cerevisiae* Lis1 (known as Pac1 in yeast) β-propeller built from the crystal structure of the mouse protein (Huang et al., 2012; Reck-Peterson et al., 2006; Tarricone et al., 2004) (Fig. 3.1C,E,F). Because our map resolved the hole at the center of the propeller, the Lis1 model could be unambiguously docked within the density in terms of its translation (Fig. 3.1E). In Lis1, the β-propeller is connected to the N-terminal LisH dimerization domain by a predicted flexible loop and a

coiled coil (De Carlo and Stark, 2010; Tarricone et al., 2004). Consequently, the rest of Lis1 is expected to adopt a wide range of positions relative to the dynein-bound propeller domain. In agreement with this, we did not resolve density beyond that of the propeller in our map and the Lis1 density seen in our reconstruction of the complex corresponded to a single β-propeller. Two-dimensional image analysis of dynein-Lis1 complexes with monomeric or dimeric Lis1 showed the same density and location for Lis1 (Fig. A2.1D,E), indicating a stoichiometry of one Lis1 propeller to one dynein motor domain.

Dissection of the dynein-Lis1 interface

Our structure of the dynein-Lis1 complex shows that the Lis1 β-propeller contacts dynein primarily at a surface-exposed helix at the junction of AAA3 and AAA4 (Fig. 3.3A), explaining why mutagenesis of four conserved, charged residues (KDEE) on this helix virtually abolished Lis1 binding and dynein regulation(Carragher et al., 2000; Huang et al., 2012). The resolution of the reconstruction does not allow us to determine unambiguously the rotational orientation of the Lis1 homology model within the corresponding density. We therefore used mutagenesis to probe the dynein-Lis1 interface and further constrain our model of the complex.

Within Lis1, sequence conservation is much greater on one face of the β-propeller (“top”) compared to the other (Fig. A2.2A), suggesting that this top face may interact with dynein. Consistent with this idea, the docked β-propeller showed a better qualitative fit and a slightly higher cross-correlation coefficient

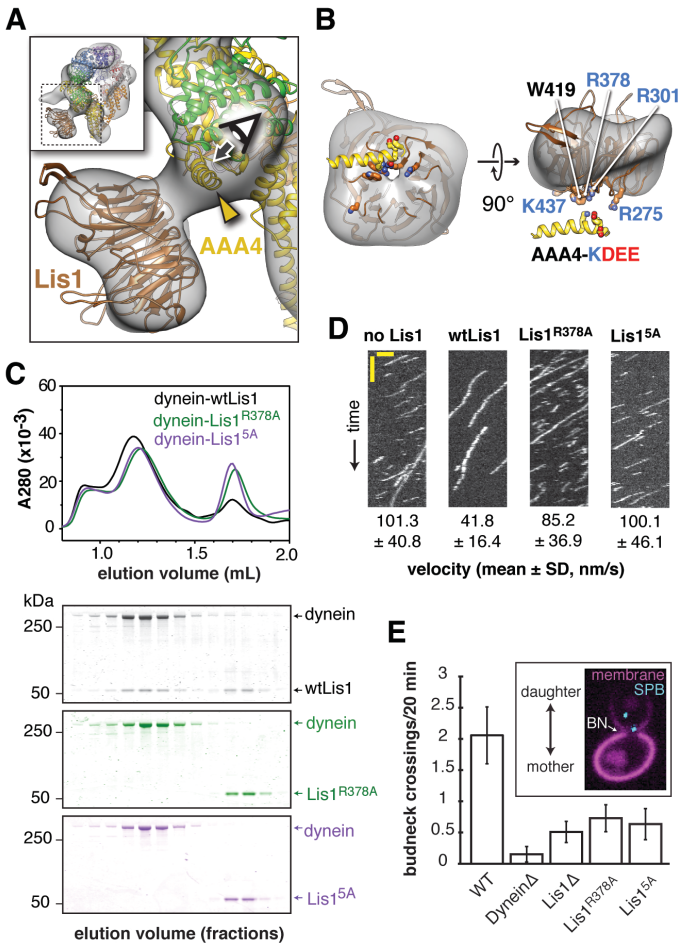

Figure 3.3 Disrupting the putative dynein-Lis1 interface impairs Lis1's ability to bind to and regulate dynein

(A) The Lis1 β-propeller engages dynein primarily at a surface helix connecting AAA3 and AAA4 (yellow arrowhead). Inset: a zoomed out view. **(B)** (Left) View along the axis highlighted in (A) by the eye/arrow; (right) rotated view. Except for the helix (yellow), the dynein density was removed for clarity. Five conserved residues on Lis1 that were mutated to alanine, either in combination (Lis1^{5A}) or individually, are labeled and shown in atomic representation. Also displayed are residues (KDEE) in dynein known to be involved in the interaction with Lis1 (Huang et al., 2012). Basic and acidic residues are labeled in blue and red, respectively. **(C)** Lis1^{R378A} and Lis1^{5A} mutants abolish dynein-Lis1 complex formation as measured by size-exclusion chromatography. Traces show elution profiles of GST-dynein$_{331kDa}$ ('dynein') with wild type Lis1 (black), Lis1^{R378A} (green) and Lis1^{5A} (purple). SDS-PAGE for collected fractions are shown below. **(D)** Kymographs of *in vitro* motility experiments with TMR labeled GST-dynein$_{331kDa}$ alone or in the presence of 200 nM wild type or mutant Lis1. Horizontal scale bar = 2 μm, vertical = 20 s. **(E)** *In vivo* spindle oscillation assays comparing *S. cerevisiae* strains carrying either wild type or mutant Lis1 or full deletions of dynein or Lis1. Inset is a Z-projection of a dividing cell with markers for the membrane (purple) and spindle pole bodies (SPBs) (cyan). BN = bud neck. Bud neck crossing by the SPBs were counted over 20 minutes. WT N = 53, DyneinΔ N = 32, Lis1Δ N = 55, Lis1^{R378A} N = 58, Lis1^{5A} N = 47. For each strain the mean and SE are shown.

with our density map when the top face is placed at the dynein interface (Fig. A2.2B). To test this docking orientation, we mutated highly conserved residues on the top face of the propeller (Fig. 3.3B). Our previous finding that the KDEE residues in dynein are critical for Lis1 binding (Huang et al., 2012; Ludtke et al., 1999) suggested that interactions between Lis1 and dynein have an electrostatic component. We therefore targeted four positively charged residues on the top propeller face, as well as a surface tryptophan, all of which are conserved (Fig. 3.3B). We mutated these residues to alanine, both singly and in combination.

Using size exclusion chromatography, we tested the ability of the Lis1 mutants to interact with a functional, dimerized dynein construct (GST-dynein$_{331kDa}$) (Reck-Peterson et al., 2006; van Heel et al., 1996). When all five residues are mutated to alanine (Lis1^{5A}), dynein binding is abolished (Fig. 3.3C and Table A3.2). Binding is severely weakened with two of the single point mutants, Lis1^{R378A} and Lis1^{W419A} (Fig. 3.3C and Fig. A2.2D). The remaining single point mutants showed varying degrees of compromised binding to dynein (Table A3.2 and Fig. A2.2D). Thus, we conclude that highly conserved amino acids on the top face of Lis1's β-propeller are critical for dynein binding, in support of our structural model for the dynein-Lis1 complex (Fig. 3.3A).

We next examined if the binding-deficient Lis1 mutants Lis1^{R378A} and Lis1^{5A} were able to regulate dynein *in vitro.* Wild type Lis1 decreases dynein velocity *in vitro* in a concentration-dependent manner (Huang et al., 2012; Lander et al., 2009). In these assays, the motion of single, fluorescently labeled dynein molecules along microtubules is monitored over time. The Lis1^{R378A} mutant

showed only a slight reduction in dynein velocity compared to dynein alone, suggesting that this mutant is limited in its ability to bind and regulate the motor (Fig. 3.3D). The Lis1^{5A} mutant showed no reduction in dynein velocity, consistent with its inability to bind dynein (Fig. 3.3D). Thus, the impact of the Lis1 mutations on dynein binding is correlated with the ability of the Lis1 mutants to regulate dynein at the single-molecule level.

Lastly, we tested our model for the dynein-Lis1 complex by measuring the effect of disrupting the dynein-Lis1 interface *in vivo*. In yeast, spindle pole bodies (SPB) span the nuclear envelope and coordinate microtubule minus ends that emanate from its nuclear and cytoplasmic faces (Jaspersen and Winey, 2004; Sorzano et al., 2004). Lis1 assists in concentrating dynein at the plus ends of cytoplasmic microtubules, from where dynein is offloaded to the cell cortex (Lee et al., 2003; Schmidt et al., 2012; Sheeman et al., 2003). Cortically anchored dynein exerts a pulling force that results in displacements of the entire mitotic spindle (Moore et al., 2009; Tang et al., 2007), giving rise to a brief series of oscillations across the budneck. Deletion of dynein eliminates these oscillations (Yeh et al., 1995). We quantified the effect of the Lis1^{5A} and Lis1^{R378A} mutants on spindle movement in cells treated with hydroxyurea, which prolongs the period of oscillations, by tracking fluorescently labeled SPBs over the course of 20 minutes. We found that disruption of the dynein-Lis1 interface resulted in a decrease in the number of budneck crossings to a level similar to that caused by deletion of Lis1 (Fig. 3.3E). These results indicate that the dynein-Lis1 interface identified in our structural model is crucial for dynein's biological function.

Lis1 sterically blocks the position adopted by the linker under ADP and no nucleotide conditions but does not prevent it from reaching the pre-powerstroke position at AAA2

The end of the linker domain is displaced ~44 Å in the dynein-Lis1 structure relative to the dynein alone map, mainly along the plane of the ring (Fig. 3.2A,B). The structure suggests that this displacement may be a direct result of Lis1's binding to dynein: the linker position in the dynein alone structure is sterically incompatible with the presence of Lis1 (Fig. 3.2B). This provides a first piece of evidence that Lis1 may regulate dynein motility through a linker-centric mechanism, by sterically blocking the linker's normal position in the no nucleotide state.

We next sought to test if Lis1 sterically blocks the linker in other nucleotide states. As the main mechanical element of dynein, the linker is thought to adopt at least two additional conformations during the ATPase cycle. In the presence of ATP (or ATP and V_i; a phosphate analog), the linker is displaced across the ring to near AAA2 (Kon et al., 2005; 2012; Roberts et al., 2009; 2012; Schmidt et al., 2012) (pre-powerstroke position). In the presence of ADP the linker lies over AAA4 in the crystal structure of the *D. discoideum* dynein(Kon et al., 2012; Schmidt et al., 2012). This post-powerstroke position is slightly different to that seen in the *S. cerevisiae* dynein crystal structure in the absence of nucleotide, in which the linker is docked onto AAA5 (Schmidt et al., 2012). However, because the same dynein isoform has not been visualized in both the no nucleotide and

ADP states, it is uncertain if the AAA4 and AAA5 linker positions correspond to distinct mechanochemical states or are due to differences between dynein species.

To address this, we first obtained the structure of *S. cerevisiae* dynein alone in the presence of ADP. Conformational sorting revealed that the linker adopts two positions in this condition (Fig. 3.4A). One is the AAA5-docked position seen in *S. cerevisiae* dynein with no nucleotide. The other is over AAA4, coinciding with that observed in the *D. discoideum* crystal structure. The AAA4 position was seen only in the presence of ADP, and was not detectable in no nucleotide conditions. These results suggest that the linker docks at AAA5 in the absence of nucleotide but can coexist in the AAA4- and AAA5-interacting states in the presence of ADP. Importantly, both the AAA4 linker position in the ADP state and the AAA5 position in the no nucleotide state are sterically incompatible with the presence of Lis1 (Fig. 3.4B). Thus, we conclude that binding of Lis1 to the dynein ring results in a displaced linker, away from its normal docking sites under both no nucleotide (AAA5) or ADP (AAA4) conditions.

We then used two approaches to determine if Lis1 influences the position of the linker at its pre-powerstroke position, near AAA2. First, we designed a monomeric fluorescence resonance energy transfer (FRET) construct to measure linker movement to AAA2 in *S. cerevisiae* dynein, based on a linker sensor developed for *D. discoideum* dynein (Kon et al., 2005). In our construct, we fused an eGFP donor to the N-terminus of the linker and coupled a tetramethylrhodamine (TMR) acceptor to AAA2 via a small acetyl-CoA-binding

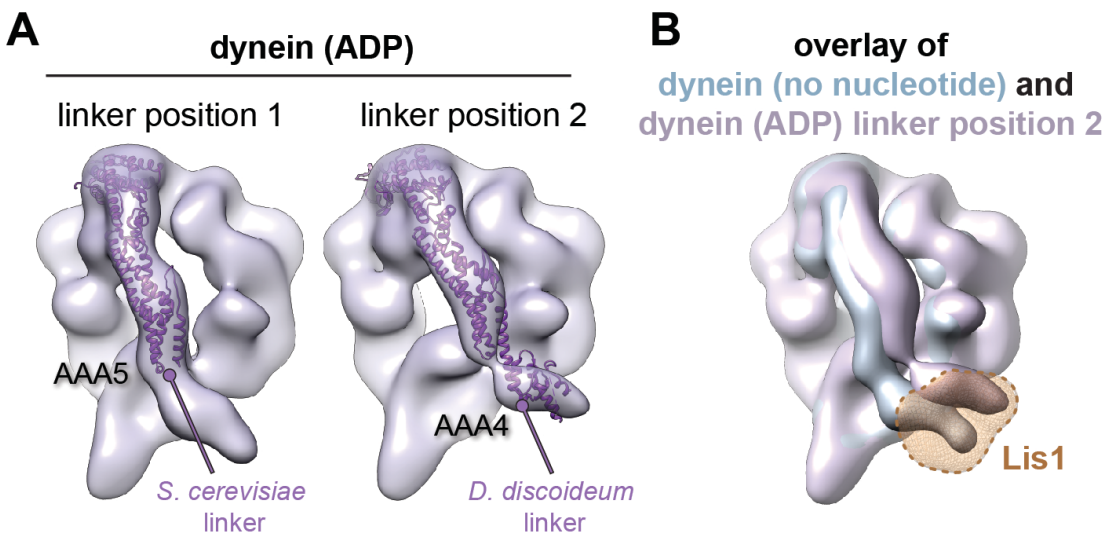

Figure 3.4 Dynein's linker positions in ADP and no nucleotide conditions, both of which are sterically incompatible in the presence of Lis1
(A) Cryo-NS maps of *S. cerevisiae* dynein in 100 μM ADP displaying the linker next to either AAA5 (left) or AAA4 (right). The *S. cerevisiae* linker domain (lacking nucleotide at AAA1, PDB ID: 4AKG (Schmidt et al., 2012) and the *D. discoideum* linker domain (with ADP at AAA1, PDB ID: 3VKG (Kon et al., 2012) are displayed in purple ribbon representation and have been docked into the linker-AAA5 and linker-AAA4 maps, respectively. To enable unambiguous comparison of linker positions between the EM density and crystal structure, we aligned each EM map to the corresponding dynein motor domain crystal structure after computationally removing the linker. **(B)** The dynein maps in no nucleotide (blue) and ADP (purple) conditions (the latter with the linker at the AAA4 location) are overlaid to compare linker positions. The location of Lis1 in the dynein–Lis1 map is shown as a transparent brown density. Both linker positions are sterically incompatible with the presence of Lis1. Note: since the ADP AAA5 linker position is the same as that seen under no nucleotide conditions, we only show the ADP map with the linker at AAA4.

tag (ybbR (Yin et al., 2005)) (Fig. 3.5A). This dynein construct (GFP-dynein$_{FRET/A2}$) slides microtubules robustly, with gliding rates ~90% of wild type dynein (GFP-dynein$_{331kDa}$) (Fig. A2.3A,B), showing that the tags are compatible with motor function. Under nucleotide-free conditions, and in the absence of Lis1, this construct showed a low FRET efficiency (~2%), as expected when the linker is docked at AAA5 (post-powerstroke position) and the FRET donor and acceptor are far apart (Fig. 3.5B). In the presence of ATP and vanadate (V_i), which trap

dynein in a dead-end ADP.V_i complex, FRET increased to ~26% (Fig. 3.5B). Under these conditions the linker is biased towards the pre-powerstroke position at AAA2 and the fluorophores lie closer together. When ADP.V_i-dynein was treated with Lis1, there was no significant change in the FRET efficiency relative to ADP.V_i-dynein alone (Fig. 3.5B). When dynein was incubated with Lis1 before adding ATP and V_i, the FRET efficiency was also close to that observed for ADP.V_i-dynein alone, albeit statistically significantly lower (Fig. 3.5B). The results suggest that Lis1 has little or no effect on the linker position once it is displaced toward AAA2 (ATP+V_i added before Lis1), and a minor effect on molecules undergoing the AAA5 to AAA2 transition (Lis1 added before ATP+V_i).

As a second method to determine if Lis1 affects the linker position of ADP.V_i dynein, we determined the EM structure of the ADP.V_i dynein-Lis1 complex. We could resolve the linker in the expected position displaced towards AAA2 and the density for the Lis1 ß-propeller at the AAA3/4 junction (Fig. 3.5C,D). In summary, these results indicate that the presence of Lis1 does not sterically interfere with the linker when it is in its pre-powerstroke position at AAA2. In contrast, Lis1 occludes the linker at both of its post-powerstroke positions at AAA4 and AAA5.

ATP turnover in the presence of Lis1 requires a hydrolysis-competent AAA1 and a functional AAA5 linker-docking site

We and others have shown that Lis1 does not significantly affect dynein's overall ATPase rate (Burgess et al., 2003; Huang et al., 2012; McKenney et al.,

2010; Roberts et al., 2012; Yamada et al., 2008). However, which of dynein's

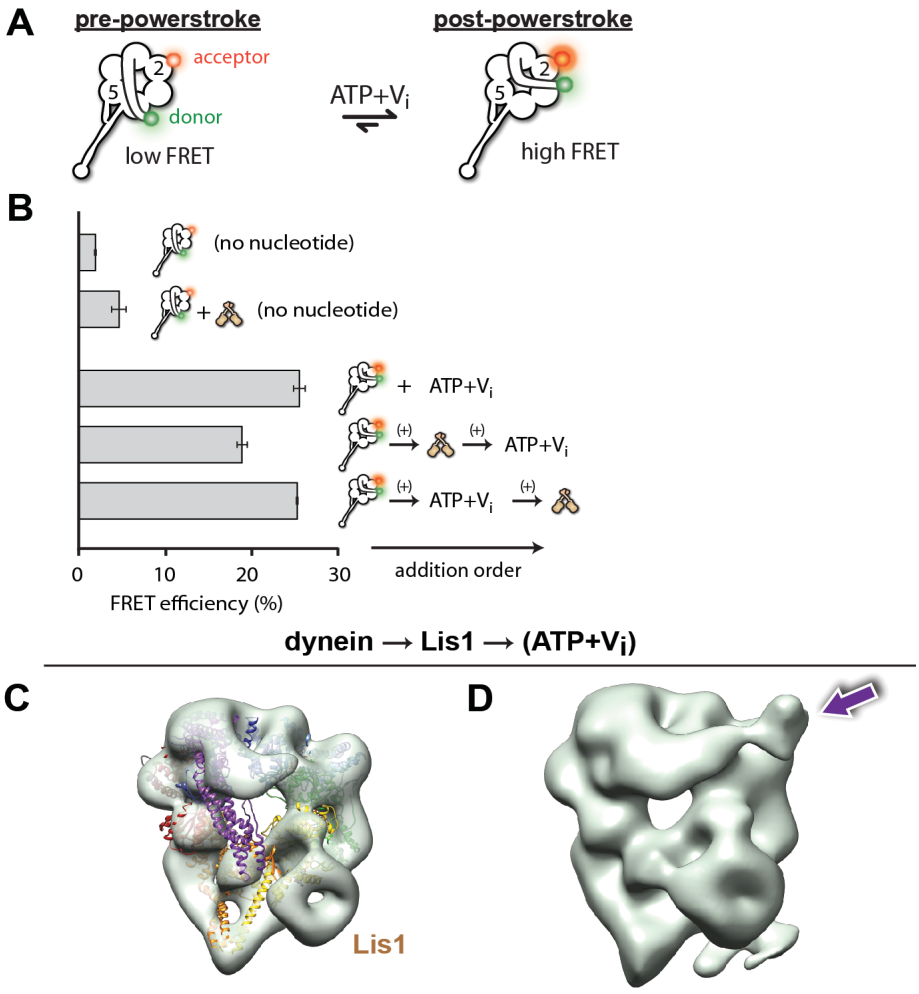

Figure 3.5 Lis1 does not prevent it from reaching the pre-powerstroke position at AAA2

(A) Schematic representation of the dynein FRET construct used to test linker dynein's swing in the presence of Lis1. eGFP (green sphere - donor) was fused to the N-terminus of the linker domain and TMR (red sphere - acceptor) was inserted into the AAA2 domain in the ring. Pre-powerstroke linker positions, where the linker moves close to AAA2 in ATP and vanadate (V_i) conditions, would display an increased FRET efficiency between the two fluorophores (bottom) relative to the no nucleotide state, when the linker is docked at AAA5 (top). **(B)** FRET efficiency between the eGFP and TMR fuorophores in the absence or presence of 200 μM ATP + Vi and 840 nM Lis1, ***$p < 0.001$. The order of addition for the reactions containing ATP + Vi and Lis1 is indicated by arrows. Averages of three experiments ± SD are shown. **(C)** Cryo-NS reconstruction of dynein-Lis1 in ATP+V_i conditions with the crystal structure of the motor domain docked in (Schmidt et al., 2012). The Lis1 density is indicated. **(D)** At lower contour levels, the N-terminal portion of the linker can be resolved (purple arrow).

AAA+ domains is responsible for this ATPase activity was not previously addressed. To determine this we measured microtubule-stimulated ATPase rates, with and without Lis1, in different monomeric dynein constructs.

As expected, dynein monomers continued to hydrolyze ATP in the presence of Lis1 at levels similar to those of dynein alone (Fig. 3.6A). Next, we measured ATPase activity in a dynein construct where AAA1, the main site of ATP hydrolysis in dynein (Carter, 2013; Gibbons et al., 1987; Vale, 2003) was rendered hydrolysis-deficient with an E to Q mutation in its Walker B motif (Blocker et al., 1997; Driskell et al., 2007; Jordens et al., 2001; Kon et al., 2004; Kural et al., 2005; Pilling et al., 2006). ATP hydrolysis was virtually abolished in this construct, both in the presence and absence of Lis1 (Fig. 3.6B), suggesting that an intact ATP hydrolysis site at AAA1 is required for ATPase activity in the presence of Lis1.

Given that Lis1 binds at AAA4, one of the hydrolysis-competent AAA+ modules in dynein, it was possible that Lis1 might be stimulating ATP hydrolysis at that site, with AAA1 playing only an indirect role. However, dynein carrying an E to Q mutation in the Walker B motif of AAA4 (Cho et al., 2008; Heald et al., 1996; Kiyomitsu and Cheeseman, 2013; Merdes et al., 1996) showed a near wild type ATPase rate (Fig. 3.6C) with or without Lis1. Therefore, a hydrolysis-competent AAA4 is not required for the ATPase activity observed in the presence of Lis1.

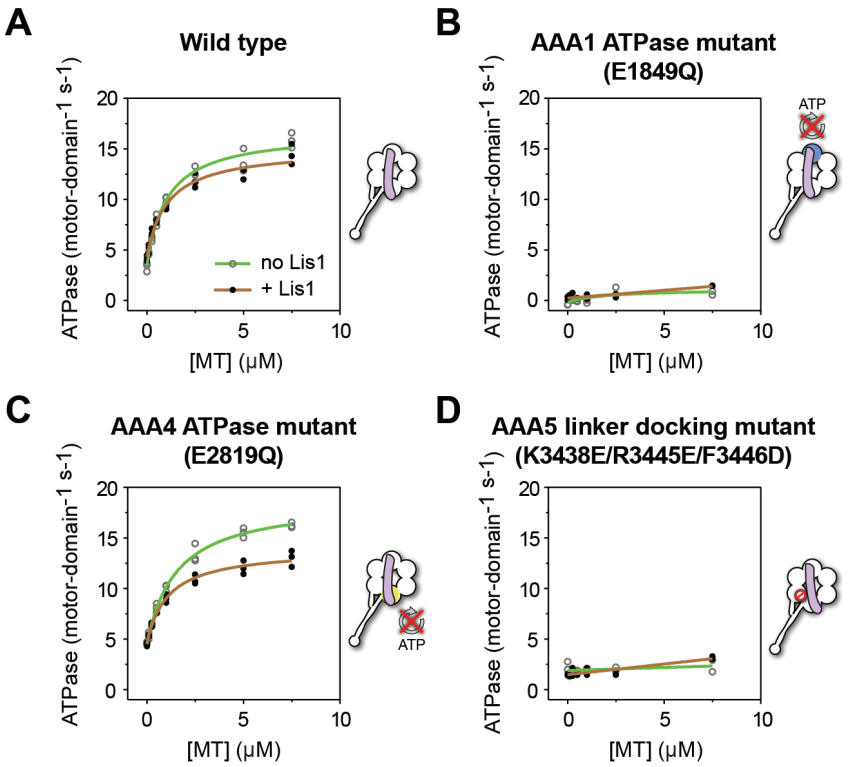

Figure 3.6 ATP turnover in the presence of Lis1 requires a hydrolysis-competent AAA1 and a functional AAA5 inker-docking site
Microtubule-stimulated ATPase activity of dynein monomers carrying **(A)** wild-type AAA+ modules, **(B)** a hydrolysis deficient E1849Q mutation in AAA1 (Kon et al., 2004), **(C)** a hydrolysis deficient E2819Q mutation in AAA4 (Cho et al., 2008), **(D)** AAA5 mutations (K3438E, R3445E, F3446D) that prevent linker docking (Schmidt et al., 2012). ATPase traces are of dynein alone (light green) or in the presence of 140 nM Lis1 (brown). Measurements were done in triplicate (A,C) or duplicate (B,D) from one preparation. Diagrams of the dynein constructs used to generate the plots are shown next to them. See Table A3.3 for fit equation and rate quantifications.

Mutations in AAA5 (a AAA+ module that cannot bind ATP) that prevent linker docking have been shown to severely reduce dynein's ATPase activity (Schmidt et al., 2012; Wilkie and Davis, 2001). We wondered whether Lis1 binding might rescue this mutation and restore ATPase activity to dynein. This was not the case; dynein constructs carrying the AAA5 mutation did not hydrolyze ATP even in the presence of Lis1 (Fig. 3.6D).

Taken together, these results indicate that sustained ATP hydrolysis in a

Lis1-regulated dynein requires a hydrolysis-competent AAA1 and a functional linker-docking site at AAA5.

Removing Lis1's steric block by shortening dynein's linker makes the motor Lis1-insensitive

The experiments discussed above showed that Lis1 does not regulate dynein by affecting the linker's ability to reach its pre-powerstroke position at AAA2. Our dynein-Lis1 structure shows that Lis1, however, does affect post-powerstroke linker positions, as Lis1 and the linker are sterically incompatible in no nucleotide and ADP conditions (Fig. 3.2B,C, Fig. 3.4B). We wondered whether motility regulation was a result of this steric blocking by Lis1. Specifically, we wanted to test the hypothesis that steric blocking of the linker is necessary for inducing dynein's Lis1-dependent state of persistent microtubule attachment. To test this hypothesis we used a dynein construct with a truncated linker that is long enough to form a functional motor but is too short to be sterically blocked by Lis1. This construct is generated by deleting 145 amino acids at the N-terminus of the dynein motor (Fig. 3.7A).

We began by verifying this construct functionally and structurally. A dimeric dynein motor containing this shortened linker shows robust motility properties in *in vitro* motility assays (Fig. A2.5A,B) (Reck-Peterson et al., 2006). A monomeric dynein carrying a shortened linker can bind Lis1 as shown both by their co-migration in size exclusion chromatography (Fig. A2.5C) and by our ability to obtain a 3D reconstruction of a dynein-Lis1 complex carrying a short

Figure 3.7 A shortened linker that can physically bypass Lis1 renders dynein Lis1-insensitive

(A) A short linker construct was designed by docking the crystal structure of the *D. discoideum* linker (purple ribbon) (Kon et al., 2012) into our EM map of dynein alone and overlaying the position of Lis1 (brown mesh). Truncating the linker at residue 1365 (dashed line) yields a linker that can interact with AAA5 (green circle) (Schmidt et al., 2012) but can no longer contact Lis1. **(B)** Cryo-NS reconstruction of the short linker dynein-Lis1 complex; the linker can now dock at AAA5 with Lis1 bound. **(C)** Diagram of the single-molecule microtubule release assay to test Lis1 regulation of dynein. Release from microtubules of TMR-labeled (red asterisk) dynein monomers on addition of ATP is monitored by TIRF microscopy. **(D)** Diagrams of predicted outcomes. Dynein's linker domain in purple, microtubule in gray, Lis1 in brown and linker-AAA5 interaction marked with a green circle. (i) Dynein monomers release from microtubules in ATP conditions in the absence of Lis1. (ii) The dynein-Lis1 EM map suggests that Lis1 prevents a full-length linker from docking at AAA5, keeping dynein bound to the microtubule. (iii) In the absence of Lis1, shortening the linker would have no effect on dynein's mechanochemical cycle. (iv) A shortened linker that can bypass Lis1 yet still bind to AAA5 should render dynein insensitive to Lis1. **(E)** Kymographs of TMR-labeled full-length (left) or short linker (right) dynein molecules. After pre-binding to microtubules, release of dynein molecules is monitored after addition of 5 mM ATP, with and without 300 nM Lis1. Kymographs correspond to the dynein constructs shown in (d). Scale bar = 5s. **(F)** Quantification of the kymographs in (d), showing the duration of microtubule attachment after addition of ATP, in the absence (grey) or presence (brown) of Lis1. Data was binned into 1s intervals and the histograms show alternating no Lis1 and +Lis1 bars. Rare attachments longer than 10 s were excluded from the analysis and plot, N ≥183.

Figure 3.7 (Continued)

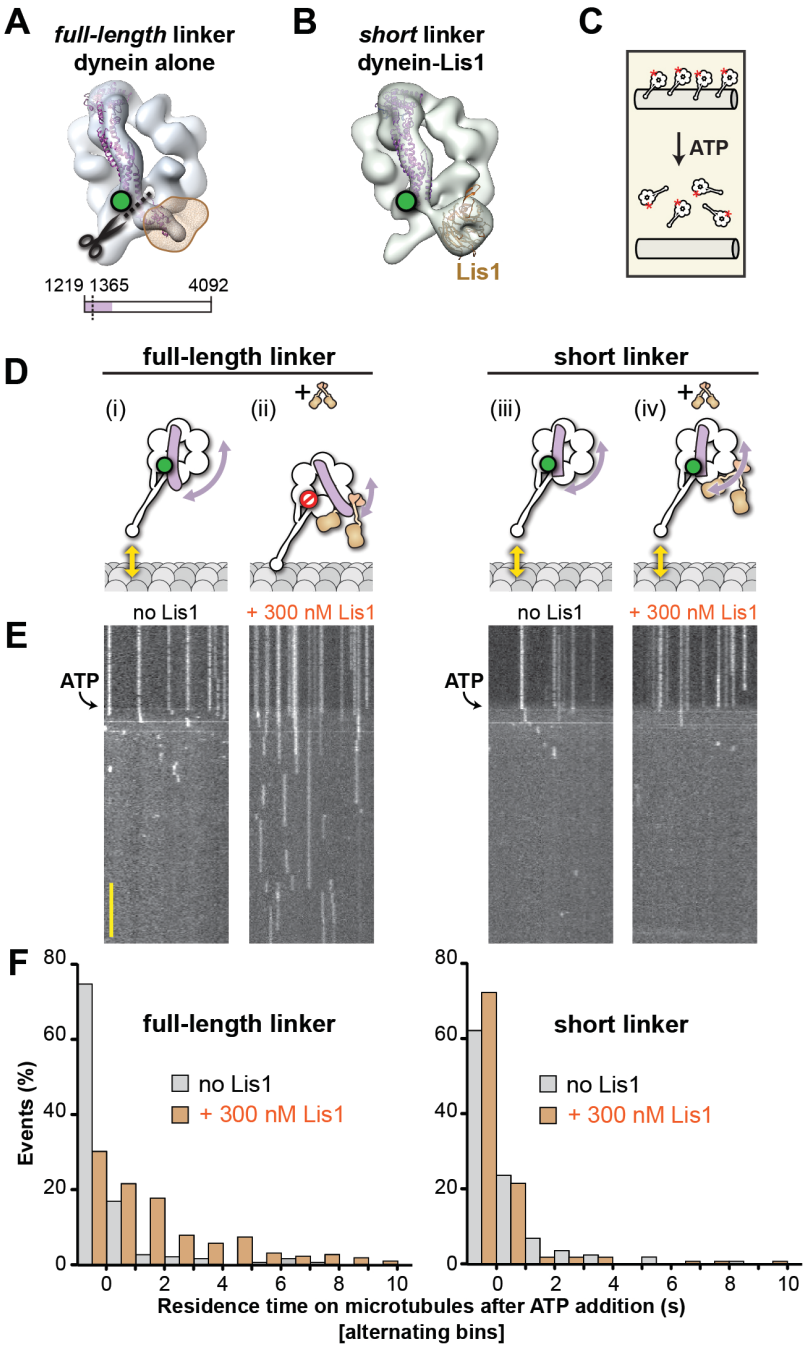

linker (Fig. 3.7B).Central to our testing the steric block hypothesis, our 3D structure of the short linker dynein-Lis1 complex shows the same conformation for the linker in the presence of Lis1 as we had observed for the full-length linker in its absence (Fig. 3.2, and 3.7A,B). We also tested whether shortening the linker affects the microtubule-stimulated ATPase activity of dynein monomers. Monomers with a short linker showed ATPase levels comparable to those seen with a full-length linker, both in the context of a wild type set of AAA+ modules and in the linker docking-deficient AAA5 mutant (Fig. A2.5D). Therefore, the short linker is functional and able to physically bypass Lis1.

We next tested whether Lis1 was capable of regulating dynein with a short linker using a single-molecule microtubule release assay (Fig. 3.7C). Here, the duration of single monomeric dynein's attachment to microtubules can be measured by kymograph analysis in a flow chamber by TIRF microscopy (Burgess et al., 2003; Huang et al., 2012; Kon et al., 2005; Roberts et al., 2009; 2012; Shima et al., 2006). Addition of ATP triggers a low-affinity state in dynein (Gibbons et al., 2005; Huang et al., 2012; Imamula et al., 2007; Kon et al., 2005; 2009; Redwine et al., 2012) and the dynein monomers release from microtubules, resulting in a loss of fluorescence signal. Microtubule rebinding events are short lived, likely corresponding to single turnovers of ATP. In the presence of a full-length linker, Lis1 converted dynein to a state of persistent microtubule attachment and dynein monomers stayed bound in the presence of ATP for extended periods (Fig. 3.5d–f (Huang et al., 2012; Reiner et al., 1993)). Strikingly, shortening of dynein's linker eliminated Lis1's ability to induce this persistent microtubule-bound state. We quantified the duration of microtubule attachment after the addition of ATP and found the same short-lived attachments seen with dynein in the

absence of Lis1 (Fig. 3.7D-F). Thus, Lis1 is not capable of regulating microtubule attachment in the short linker construct. These data support a linker-centric mode of dynein regulation where Lis1 prevents the linker from reaching its AAA5 docking site.

Discussion

We previously described Lis1 as a "clutch" for dynein, based on its ability to uncouple the cycles of ATP hydrolysis, which take place in the motor domain, from the cycles of microtubule binding and release at the microtubule binding domain (Huang et al., 2012). One of the functional consequences of the dynein-Lis1 interaction is that Lis1 keeps dynein in a persistent microtubule-bound state. Here, we have determined six 3D EM structures of dynein and dynein-Lis1 in different nucleotide states. By combining these structures with single molecule motility experiments, we have established that Lis1 regulates dynein's microtubule attachment by sterically blocking its linker domain.

Together, our data suggest the following model of dynein regulation by Lis1 (Fig. 3.8). In the current view of dynein's mechanochemical cycle, the motor domain encounters the microtubule with ADP.P_i bound at AAA1, with the linker in a pre-powerstroke position at AAA2 (Kon et al., 2005; Roberts et al., 2009; 2012). Strong microtubule binding stimulates P_i release, inducing the linker to swing to AAA4 (Kon et al., 2012). Finally, linker docking at AAA5 is thought to promote the release of ADP from AAA1, resetting the mechanochemical cycle (Schmidt et al., 2012). Our data suggest that when Lis1 is present, the linker retains its ability to adopt the pre-powerstroke AAA2 position but is prevented from reaching its normal post-powerstroke positions at AAA4 and AAA5 on dynein's ring (Fig. 3.8). This blocking of the linker by Lis1 is critical for

motility regulation; its removal by shortening dynein's linker renders the motor Lis1-insensitive.

Why does Lis1's blocking the linker from adopting its normal post-powerstroke positions prevent dynein's microtubule detachment? One possibility suggested by our structures is that Lis1 disrupts the interaction between the linker and AAA5, preventing normal progression through the mechanochemical cycle. Consistent with this notion, when linker docking at AAA5 is abolished by mutagenesis, dynein displays reduced velocity and prolonged microtubule attachments (Schmidt et al., 2012), reminiscent of Lis1's effects. However, while Lis1 has little effect on dynein's ATPase, AAA5 linker docking mutants display severely reduced ATPase rates, both in the absence (Schmidt et al., 2012) and presence of Lis1 (Fig. 3.6D, Fig. A2.7D). Given these results, it is not clear at this point what the mechanistic basis is for dynein's continuing ATPase in the presence of Lis1. On the one hand, it is possible that the AAA5 mutations may, in addition to preventing linker docking, disrupt dynein's mechanochemical cycle and thus also prevent ATP hydrolysis. A method to reversibly block linker docking at AAA5 (*e.g*. via a small molecule) would be required to determine if AAA5 docking is truly required for dynein ATPase activity. On the other hand, Lis1 may uncouple ATP hydrolysis from linker docking at AAA5 through an allosteric effect on the ring. In this scenario, the linker-AAA5 interaction, which is blocked by Lis1, would be required for the conformational changes that ultimately shift dynein's microtubule-binding domain to its low-affinity state, but not for dynein's continuing ATPase activity. Higher resolution structures of the dynein-Lis1 complex will be required to establish whether Lis1 has an effect on the structure of dynein's ring.

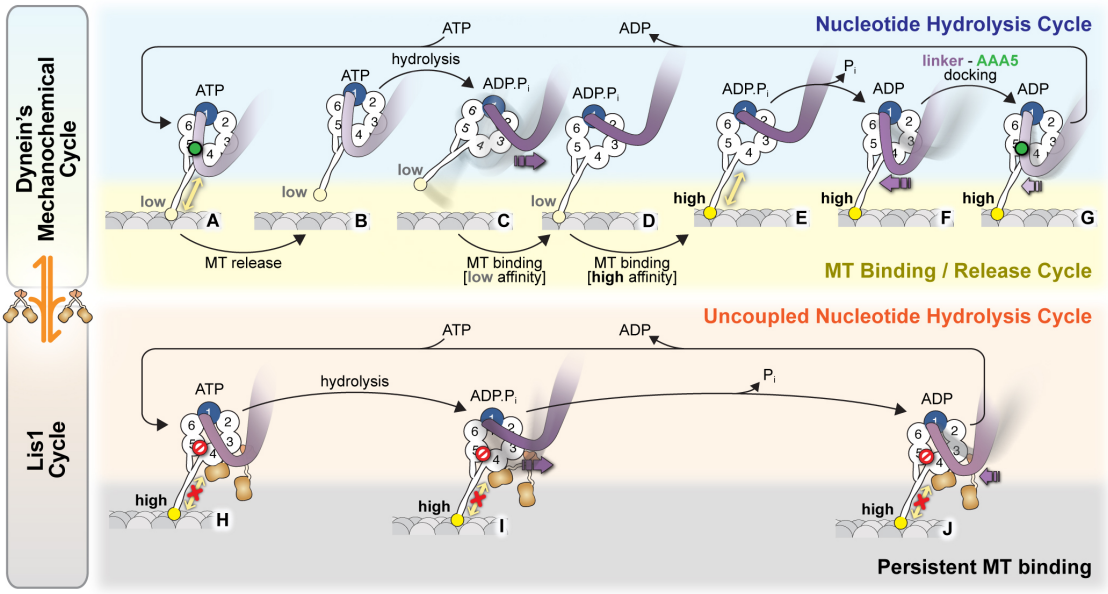

Figure 3.8 Model for the regulation of dynein by Lis1
(A-G) Current view of dynein's mechanochemical cycle. **(A)** ATP binding to AAA1 induces the low-affinity conformation in dynein's microtubule-binding domain and **(B)** release from the microtubule. **(C)** The linker domain changes its position from AAA5 towards AAA2, the "pre-powerstroke" and ATP is hydrolyzed. **(D)** Binding of dynein to a new site on the microtubule triggers a change in the microtubule-binding domain to its high affinity conformation **(E)**. **(F)** Release of P_i results in the "powerstroke", a movement of the linker back towards AAA5. **(G)** Docking of the linker at AAA5 is thought to promote nucleotide exchange at AAA1, resetting the motor for a new cycle. **(H-J)** Model for the Lis1-regulated cycle. Lis1 prevents the linker from completing its normal conformational cycle, keeping dynein in a persistent microtubule-attached state, despite continuing ATP hydrolysis. **(H)** Binding of Lis1 to dynein blocks the linker from docking onto the ring at AAA5, preventing the conformational changes in the stalk and microtubule binding domain that ultimately result in dynein's release from the microtubule. **(I)** The linker is still capable of moving to the pre-powerstroke position at AAA2 in the presence of Lis1, and ATP is hydrolyzed. **(J)** Presumably, by analogy to the dynein alone cycle, P_i release triggers the power-stroke, but Lis1 sterically blocks the linker's normal position on dynein's ring in the ADP state. Our current understanding of Lis1 regulation does not yet explain the mechanism of nucleotide exchange at AAA1.

It is conceivable that blocking of the normal linker-docking sites by Lis1 might induce a new interaction between the linker and the AAA+ ring. Similarly, Lis1 may interact specifically with the linker itself. Either (or both) of these scenarios could in turn be responsible for preventing microtubule release. However, current evidence does not favor these possibilities. Low sequence conservation in the portion of the linker facing

Lis1 argues against a specific Lis1-linker interaction (Fig. A2.1I). Likewise, a specific interaction between a Lis1-displaced linker and dynein's ring is not supported by the apparent conformational heterogeneity of the N-terminus of the linker in the presence of Lis1 where 3D sorting is required to resolve linker positions (Fig. A2.1 F–H). Also mutating five amino acids on AAA4 proximal to the linker's displaced position (the most likely candidates to interact with the displaced linker) had minimal effect on Lis1-mediated motility regulation (Fig. A2.2). A direct test of whether specific interactions exist among these different elements will also require a higher resolution structure where the rotational orientation of the Lis1 homology model within its density in the EM map is unequivocal and specific interactions between the linker and Lis1 as well as the linker and the dynein ring can be distinguished from physical proximity.

In conclusion, our data show that Lis1, a conserved dynein regulator, directly disrupts dynein's mechanochemical cycle by physically blocking conformations that are required to couple the cycles of ATP hydrolysis taking place in the motor domain from those of track binding and release happening at the microtubule binding domain. This allows Lis1 to keep dynein in a persistent microtubule-bound state. This modulation of dynein's interaction with its microtubule track likely contributes to dynein's ability to carry out the variety cellular functions it performs in different organisms, given the conservation of the amino acids at the dynein-Lis1 interface. For example, Lis1 is involved in initiation of cargo transport (Egan et al., 2012; Lenz et al., 2006; Moughamian et al., 2013), in transport of high load cargo (McKenney et al., 2010), and in targeting dynein molecules to the cell cortex via the microtubule plus end (Lee et al., 2003; Roberts et al., 2014; Sheeman et al., 2003). The displaced linker observed in the

presence of Lis1 in our 3D dynein-Lis1 reconstruction may contribute to this latter task, generating an “unmasked” tail domain that has been shown necessary for cortical dynein localization (Markus and Lee, 2011). In the case of the mammalian proteins, dynein and Lis1 were previously shown to form a stable complex only in ATP and V_i conditions (McKenney et al., 2010). Our 3D reconstruction of dynein-Lis1 under those conditions suggests this might be a consequence of the linker’s moving to its pre-powerstroke site at AAA2, where the linker and Lis1 are no longer sterically incompatible.

The work presented here has helped dissect the molecular mechanism by which Lis1 regulates a single dynein motor domain. The next challenge will be to understand the interactions between Lis1 and dynein dimers and of those with other regulatory factors. Future structural studies with full-length dimeric dynein-Lis1-Nudel complexes, free and bound to microtubules, will be required to answer these exciting questions.

Acknowledgements

We would like to thank Jeff Moore (University of Colorado School of Medicine) for yeast strains, Vu Nguyen, Rogelio Hernandez-Lopez, Michael Cianfrocco, John Srouji and Julie Huang for their contributions during this work, Morgan deSantis for comments on the manuscript, and Liza Sholl for administrative support. EM data were collected at Harvard’s Center for Nanoscale Systems, a member of the National Nanotechnology Infrastructure Network and supported by the National Science Foundation (NSF) (ECS-0335765). Computation was performed in part on the Odyssey cluster supported by Harvard’s FAS Science Division Research Computing Group. Single molecule data

were collected in part at Harvard's Center for Biological Imaging, supported by an SIG award (RR1S1027990) from the NIH. Spinning disc confocal microscopy data was collected at the Nikon Imaging Center at Harvard Medical School. K.T. was supported by a Charles King postdoctoral fellowship. A.J.R. is a Sir Henry Fellow supported by the Wellcome Trust (092436/Z/10/Z) sponsored by Peter J. Knight and Stan A. Burgess (University of Leeds). S.L.R-P. was supported by the Rita Allen Foundation.

References

Aguet, F., Antonescu, C.N., Mettlen, M., Schmid, S.L., and Danuser, G. (2013). Advances in Analysis of Low Signal-to-Noise Images Link Dynamin and AP2 to the Functions of an Endocytic Checkpoint. Developmental Cell *26*, 279–291.

Blocker, A., Severin, F.F., Burkhardt, J.K., Bingham, J.B., Yu, H., Olivo, J.C., Schroer, T.A., Hyman, A.A., and Griffiths, G. (1997). Molecular requirements for bi-directional movement of phagosomes along microtubules. The Journal of Cell Biology *137*, 113–129.

Burgess, S.A., Walker, M.L., Sakakibara, H., Knight, P.J., and Oiwa, K. (2003). Dynein structure and power stroke. Nature *421*, 715–718.

Cardone, G., Heymann, J.B., and Steven, A.C. (2013). One number does not fit all: mapping local variations in resolution in cryo-EM reconstructions. Journal of Structural Biology *184*, 226–236.

Carragher, B., Kisseberth, N., Kriegman, D., Milligan, R.A., Potter, C.S., Pulokas, J., and Reilein, A. (2000). Leginon: an automated system for acquisition of images from vitreous ice specimens. Journal of Structural Biology *132*, 33–45.

Carter, A.P., Garbarino, J.E., Wilson-Kubalek, E.M., Shipley, W.E., Cho, C., Milligan, R.A., Vale, R.D., and Gibbons, I.R. (2008). Structure and Functional Role of Dynein's Microtubule-Binding Domain. Science *322*, 1691–1695.

Carter, A.P. (2013). Crystal clear insights into how the dynein motor moves. Journal of Cell Science *126*, 705–713.

Case, R.B., Pierce, D.W., Hom-Booher, N., Hart, C.L., and Vale, R.D. (1997). The directional preference of kinesin motors is specified by an element outside of the motor catalytic domain. Cell *90*, 959–966.

Cho, C., Reck-Peterson, S.L., and Vale, R.D. (2008). Regulatory ATPase Sites of Cytoplasmic Dynein Affect Processivity and Force Generation. Journal of Biological Chemistry *283*, 25839–25845.

Clegg, R.M. (1995). Fluorescence resonance energy transfer. Current Opinion in Biotechnology *6*, 103–110.

De Carlo, S., and Stark, H. (2010). Cryonegative Staining of Macromolecular Assemblies. Methods in Enzymology *481*, 127–145.

Driskell, O.J., Mironov, A., Allan, V.J., and Woodman, P.G. (2007). Dynein is required for receptor sorting and the morphogenesis of early endosomes. Nature Cell Biology *9*, 113–120.

Egan, M.J., Tan, K., and Reck-Peterson, S.L. (2012). Lis1 is an initiation factor for dynein-driven organelle transport. The Journal of Cell Biology *197*, 971–982.

Gee, M.A., Heuser, J.E., and Vallee, R.B. (1997). An extended microtubule-binding structure within the dynein motor domain. Nature *390*, 636–639.

Gibbons, I.R., Garbarino, J.E., Tan, C.E., Reck-Peterson, S.L., Vale, R.D., and Carter, A.P. (2005). The Affinity of the Dynein Microtubule-binding Domain Is Modulated by the Conformation of Its Coiled-coil Stalk. Journal of Biological Chemistry *280*, 23960–23965.

Gibbons, I.R., Gibbons, B.H., Mocz, G., and Asai, D.J. (1991). Multiple nucleotide-binding sites in the sequence of dynein beta heavy chain. Nature *352*, 640–643.

Gibbons, I.R., Lee-Eiford, A., Mocz, G., Phillipson, C.A., Tang, W.J., and Gibbons, B.H. (1987). Photosensitized cleavage of dynein heavy chains. Cleavage at the “V1 site” by irradiation at 365 nm in the presence of ATP and vanadate. *262*, 2780–2786.

Gietz, R.D., and Woods, R.A. (2002). Transformation of yeast by lithium acetate/single-stranded carrier DNA/polyethylene glycol method. Methods in Enzymology *350*, 87–96.

Guthrie, C., and Fink, G.R. (1991). Guide to Yeast Genetics and Molecular Biology (Methods in Enzymology, Academic Press).

Heald, R.R., Tournebize, R.R., Blank, T.T., Sandaltzopoulos, R.R., Becker, P.P., Hyman, A.A., and Karsenti, E.E. (1996). Self-organization of microtubules into bipolar spindles around artificial chromosomes in Xenopus egg extracts. Nature *382*, 420–425.

Huang, J., Roberts, A.J., Leschziner, A.E., and Reck-Peterson, S.L. (2012). Lis1 Acts as a “‘Clutch’” betweenthe ATPase and Microtubule-Binding Domains of the Dynein Motor. Cell *150*, 975–986.

Imamula, K., Kon, T., Ohkura, R., and Sutoh, K. (2007). The coordination of cyclic microtubule association/dissociation and tail swing of cytoplasmic dynein. Proceedings

of the National Academy of Sciences of the United States of America *104*, 16134–16139.

Jaspersen, S.L., and Winey, M. (2004). The budding yeast spindle pole body: structure, duplication, and function. Annu. Rev. Cell Dev. Biol.

Jordens, I.I., Fernandez-Borja, M.M., Marsman, M.M., Dusseljee, S.S., Janssen, L.L., Calafat, J.J., Janssen, H.H., Wubbolts, R.R., and Neefjes, J.J. (2001). The Rab7 effector protein RILP controls lysosomal transport by inducing the recruitment of dynein-dynactin motors. Current Biology : CB *11*, 6–6.

Kim, M.H., Cooper, D.R., Oleksy, A., Devedjiev, Y., Derewenda, U., Reiner, O., Otlewski, J., and Derewenda, Z.S. (2004). The Structure of the N-Terminal Domain of the Product of the Lissencephaly Gene Lis1 and Its Functional Implications. Structure *12*, 987–998.

Kiyomitsu, T., and Cheeseman, I.M. (2013). Cortical dynein and asymmetric membrane elongation coordinately position the spindle in anaphase. Cell *154*, 391–402.

Kon, T., Imamula, K., Roberts, A.J., Ohkura, R., Knight, P.J., Gibbons, I.R., Burgess, S.A., and Sutoh, K. (2009). Helix sliding in the stalk coiled coil of dynein couples ATPase and microtubule binding. Nat. Struct. Mol. Biol. *16*, 325–333.

Kon, T., Mogami, T., Ohkura, R., Nishiura, M., and Sutoh, K. (2005). ATP hydrolysis cycle–dependent tail motions in cytoplasmic dynein. Nat. Struct. Mol. Biol. *12*, 513–519.

Kon, T., Nishiura, M., Ohkura, R., Toyoshima, Y.Y., and Sutoh, K. (2004). Distinct Functions of Nucleotide-Binding/Hydrolysis Sites in the Four AAA Modules of Cytoplasmic Dynein †. Biochemistry *43*, 11266–11274.

Kon, T., Oyama, T., Shimo-Kon, R., Imamula, K., Shima, T., Sutoh, K., and Kurisu, G. (2012). The 2.8 A˚ crystal structure of the dynein motor domain. Nature 1–7.

Kural, C., Kim, H., Syed, S., Goshima, G., Gelfand, V.I., and Selvin, P.R. (2005). Kinesin and dynein move a peroxisome in vivo: a tug-of-war or coordinated movement? Science (New York, NY) *308*, 1469–1472.

Lander, G.C., Stagg, S.M., Voss, N.R., Cheng, A., Fellmann, D., Pulokas, J., Yoshioka, C., Irving, C., Mulder, A., Lau, P.-W., et al. (2009). Appion: an integrated, database-driven pipeline to facilitate EM image processing. Journal of Structural Biology *166*, 95–102.

Lee, W.-L., Oberle, J.R., and Cooper, J.A. (2003). The role of the lissencephaly protein Pac1 during nuclear migration in budding yeast. The Journal of Cell Biology *160*, 355–364.

Lenz, J.H., Schuchardt, I., Straube, A., and Steinberg, G. (2006). A dynein loading zone for retrograde endosome motility at microtubule plus-ends. The EMBO Journal *25*,

2275–2286.

Longtine, M.S., McKenzie, A., Demarini, D.J., Shah, N.G., Wach, A., Brachat, A., Philippsen, P., and Pringle, J.R. (1998). Additional modules for versatile and economical PCR-based gene deletion and modification in Saccharomyces cerevisiae. Yeast (Chichester, England) *14*, 953–961.

Ludtke, S.J., Baldwin, P.R., and Chiu, W. (1999). EMAN: semiautomated software for high-resolution single-particle reconstructions. Journal of Structural Biology *128*, 82–97.

Markus, S.M., and Lee, W.-L. (2011). Regulated Offloading of Cytoplasmic Dynein from Microtubule Plus Ends to the Cortex. Developmental Cell *20*, 639–651.

McKenney, R.J., Vershinin, M., Kunwar, A., Vallee, R.B., and Gross, S.P. (2010). LIS1 and NudE Induce a Persistent Dynein Force-Producing State. Cell *141*, 304–314.

Merdes, A., Ramyar, K., Vechio, J.D., and Cleveland, D.W. (1996). A complex of NuMA and cytoplasmic dynein is essential for mitotic spindle assembly. Cell *87*, 447–458.

Moore, J.K., Stuchell-Brereton, M.D., and Cooper, J.A. (2009). Function of dynein in budding yeast: Mitotic spindle positioning in a polarized cell. Cell Motil. Cytoskeleton *66*, 546–555.

Moughamian, A.J., Osborn, G.E., Lazarus, J.E., Maday, S., and Holzbaur, E.L.F. (2013). Ordered Recruitment of Dynactin to the Microtubule Plus-End is Required for Efficient Initiation of Retrograde Axonal Transport. J. Neurosci. *33*, 13190–13203.

Nishiura, M. (2004). A Single-headed Recombinant Fragment of Dictyostelium Cytoplasmic Dynein Can Drive the Robust Sliding of Microtubules. Journal of Biological Chemistry *279*, 22799–22802.

Pilling, A.D., Horiuchi, D., Lively, C.M., and Saxton, W.M. (2006). Kinesin-1 and Dynein are the primary motors for fast transport of mitochondria in Drosophila motor axons. Molecular Biology of the Cell *17*, 2057–2068.

Reck-Peterson, S.L., Yildiz, A., Carter, A.P., Gennerich, A., Zhang, N., and Vale, R.D. (2006). Single-Molecule Analysis of Dynein Processivity and Stepping Behavior. Cell *126*, 335–348.

Redwine, W.B., Hernandez-Lopez, R., Zou, S., Huang, J., Reck-Peterson, S.L., and Leschziner, A.E. (2012). Structural Basis for Microtubule Binding and Release by Dynein. Science *337*, 1532–1536.

Reiner, O., Carrozzo, R., Shen, Y., Wehnert, M., Faustinella, F., Dobyns, W.B., Caskey, C.T., and Ledbetter, D.H. (1993). Isolation of a Miller-Dieker lissencephaly gene containing G protein beta-subunit-like repeats. Nature *364*, 717–721.

Roberts, A.J., Malkova, B., Walker, M.L., Sakakibara, H., Numata, N., Kon, T., Ohkura,

R., Edwards, T.A., Knight, P.J., Sutoh, K., et al. (2012). ATP-driven remodeling of the linker domain in the dynein motor. Structure (London, England : 1993) *20*, 1670–1680.

Roberts, A.J., Numata, N., Walker, M.L., Kato, Y.S., Malkova, B., Kon, T., Ohkura, R., Arisaka, F., Knight, P.J., Sutoh, K., et al. (2009). AAA+ Ring and Linker Swing Mechanism in the Dynein Motor. Cell *136*, 485–495.

Schmidt, H., Gleave, E.S., and Carter, A.P. (2012). Insights into dynein motor domain function from a 3.3-Å crystal structure. Nat. Struct. Mol. Biol. *19*, 492–497.

Sheeman, B., Carvalho, P., Sagot, I., Geiser, J., Kho, D., Hoyt, M.A., and Pellman, D. (2003). Determinants of S. cerevisiae dynein localization and activation: implications for the mechanism of spindle positioning. Current Biology : CB *13*, 364–372.

Shima, T., Kon, T., Imamula, K., Ohkura, R., and Sutoh, K. (2006). Two modes of microtubule sliding driven by cytoplasmic dynein. Proceedings of the National Academy of Sciences of the United States of America *103*, 17736–17740.

Sorzano, C.O.S., Marabini, R., Velázquez-Muriel, J., Bilbao-Castro, J.R., Scheres, S.H.W., Carazo, J.M., and Pascual-Montano, A. (2004). XMIPP: a new generation of an open-source image processing package for electron microscopy. Journal of Structural Biology *148*, 194–204.

Tang, G., Peng, L., Baldwin, P.R., Mann, D.S., Jiang, W., Rees, I., and Ludtke, S.J. (2007). EMAN2: an extensible image processing suite for electron microscopy. Journal of Structural Biology *157*, 38–46.

Tarricone, C., Perrina, F., Monzani, S., Massimiliano, L., Kim, M.-H.H., Derewenda, Z.S., Knapp, S., Tsai, L.-H.H., and Musacchio, A. (2004). Coupling PAF signaling to dynein regulation: structure of LIS1 in complex with PAF-acetylhydrolase. Neuron *44*, 809–821.

Torisawa, T., Nakayama, A., Furuta, K., Yamada, M., Hirotsune, S., and Toyoshima, Y.Y. (2011). Functional dissection of LIS1 and NDEL1 towards understanding the molecular mechanisms of cytoplasmic dynein regulation. The Journal of Biological Chemistry *286*, 1959–1965.

Vale, R.D. (2003). The molecular motor toolbox for intracellular transport. Cell *112*, 467–480.

van Heel, M., Harauz, G., Orlova, E.V., Schmidt, R., and Schatz, M. (1996). A new generation of the IMAGIC image processing system. Journal of Structural Biology *116*, 17–24.

Wilkie, G.S.G., and Davis, I.I. (2001). Drosophila wingless and Pair-Rule Transcripts Localize Apically by Dynein-Mediated Transport of RNA Particles. Cell *105*, 11–11.

Yamada, M., Toba, S., Yoshida, Y., Haratani, K., Mori, D., Yano, Y., Mimori-Kiyosue, Y.,

Nakamura, T., Itoh, K., Fushiki, S., et al. (2008). LIS1 and NDEL1 coordinate the plus-end-directed transport of cytoplasmic dynein. The EMBO Journal *27*, 2471–2483.

Yeh, E., Skibbens, R.V., Cheng, J.W., Salmon, E.D., and Bloom, K. (1995). Spindle dynamics and cell cycle regulation of dynein in the budding yeast, Saccharomyces cerevisiae. The Journal of Cell Biology *130*, 687–700.

Yin, J., Straight, P.D., McLoughlin, S.M., Zhou, Z., Lin, A.J., Golan, D.E., Kelleher, N.L., Kolter, R., and Walsh, C.T. (2005). Genetically encoded short peptide tag for versatile protein labeling by Sfp phosphopantetheinyl transferase. PNAS *102*, 15815–15820.

Chapter 4 : Conclusions and future directions

My thesis work, using a combination of cryo-EM structural biology and single-molecule approaches, has provided novel insights into how dynein interacts with its microtubule track and how microtubule binding is regulated by the ubiquitous co-factor, Lis1.

Summary and Discussions of Chapter 2

Chapter 2 investigated how dynein binds to its microtubule track. Our work revealed that binding to the microtubule triggers large conformational changes in dynein's MTBD. We hypothesized that these structural changes then lead to changes in the stalk's coiled coil register and further structural changes in the AAA+ ring that could regulate the nucleotide state at AAA1. Using our structure to guide molecular dynamics simulations allowed us to come up with a model of the molecular basis for dynein's interaction with the microtubule. Specifically, these simulations allowed us to identify two dynamic salt bridge switches in the MTBD, which can either interact intramolecularly within dynein or intermolecularly between dynein and the microtubule. Single-molecule functional studies showed that these salt bridges tuned dynein's affinity for the microtubule. Finally, our experiments revealed that dynein is much less processive than it could be, suggesting that suboptimal processivity may have evolved to allow a broader dynamic range for regulation.

The next step in this project will be to determine the structure of an entire dynein monomer bound to the microtubule. Comparison of this structure with the existing structures of free monomeric dynein (Carter et al., 2011; et al., 2011; Kon et al., 2012; Nishikawa et al., 2014; Schmidt et al., 2012) will reveal more information about the mechanism of allosteric communication between the MTBD, the stalk and the AAA+ ring.

Going a step further, the structure of a dynein dimer bound to the microtubule would reveal insights regarding how dynein steps along the microtubule, as well as potential communication mechanisms between protomers. Some technical hurdles to overcome for these studies include utilizing methods for heterogeneous samples (dynein is very flexible) (Scheres, 2012a, 2012b) , as well as identifying methods to obtain either full ordered decoration or sparse decoration of the microtubule by dynein. A major technical advance in the EM field, direct electron detectors, should allow high resolution to be attained if these technical hurdles can be addressed (Bai et al., 2013; Liao et al., 2013) . One method that may increase microtubule decoration will be to use the highly processive mutants that we discovered in our study (Redwine et al., 2012) . Furthermore, since our work was published we have determined that a double mutant, with both salt bridges mutated, leads to the most processive dynein observed to date. This may allow us to achieve better dynein decoration of microtubules.

Our work raised the question: has dynein evolved to be sub-maximally processive? To shed light on this, future experiments could evaluate if high processivity is detrimental in living cells/organisms. In our lab, we work with two *in vivo* systems, the budding yeast *Saccharomyces cerevisiae* and the filamentous fungus *Aspergillus nidulans*, where this question could be tested. In yeast, the sole role of dynein is to pull on microtubules (while anchored at the cortex), which leads to spindle alignment and proper nuclear segregation. This process begins with dynein first being transported to the microtubule plus end by a kinesin (Kip2). Recent *in vitro* reconstitution studies in our lab suggested that dynein is not a passive passenger, rather it engages in a tug-of-war with Kip2 (Roberts et al., 2014) . Thus, one hypothesis for why high processivity is

detrimental is that highly processive dynein will overcome Kip2 in the tug-of-war, resulting in decreased dynein being delivered to the cortex. Current work in our lab suggests that relative to wild-type dynein, fewer highly processive dynein mutants arrive at microtubule plus ends and fewer dynein molecules are present on the cell cortex (Redwine et al. unpublished data). *Aspergillus nidulans* is another good system to test the consequence of highly processive dynein, where dynein transports many organelles, including endosomes, peroxisomes, and autophagosomes (Egan et al., 2012a, 2012b; Tan et al., 2014) .

Summary and Discussions of Chapter 3

Chapter 3 investigated how dynein is regulated by Lis1. Our new 3D cryo-EM structures of the dynein-Lis1 complex and mutagenesis revealed a clearer picture of the dynein/Lis1 interaction. Lis1 binds to dynein's AAA+ ring at AAA4. With Lis1 bound to dynein, dynein's mechanical element, the linker, is found in an altered position. Based on our new structures, FRET and single-molecule functional studies, we were able to expand on our "clutch" model for dynein regulation by Lis1 (Huang et al., 2012) . We proposed that Lis1 binding to dynein sterically blocks the dynein linker from reaching its normal docking site on the AAA+ ring. This interaction is required for dynein release from microtubules. Thus, by preventing linker docking, Lis1 prevents release from microtubules.

One important future direction for this project will be to improve the resolution of the dynein-Lis1 complex. This will likely be achievable using the newly developed direct electron detectors (Bai et al., 2013; Liao et al., 2013) . A higher-resolution dynein/Lis1

structure will likely reveal the exact docking orientation of Lis1 in the dynein-Lis1 complex. This will allow mutagenesis studies to be performed that will identify key residues at the dynein/Lis1 interface. This interface appears to be based on electrostatic interaction, thus it may be possible to design mutants of dynein and Lis1 where charged residues at the dynein/Lis1 interface have been swapped.

Another direction on the structural biology front will be to determine structures of dimeric dynein with dimeric Lis1, as well as structures of full-length dynein, dimeric Lis1 and Nudel. Earlier work indicated that dimeric Lis1 might adopt different conformations when alone vs. in the presence of binding partners (Kim et al., 2004; Tarricone et al., 2004) . In addition, our own previous work indicated that dynein's two motor domains are closer together in the presence of dimeric Lis1 (Huang et al., 2012) .

A major outstanding question regarding how Lis1 regulates dynein is to determine why dynein's ATPase activity continues in the presence of Lis1, but microtubule detachment is uncoupled from the ATPase cycle. Does Lis1 stimulate the activity of a specific AAA domain? It is difficult to explore AAA modules individually. However, a recently developed technique, nCoMET, is a promising tool, which tags a fluorescent reporter locally near the nucleotide binding pocket of a particular AAA+ domain. The reporter's fluorescence can be quenched upon Co^{2+} binding, which substitutes for Mg^{2+} (Stinson et al., 2013) In this way, we would be able to monitor individual AAA's activity by measuring its local reporter's fluorescence intensity in the presence or absence of Lis1.

Another question that remains to be determined is if Lis1 binding to dynein is nucleotide-dependent. Mckenney et al. (McKenney et al., 2010) found that Lis1 only

binds mammalian dynein at its pre-power stroke stage (ATP.Vi), while Huang and Roberts (Huang et al., 2012) showed that Lis1 can bind yeast dynein under all nucleotide states tested (Huang et al., 2012; McKenney et al., 2010) While these may represent species-specific differences, it is also possible that the affinity of Lis1 for dynein is nucleotide dependent. To determine this, more comprehensive Lis1-dynein binding affinity measurements at different states need to be performed. One straightforward way to do this is to use a range of concentrations of Lis1-bound beads to deplete a low and fixed concentration of dynein from the solution (Pollard, 2010) isothermal titration calorimetry (ITC), which would measure the heat change from the solution reaction, or fluorescence polarization (FP), another solution-based technique that would monitor the polarization change of fluorescently-labeled Lis1 upon dynein binding.

Other future directions

There are still a number of important questions to be addressed in the dynein field. I describe some of these below.

(1) What is the structural basis for full-length dynein interacting with its cofactors Lis1-Nudel and the dynactin complex? I expect that high-resolution structures will reveal the mechanistic basis for dynein inhibition by Lis1 and dynein activation by dynactin. Cryo-EM using the new direct electron detector will be ideally suited for this purpose.

(2) How do opposite polarity motors ultimately move cargos unidirectionally? Recent work suggests that motor regulation is required. The DNA origami system

developed in our lab (Derr et al., 2012) will be an ideal tool for investigating mechanisms of opposite polarity motor regulation.

(3) How does a single type of dynein transport different cargo? While in yeast, dynein has only a single known cargo, in filamentous fungi and metazoan organisms dynein transports many different organellar, RNA, and protein cargos. How is binding to specific cargos achieved? Does binding to cargo regulate dynein's motile properties? Several recent papers suggest that this may be the case (Bielska et al., 2014; McKenney et al., 2014; Schlager et al., 2014; Zhang et al., 2014) Proteomic and genetic approaches can be used to identify additional adaptors.

(4) How are unidirectional motors recycled to the start of their track? Recent *in vitro* reconstitution demonstrated a minimal protein system essential to target dynein to the start of the track, the plus end of the microtubule (Duellberg et al., 2014; Roberts et al., 2014) . Next, it will be interesting to investigate how dynein is activated at the plus end to move towards the microtubule minus-end. Furthermore, what happens at the end of a run?

(5) To what extent has dynein from different organisms evolved differently in term of the structure and regulatory mechanism? Mammalian dynein has been less studied than the yeast and *Dictyostelium discoideum* dyneins in the past due to a lack of recombinant proteins. However, recent work has succeeded in developing recombinant mammalian dynein (Schlager et al., 2014; Trokter et al., 2012) , which will allow its mechanism to be dissected and compared to other dyneins.

(6) Can cargo transport be manipulated non-invasively in living cells? Recently a light-sensitive peptide was engineered into the lever arm of kinesin and myosin motors,

allowing regulation of speed and direction in response to blue light (Nakamura et al., 2014) . The basis for dynein directionality and speed is currently under investigation. Upon gaining this understanding a goal for the future will be to develop methods to control dynein's activity with light. Ultimately, being able to control both dynein and kinesin motility in living cells will allow dissection and control of bidirectional microtubule-based transport in living cells.

References

Bai, X.-C.C., Fernandez, I.S., McMullan, G., and Scheres, S.H. (2013). Ribosome structures to near-atomic resolution from thirty thousand cryo-EM particles. eLife *2*, e00461.

Bielska, E, Schuster, M, Roger, Y, and Berepiki, A (2014). Hook is an adapter that coordinates kinesin-3 and dynein cargo attachment on early endosomes.
Carter, A.P., Cho, C., Jin, L., and Vale, R.D. (2011). Crystal structure of the dynein motor domain. Science (New York, N.Y.) *331*, 1159–1165.

Derr, N.D., Goodman, B.S., Jungmann, R., Leschziner, A.E., Shih, W.M., and Reck-Peterson, S.L. (2012). Tug-of-war in motor protein ensembles revealed with a programmable DNA origami scaffold. Science (New York, N.Y.) *338*, 662–665.
Duellberg, C., Trokter, M., Jha, R., Sen, I., Steinmetz, M.O., and Surrey, T. (2014). Reconstitution of a hierarchical +TIP interaction network controlling microtubule end tracking of dynein. Nature Cell Biology *16*, 804–811.

Egan, M.J., Tan, K., and Reck-Peterson, S.L. (2012a). Lis1 is an initiation factor for dynein-driven organelle transport. The Journal of Cell Biology *197*, 971–982.

Egan, M.J., McClintock, M.A., and Reck-Peterson, S.L. (2012b). Microtubule-based transport in filamentous fungi. Current Opinion in Microbiology *15*, 637–645.

Huang, J., Roberts, A.J., Leschziner, A.E., and Reck-Peterson, S.L. (2012). Lis1 acts as a "clutch" between the ATPase and microtubule-binding domains of the dynein motor. Cell *150*, 975–986.

Kim, MH, Cooper, DR, Oleksy, A, and Devedjiev, Y (2004). The Structure of the N-Terminal Domain of the Product of the Lissencephaly Gene Lis1 and Its Functional Implications. Structure *12*, 987-98.

Kon, T., Sutoh, K., and Kurisu, G. (2011). X-ray structure of a functional full-length dynein motor domain. Nature Structural & Molecular Biology *18*, 638–642.

Kon, T., Oyama, T., Shimo-Kon, R., Imamula, K., Shima, T., Sutoh, K., and Kurisu, G. (2012). The 2.8 Å crystal structure of the dynein motor domain. Nature *484*, 345–350.

Liao, M., Cao, E., Julius, D., and Cheng, Y. (2013). Structure of the TRPV1 ion channel determined by electron cryo-microscopy. Nature *504*, 107–112.

McKenney, R., Vershinin, M., Kunwar, A., Vallee, R., and Gross, S. (2010). LIS1 and NudE induce a persistent dynein force-producing state. Cell *141*, 304–314.

McKenney, R., Huynh, W., Tanenbaum, M., Bhabha, G., and Vale, R. (2014). Activation of cytoplasmic dynein motility by dynactin-cargo adapter complexes. Science (New York, N.Y.) *345*, 337–341.

Nakamura, M., Chen, L., Howes, S.C., Schindler, T.D., Nogales, E., and Bryant, Z. (2014). Remote control of myosin and kinesin motors using light-activated gearshifting. Nature Nanotechnology *9*, 693–697.

Nishikawa, Y., Oyama, T., Kamiya, N., Kon, T., Toyoshima, Y.Y., Nakamura, H., and Kurisu, G. (2014). Structure of the entire stalk region of the Dynein motor domain. Journal of Molecular Biology *426*, 3232–3245.

Pollard, T.D. (2010). A guide to simple and informative binding assays. Molecular Biology of the Cell *21*, 4061–4067.

Redwine, W.B., Hernández-López, R., Zou, S., Huang, J., Reck-Peterson, S.L., and Leschziner, A.E. (2012). Structural basis for microtubule binding and release by dynein. Science (New York, N.Y.) *337*, 1532–1536.

Roberts, A.J., Goodman, B.S., and Reck-Peterson, S.L. (2014). Reconstitution of dynein transport to the microtubule plus end by kinesin. eLife *3*, e02641.

Scheres, S.H. (2012a). RELION: implementation of a Bayesian approach to cryo-EM structure determination. Journal of Structural Biology *180*, 519–530.

Scheres, S.H. (2012b). A Bayesian view on cryo-EM structure determination. Journal of Molecular Biology *415*, 406–418.

Schlager, M.A., Hoang, H., Urnavicius, L., Bullock, S.L., and Carter, A.P. (2014). In vitro reconstitution of a highly processive recombinant human dynein complex. The EMBO Journal *33*, 1855-68.

Schmidt, H., Gleave, E.S., and Carter, A.P. (2012). Insights into dynein motor domain function from a 3.3-Å crystal structure. Nature Structural & Molecular Biology *19*, 492–7.

Stinson, B.M., Nager, A.R., Glynn, S.E., Schmitz, K.R., Baker, T.A., and Sauer, R.T. (2013). Nucleotide binding and conformational switching in the hexameric ring of a AAA+ machine. Cell *153*, 628–639.

Tan, K., Roberts, A.J., Chonofsky, M., Egan, M.J., and Reck-Peterson, S.L. (2014). A microscopy-based screen employing multiplex genome sequencing identifies cargo-specific requirements for dynein velocity. Molecular Biology of the Cell *25*, 669–678.

Tarricone, C., Perrina, F., Monzani, S., Massimiliano, L., Kim, M.-H.H., Derewenda, Z.S., Knapp, S., Tsai, L.-H.H., and Musacchio, A. (2004). Coupling PAF signaling to dynein regulation: structure of LIS1 in complex with PAF-acetylhydrolase. Neuron *44*, 809–821.

Trokter, M., Mucke, N., and Surrey, T. (2012). Reconstitution of the human cytoplasmic dynein complex. Proceedings of the National Academy of Sciences *109*, 20895-900.

Zhang, J., Qiu, R., Arst, H.N., Peñalva, M.A., and Xiang, X. (2014). HookA is a novel dynein-early endosome linker critical for cargo movement in vivo. The Journal of Cell Biology *204*, 1009–1026.

Appendix 1 : Supplementary Materials for Structural basis for microtubule binding and release by dynein

William Bret Redwine*, Rogelio Hernandez-Lopez*, Sirui Zou, Julie Huang,

Samara Reck-Peterson, Andres Leschziner

Contributions

Bret Redwine and Rogelio Hernandez-Lopez contributed equally. Bret Redwine initiated the project and performed biochemistry, sample preparation, and electron microscopy data collection. Rogelio Hernandez-Lopez and William Redwine performed 3D reconstruction. Rogelio Hernandez-Lopez performed molecular dynamics simulations. Sirui Zou performed single molecule motility experiments for dynamic salt bridge dynein mutants. Julie Huang tested wild-type dynein's salt-dependent motility properties. Andres Leschziner and Samara Reck-Peterson provided mentorship. This work was published in: Structural basis for microtubule binding and release by dynein. *Science* **337**, 1532-1536 (2012).

Supplementary figures and tables

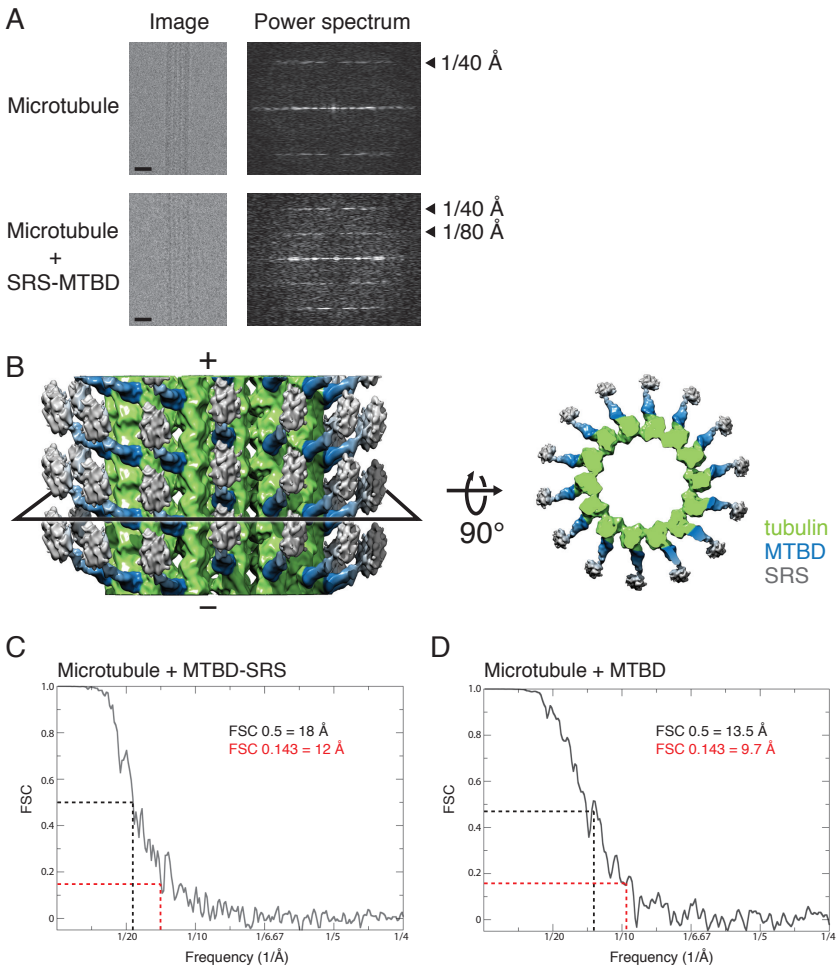

Figure A1.1 Complete reconstruction of the high-affinity SRS-MTBD construct bound to a MT

(**A**) Left: Images containing MTs only (top) and MTs highly decorated with the high-affinity SRS-MTBD (bottom). Scale bar represents 20 nm. Right: Corresponding power spectra of the MTs. Note the layer lines at 1/40 Å and 1/80 Å, which correspond to the repeated units of tubulin monomers and SRS-MTBD, respectively. (**B**) Left: A segment of the MT + SRS-MTBD reconstruction low-pass filtered to 12 Å. MT polarity is indicated by plus and minus signs. Note that the stalk emerges from the MT at an angle of ~60°, consistent with previous observations (Carter et al., 2008; Mizuno et al., 2004). Right: A slice taken through the volume, related to the complete reconstruction by a 90° rotation, such that the viewer is looking down the MT from the minus end. The color of each component is indicated and refers to both views. (**C**) The estimated resolution of the complete volume, including the SRS, is 12 Å, using the 0.143 criterion (red dashed line). (**D**) The estimated resolution of the volume containing only the MT and MTBD is 9.7 Å, using the 0.143 criterion (red dashed line). The discrepancy in resolutions is likely due to a relatively less constrained SRS domain decreasing the overall resolution of the structure.

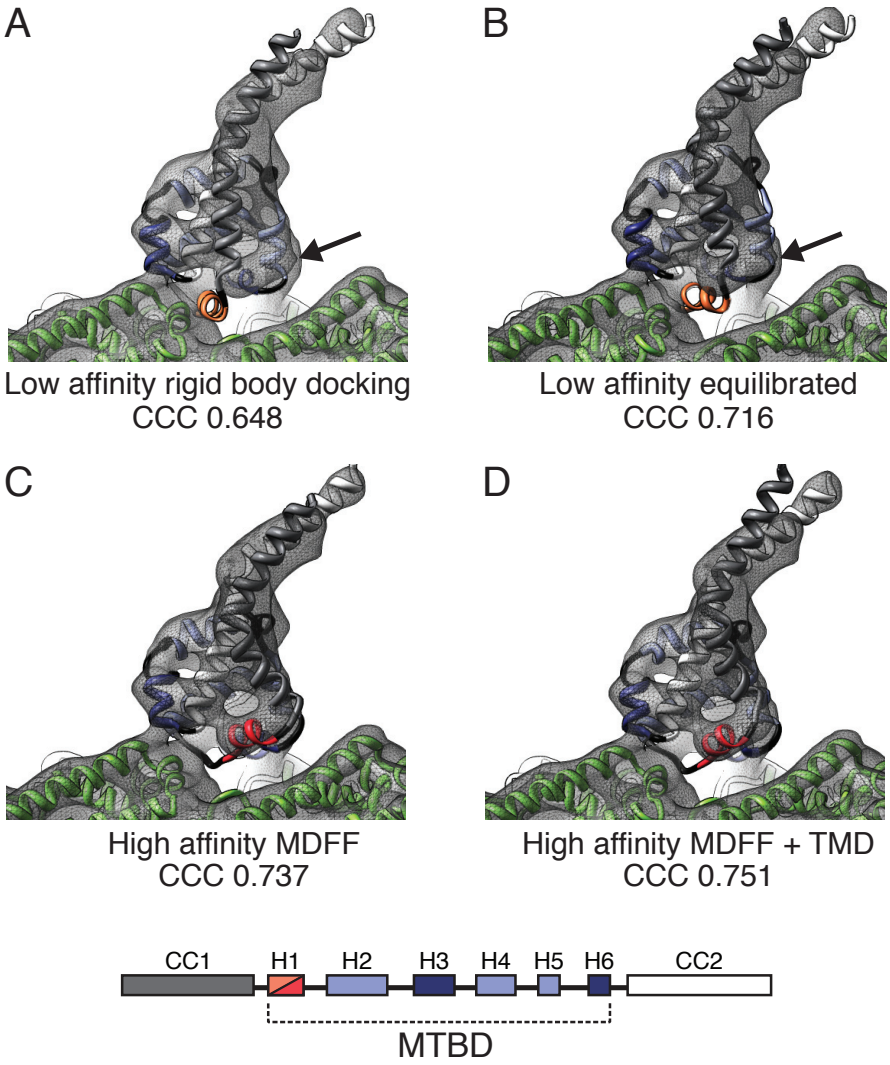

Figure A1.2 Molecular Dynamics study of the dynein MTBD conformations bound to MTs.

(**A**) Crystal structures of the low-affinity conformation (PDB 3ERR (Carter et al., 2008)) and tubulin (Wells and Aksimentiev, 2010) rigid-body docked into our cryo-EM density map. H1 is shown in orange and displays steric clashes with the MT. Adjacent to H1 is an unoccupied portion of the map (black arrow). (**B**) Pseudo-atomic model of the low-affinity conformation bound to MTs obtained after 15 ns of MD simulations. H1 moves to a position that avoids clashes with the MT. (**C**) Pseudo-atomic model of a putative intermediate state obtained after molecular dynamics flexible fitting (MDFF). The repositioning of H1 and H3 is achieved but the coiled-coil registry is still in the low-affinity conformation. (**D**) Pseudo-atomic model of the dynein MTBD in its high-affinity state obtained after MDFF and targeted molecular dynamics (TMD). The coordinates of the Cα atoms corresponding to a shift of half heptad (4 aa) were used as a target position to guide the registry shift. The cross-correlation coefficient (CCC) between the target density map and each structure at 9.7 Å resolution is indicated below each panel. Color-coding is indicated for each set of structures.

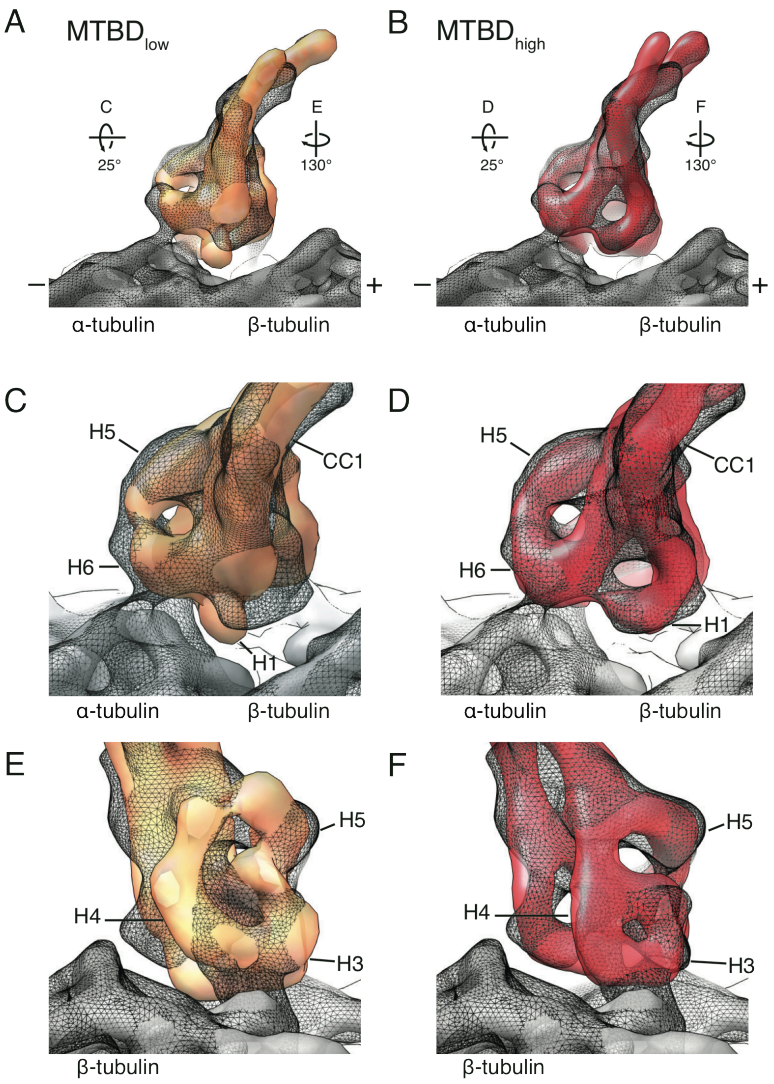

Figure A1.3 Comparison of 10 Å synthetic maps of the low- and high-affinity MTBD conformations with our experimental map

The stalk and MTBD of the low-affinity conformation (Carter et al., 2008) and the pseudo-atomic model of the high-affinity conformation of the MTBD were converted to synthetic EM maps, filtered to a resolution of 10 Å, and oriented relative to the cryo-EM map identically to the atomic models shown in Fig. 2.3 (**A**) 10 Å synthetic map of the low-affinity conformation (MTBD$_{low}$, orange) docked into the cryo-EM map (grey mesh). (**C, E**) Close-ups of the structure shown in (A); the direction of each view is indicated in panel (A). (**B**) 10 Å synthetic map of the pseudo-atomic model of the high-affinity conformation (MTBD$_{high}$, red) docked into the cryo-EM map. (**D, F**) Close-ups of the structure shown in (B); the direction of each view is indicated in panel (B). The synthetic map of the low-affinity conformation protrudes from our experimental map at several locations (CCC = 0.648), including H1 (C) and H4 (E). In contrast, the synthetic map of the pseudo-atomic model exhibits a better overall fit to our experimental map (CCC = 0.751).

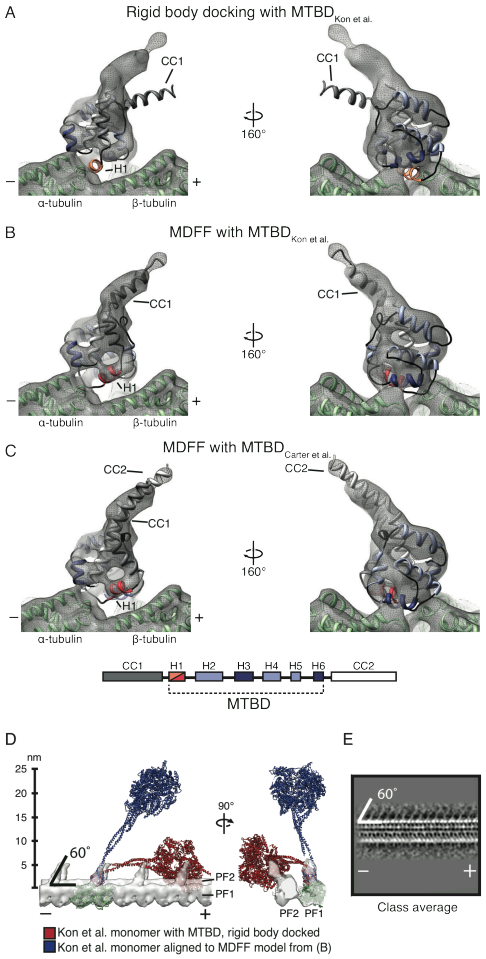

Figure A1.4 Different atomic resolution structures of the MTBD converge on a single MT-bound conformation.

(**A)** The MTBD from a recently reported atomic resolution structure of ADP-bound monomeric dynein (PDB 3VKH (Kon et al., 2012)), labeled $MTBD_{Kon\ et\ al.}$), was rigid-body docked into the experimental map. Note that helices H1 (orange) and CC1 (grey) lie outside of the experimental map. (**B**) Conformation of $MTBD_{Kon\ et\ al.}$ after 12 ns of MDFF. Helices H1 (red) and CC1 (grey) have moved into our experimental map. The conformation of the MTBD used in this study (PDB 3ERR (Carter et al., 2008)) after MDFF ($MTBD_{Carter\ et\ al.}$) is shown for comparison (**C**). Note the similarity of the MDFF models in (B) and (C). (**D**) The atomic resolution structure of ADP-bound monomeric dynein (Kon et al., 2012), shown in red, was rigid body docked into a section of one protofilament (PF1) of the experimental map. The orientation of the MTBD is shown in (A). Tubulin is colored green. The resulting conformation of the entire monomer results in clashes with the neighboring protofilament (PF2). A second monomer model (blue) was obtained by replacing the MTBD (residues 3352 to 3491) from the crystal structure with the MDFF-generated $MTBD_{Kon\ et\ al.}$ shown in (B) (See material and methods for details). The monomer containing the MDFF-generated $MTBD_{Kon\ et\ al.}$ exhibits no clashes with our experimental map, and its overall configuration closely matches class averages of *S. cerevisiae* monomeric dynein bound to MTs (**E**). For panels (D) and (E) the approximate angle of the stalk relative to the MT (~60°) is indicated. For all panels MT polarity is indicated.

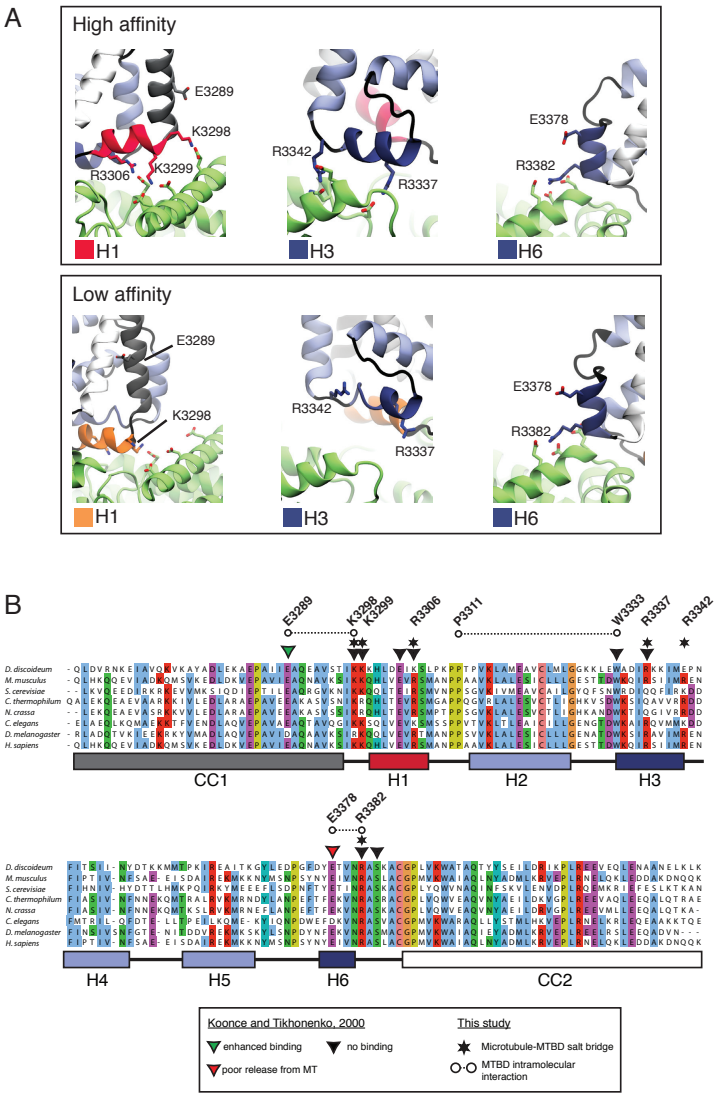

Figure A1.5 Conserved intermolecular MTBD-MT and intramolecular MTBD interactions in the dynein high-affinity state.

(**A**) Top: Salt bridges formed between the MTBD and the MT, as detected by MD simulations in the high-affinity pseudo-atomic model, are labelled within the indicated helices of the MTBD. Bottom: The corresponding views for the MT-bound low-affinity state are shown. Tubulin is colored green. (**B**) Alignment of the MTBD from diverse cytoplasmic dynein sequences calculated with MAFFT (Katoh et al., 2002) and visualized with Jalview (Waterhouse et al., 2009) according to the Clustal coloring scheme for residues with identity ≥ 50%. Of interest to this study, basic and acidic residues are colored red and purple, respectively. Residues that are conserved between *Dictyostelium discoideum* (*Dd*) (Koonce and Tikhonenko, 2000) and *Mus musculus* (*Mm*) (Gibbons et al., 2005) and form salt bridges with MT residues are labeled and annotated according to the legend above. One *Mm* residue, R3342, forms a salt bridge with the MT and is not present in *Dd* dynein. Intramolecular MTBD salt bridges (E3289-K3298 and E3378-R3382, Fig. 2.4) are connected with a dashed line, as is an intramolecular interaction between P3311 and W3333, which is maintained in both high- and low-affinity states.

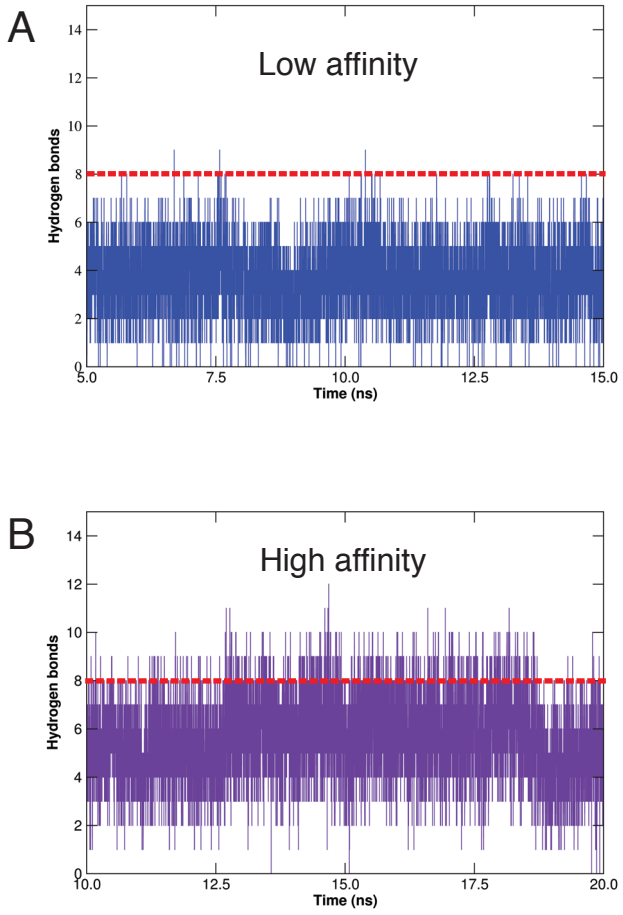

Figure A1.6 Formation of hydrogen bonds between the dynein MTBD and tubulin during MD simulations.
Hydrogen bonds formed between the dynein MTBD and tubulin over time are shown for the (**A**) dynein low-affinity state and the (**B**) dynein high-affinity state. Hydrogen bonds were counted for the last 10 ns of the final MD equilibration simulations when the distance between the donor and acceptor was within 3.0 Å and the angle between donor and hydrogen-acceptor was greater than 160°. A dashed line marks the same point on the y-axis in both graphs.

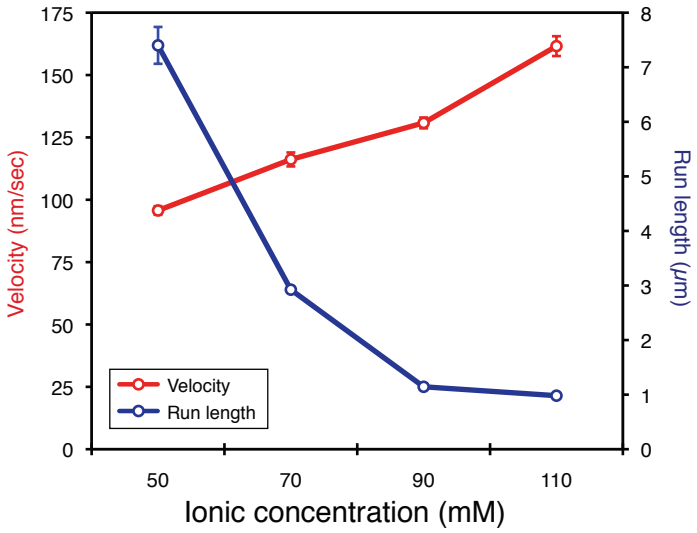

Figure A1.7 Effect of increasing ionic strength on dynein motility.
Fluorescently labeled dynein motors were tracked on axonemes by total internal reflection (TIRF) microscopy. The run length and velocity were determined in assay buffer supplemented with increasing concentrations of potassium acetate (KAc). Total ionic concentration is the sum of added KAc and a constant concentration of buffering agent. The run length at each point is the mean ± standard deviation. The velocity at each point is the mean ± standard error. The average length of analyzed axonemes (mean ± standard deviation) was 24.5 ± 8.0 μm.

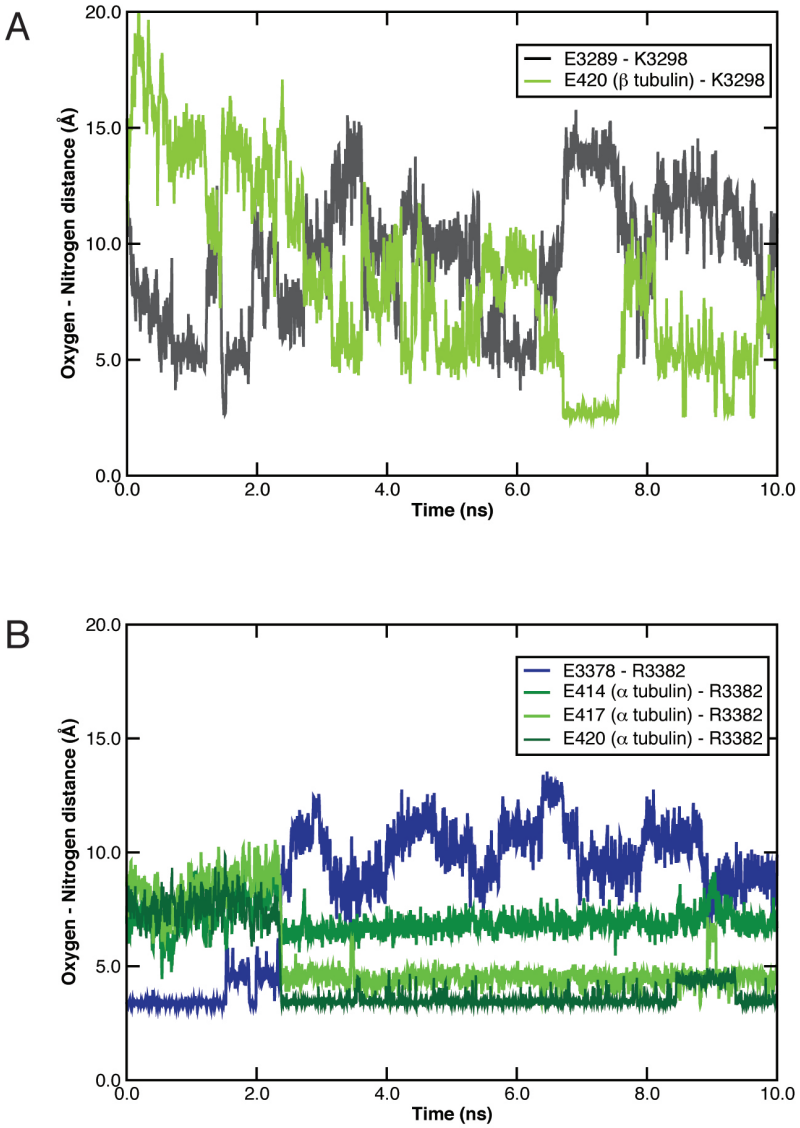

Figure A1.8 Dynamic salt bridges in H1 and H6 of the MTBD as observed by MD simulations

(**A**) Dynamic salt bridges at H1 are formed between K3298 and either E3298 in the dynein MTBD or E420 in β-tubulin. (**B**) Dynamic salt bridges at H6 are formed between R3382 and either E3378 in the dynein MTBD or E414, E417 and E420 in α-tubulin. For both (A) and (B) the average oxygen-nitrogen distances over time for the indicated salt bridges are shown.

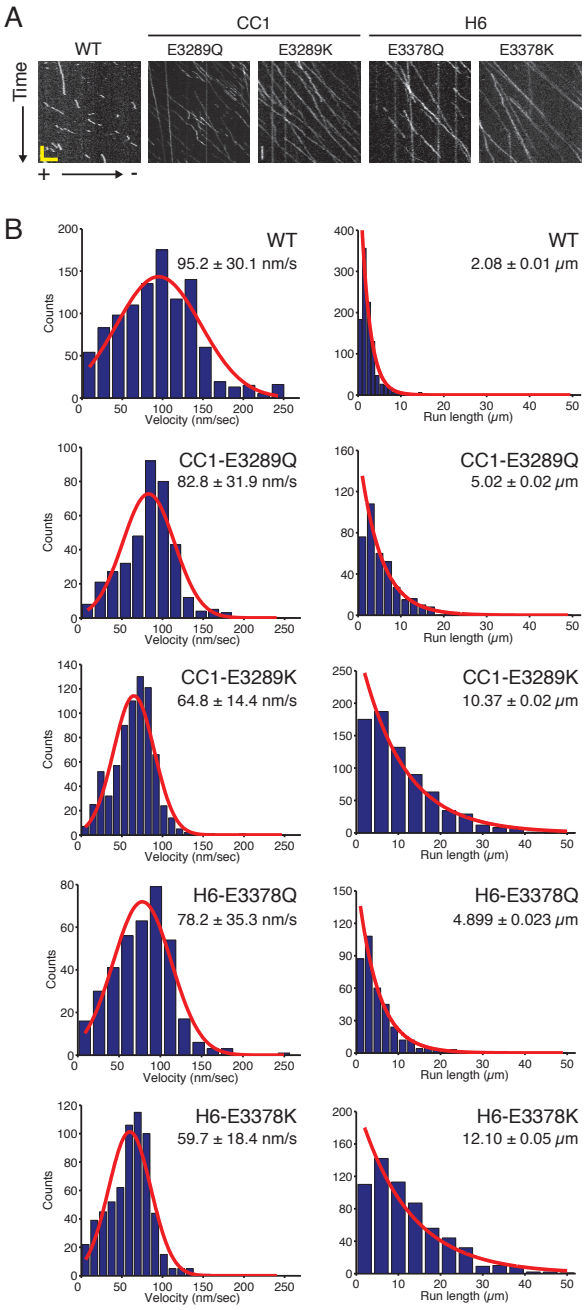

Figure A1.9 Dynamic salt bridges temper dynein motility.
Data corresponds to that reported in Fig. 2.5. (**A**) Representative kymographs of fluorescently labeled dynein and dynein mutants moving along MTs. Each kymograph follows the trajectory of all dynein molecules along a stretch of a single MT. MT polarity is indicated and applies to all panels. Horizontal scale bar, 5 μm; vertical scale bar, 1 min. (**B**) Histograms of velocity and run length of WT dynein and dynein mutants from (A). All velocity data are plotted as mean +/- SD and all run length data are plotted as characteristic run length +/- SE, N>300.

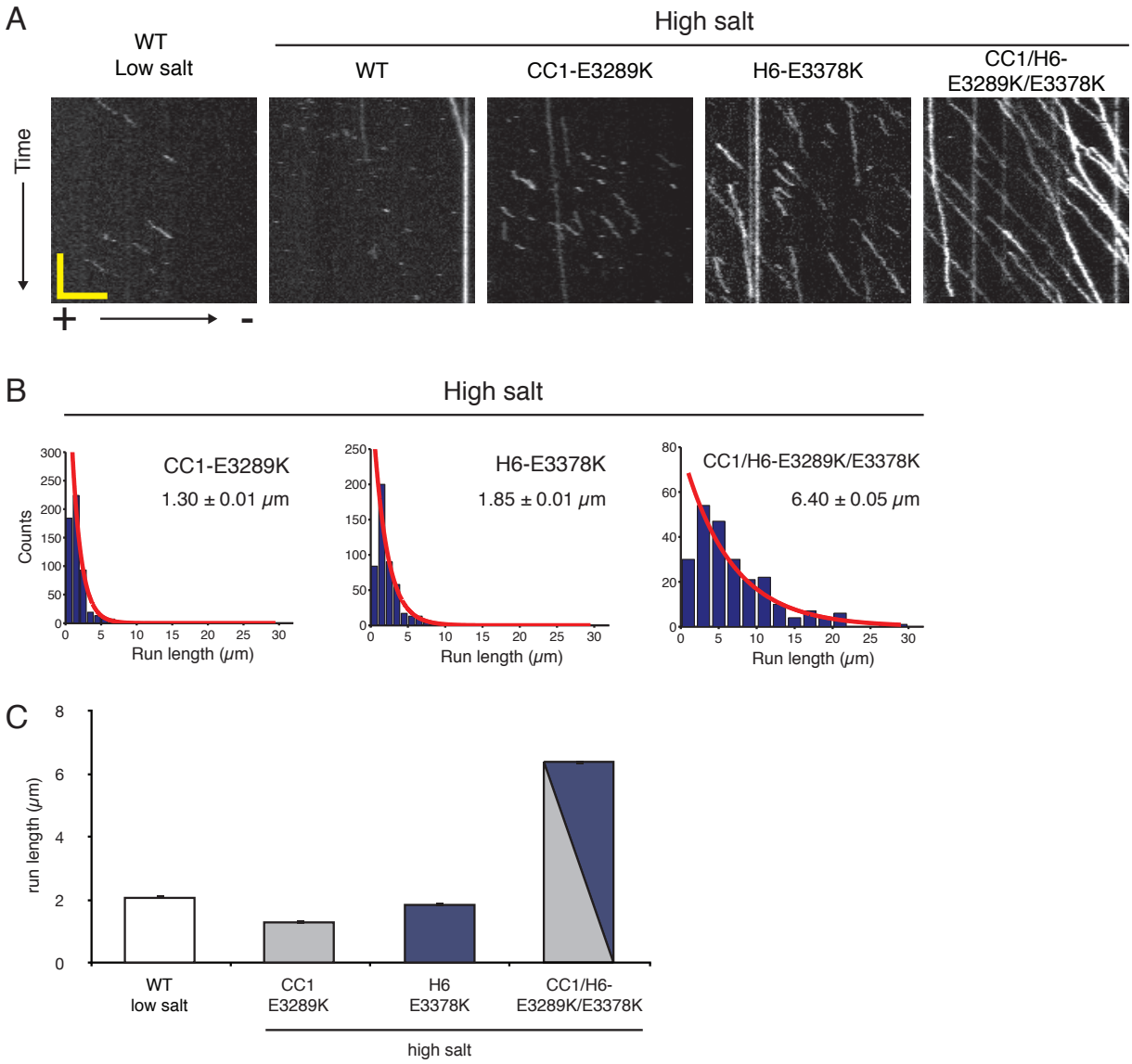

Figure A1.10 Dynamic salt bridge mutations increase dynein processivity under more stringent motility conditions

(**A**) Representative kymographs of fluorescently labeled dynein moving along MTs (low salt = 80 mM total ionic strength, high salt = 130 mM total ionic strength). Note that WT dynein motility is measurable only under low salt conditions, whereas CC1-E3289K and H6-E3378K dynein mutants exhibit run lengths in high salt that are similar to WT run lengths in low salt. The combined CC1/H6-E3289K/E3378K double mutant exhibits much longer run lengths. Horizontal scale bar, 5 μm; vertical scale bar, 1 min. (**B**) Histograms of dynein run length corresponding to (A) are shown with their characteristic run length ± SE, N>250. (**C**) Quantitation of data show in (A) and (B). The differences between CC1-E3289K and H6-E3378K, and H6-E3378K and CC1/H6-E3289K/E3378 are significant (two-tailed KS-test, P<0.01).

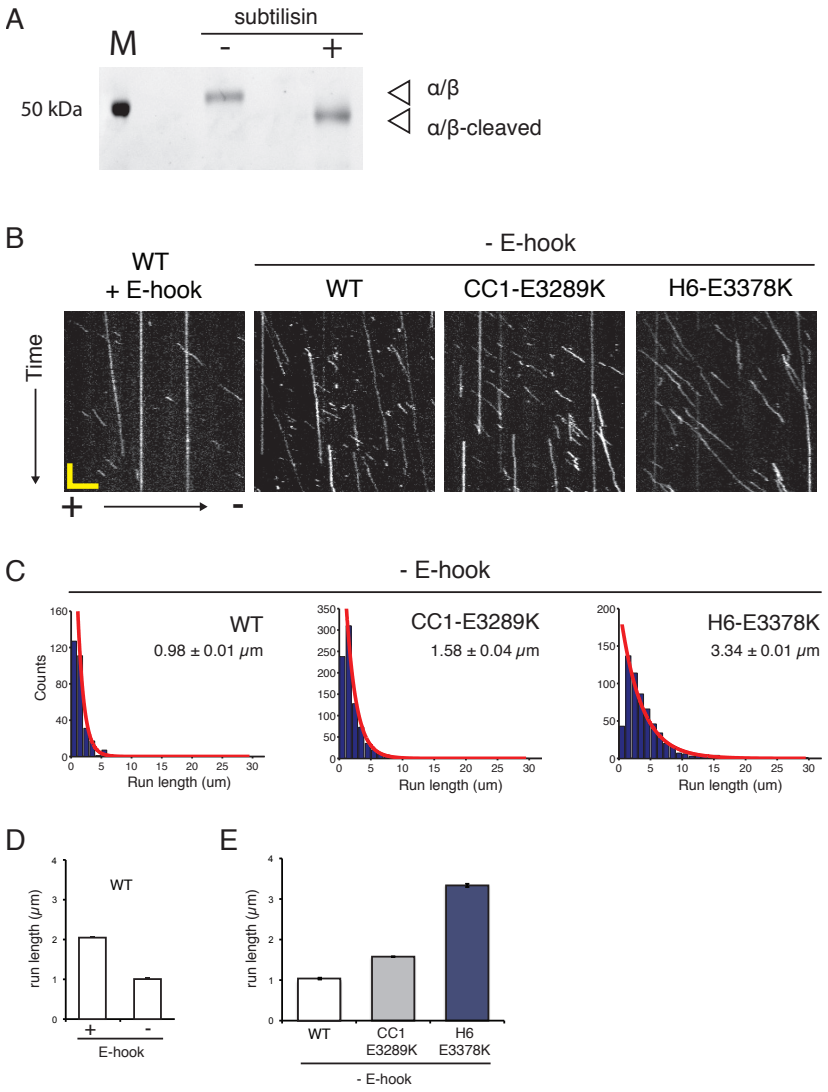

Figure A1.11 Dynamic salt bridge mutations increase dynein processivity independent of tubulin E-hooks.

(**A**) SDS-PAGE analysis of tubulin used in single molecule motility assays. Polymerized MTs were treated with subtilisin, which removes the C-terminal E-hook. Removal of the E-hook causes an increased mobility of α- and β- tubulin on the gel. (**B**) Representative kymographs of fluorescently labeled dynein moving along MTs. The presence or absence of the E-hook is indicated. Note the visibly longer runs in CC1-E3289K and H6-E3378K relative to wild type dynein (WT). Horizontal scale bar, 5 μm; vertical scale bar, 1 min. (**C**) Histograms of dynein run length corresponding to (B) are shown with their characteristic run length ± SE, N>300. (**D**) Quantitation of WT dynein run length on MTs with (+) and without (-) the E-hook. Removal of the E-hook causes a two-fold decrease in run length. The difference is statistically significant (two-tailed KS-test, P<0.01). (**E**) Quantitation of dynein run length on MTs without E-hooks. Note that CC1-E3289K causes a two-fold increase in run length and H6-E3378K causes a greater than three-fold increase in run length relative to WT. The increases are statiscally significant (two-tailed KS-test, P<0.01). Data in (D) and (E) are plotted as characteristic run length +/- SE.

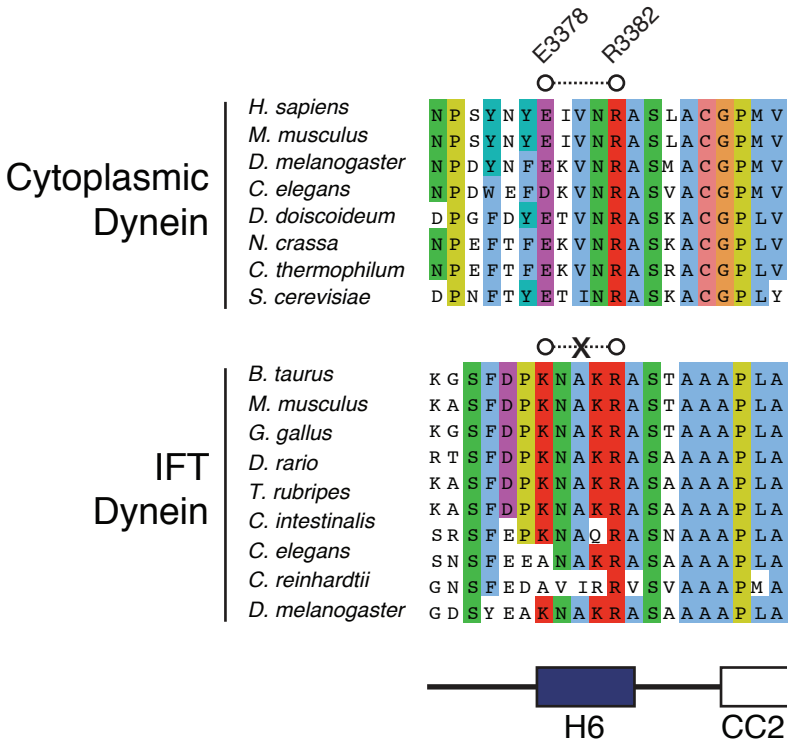

Figure A1.12 Intraflagellar transport (IFT) dynein lacks a key intramolecular salt bridge that tunes the affinity of cytoplasmic dynein.
Alignment of a section of the MTBD from diverse cytoplasmic dynein and IFT dynein (cytoplasmic dynein 2) sequences calculated with MAFFT (Katoh et al., 2002) and visualized with Jalview (Waterhouse et al., 2009) according to the Clustal coloring scheme. An intramolecular salt bridge, whose disruption increases cytoplasmic dynein processivity (Fig. 2.4), is comprised of *Mus musculus* (*Mm*) E3378 and R3382 and is indicated by a dashed line. Note that IFT dynein lacks an acidic residue at the position equivalent to *Mm* E3378, and this position is often basic. This would prevent formation of an intramolecular salt bridge in H6, and indicates that this configuration might enhance IFT dynein processivity.

Table A1.1 Prominent interactions involving the high-affinity state of dynein's MTBD.

Percentages calculated from last 10 ns of MD simulations. Interactions listed were observed for at least 1 ns along the 10 ns trajectory. Omitted were intramolecular hydrogen bonds that form the alpha helices of the dynein's MTBD. * Calculated from 15 ns of MDFF+TMD simulations.

High Affinity State Intermolecular Interactions	
MTBD-tubulin Interaction	**occupancy**
R3382-αE417	23%
R3382-αE420	79%
R3382-αG416	40%
K3299-βE431	60%
K3299-βD427	53%
R3342-βE159	51%
N3310-αG410	38%
L3385-αE415	48%
S3384-αG415	27%
A3383-αE415	49%
R3306-βE196	86%*
R3337-βD199	2%*
R3342-βN197	36%*
High Affinity State Intramolecular Interactions	
MTBD Residues	**occupancy**
K3366-D3402	52%
K3405-E3408	40%
Y3369-E3320	65%
H3301-E3304	62%
R3362-D3359	61%
R3406-D3359	65%
Q3397-S3353	38%
R3306-E3343	19%
K3427-D3423	20%
R3406-D3402	37%
K3282-E3278	11%
T3330-Q3335	16%
K3416-D3420	11%
K3264-E3267	22%
Y3400-E3284	34%
K3416-E3413	12%
T3331-E3320	11%

Table A1.2 Prominent interactions involving the low-affinity state of dynein's MTBD.

Percentages calculated from last 10 ns of MD simulations. Interactions listed were observed for at least 1 ns along the 10 ns trajectory. Omitted were intramolecular hydrogen bonds that form the alpha helices of the dynein's MTBD.

Low Affinity State Intermolecular Interactions	
MTBD-tubulin Interaction	**occupancy**
A3383-αE415	45%
R3382-αG416	44%
R3382-αE417	61%
R3382-αE420	79%
K3299-βE196	27%
S3307-βR253	16%
L3385-αE415	34%
N3310-αK112	10%
Low Affinity State Intramolecular Interactions	
MTBD Residues	**occupancy**
K3366-D3402	61%
R3366-E3363	43%
R3342-E3328	87%
R3411-E3355	51%
S3353-E3356	15%
K3405-E3408	52%
Y3369-E3320	45%
H3301-E3304	37%
K3392-E3289	57%
K3316-E3320	23%
S3321-Y3375	43%
R3362-D3359	59%
K3272-E3413	54%
S3374-N3372	15%
T3331-E3320	29%
K3366-E3363	38%
K3282-D3279	29%
R3406-D3402	20%

Table A1.3 Yeast strains used in this study.

All yeast strains are based on the W303 background. Note that the following relationship between *Saccharomyces cervisiae* (*Sc*) and *Mus musculus* (*Mm*) dynein residues: *Sc*E3107 = *Mm*E3289 and *Sc*E3197 = *Mm*E3378.

Strain ID	Genotype	Source	Figure
RPY98	*MATa, his3-11,5; ura3-52 leu2-3,112; ade2-1, trp-1, pep4Δ::HIS5, PAC11-13Myc-TRP, pGal-ZZ-Tev-GFP-HA-Dyn1$_{331kDa}$*	(Reck-Peterson et al., 2006)	Fig. S4D, E
RPY208	*MATa his3-11,5; ura3-52, leu2-3,112; ade2-1, trp-1, pep4Δ::HIS5, prb1Δ, pGAL-ZZ-TEV-GFP-3XHA-GST-DYN1$_{331kDa}$-gsDHA-kanR*	(Reck-Peterson et al., 2006)	Fig. 4A, B, Fig. S9, 10, 11
RPY237	*MATa, his3-11,5; ura3-52, leu2-3,112; ade2-1, trp-1, pep4**Δ**::HIS5, prb1**Δ**, pac1**Δ**::klURA3, pGAL-ZZ-TEV-GFP-3XHA-GST-DYN1$_{331kDa}$-gsDHA-kanR*	(Reck-Peterson et al., 2006)	Fig. S7
RPY1217	*MATa, his3-11,5; ura3-52, leu2-3,112; ade2-1, trp-1, pep4**Δ**::HIS5, prb1**Δ**, pGAL-ZZ-TEV-GFP-3XHA-GST-DYN1$_{331kDa}$(E3107Q)-gsDHA-kanR*	this study	Fig. 2.5A, B, Fig. A2.9
RPY1218	*MATa, his3-11,5; ura3-52, leu2-3,112; ade2-1, trp-1, pep4**Δ**::HIS5, prb1**Δ**, pGAL-ZZ-TEV-GFP-3XHA-GST-DYN1$_{331kDa}$(E3107K)-gsDHA-kanR*	this study	Fig. 2.5A, B, Fig. A2.9, 10, 11
RPY1233	*MATa, his3-11,5; ura3-52, leu2-3,112; ade2-1, trp-1, pep4**Δ**::HIS5, prb1**Δ**, pGAL-ZZ-TEV-GFP-3XHA-GST-DYN1$_{331kDa}$(E3197Q)-gsDHA-kanR*	this study	Fig. 2.5A, B, Fig. A2.9
RPY1235	*MATa, his3-11,5; ura3-52, leu2-3,112; ade2-1, trp-1, pep4**Δ**::HIS5, prb1**Δ**, pGAL-ZZ-TEV-GFP-3XHA-GST-DYN1$_{331kDa}$(E3197K)-gsDHA-kanR*	this study	Fig. 2.5A, B, Fig. A2.9, 10, 11
RPY1247	*MATa, his3-11,5; ura3-52, leu2-3,112; ade2-1, trp-1, pep4**Δ**::HIS5, prb1**Δ**, pGAL-ZZ-TEV-GFP-3XHA-GST-DYN1$_{331kDa}$(E3107K, E3197K)-gsDHA-kanR*	this study	Fig. A2.11

References

Carter, A.P., Garbarino, J.E., Wilson-Kubalek, E.M., Shipley, W.E., Cho, C., Milligan, R.A., Vale, R.D., and Gibbons, I.R. (2008). Structure and functional role of dynein's microtubule-binding domain. Science *322*, 1691–1695.

Gibbons, I.R., Garbarino, J.E., Tan, C.E., Reck-Peterson, S.L., Vale, R.D., and Carter, A.P. (2005). The affinity of the dynein microtubule-binding domain is modulated by the conformation of its coiled-coil stalk. Journal of Biological Chemistry *280*, 23960–23965.

Katoh, K., Misawa, K., Kuma, K.-I., and Miyata, T. (2002). MAFFT: a novel method for rapid multiple sequence alignment based on fast Fourier transform. Nucleic Acids Research *30*, 3059–3066.

Kon, T., Oyama, T., Shimo-Kon, R., Imamula, K., Shima, T., Sutoh, K., and Kurisu, G. (2012). The 2.8 Å crystal structure of the dynein motor domain. Nature *484*, 345–350.

Koonce, M.P., and Tikhonenko, I. (2000). Functional elements within the dynein microtubule-binding domain. Molecular Biology of the Cell *11*, 523–529.

Mizuno, N., Toba, S., Edamatsu, M., Watai-Nishii, J., Hirokawa, N., Toyoshima, Y.Y., and Kikkawa, M. (2004). Dynein and kinesin share an overlapping microtubule-binding site. The EMBO Journal *23*, 2459–2467.

Reck-Peterson, S.L., Yildiz, A., Carter, A.P., Gennerich, A., Zhang, N., and Vale, R.D. (2006). Single-molecule analysis of dynein processivity and stepping behavior. Cell *126*, 335–348.

Waterhouse, A.M., Procter, J.B., Martin, D.M.A., Clamp, M., and Barton, G.J. (2009). Jalview Version 2--a multiple sequence alignment editor and analysis workbench. Bioinformatics (Oxford, England) *25*, 1189–1191.

Wells, D.B., and Aksimentiev, A. (2010). Mechanical properties of a complete microtubule revealed through molecular dynamics simulation. Biophysical Journal *99*, 629–637.

Appendix 2 : Supplementary Materials for Lis1 regulates dynein by sterically blocking its mechanochemical cycle

Sirui Zou*, Katerina Toropova*, Anthony Roberts, William Redwine, Brian Goodman,

Samara Reck-Peterson and Andres E. Leschziner

Contributions

Sirui Zou and Katerina Toropova contributed equally. Sirui Zou, Katerina Toropova, Anthony Roberts, Samara Reck-Peterson and Andres Leschziner designed the experiments. Sirui Zou performed and analyzed FRET experiments and single-molecule assays. Katerina Toropova performed and analyzed 3D EM-reconstitution, ATPase activity assay and mutagenesis identifying the interface of dynein-Lis1 complex. William Redwine performed and analyzed in-vivo spindle oscillation assay. Brian Goodman wrote the tracking scripts to analyze the data of spindle oscillation assay. This work was published in: Lis1 regulates dynein by sterically blocking its mechanochemical cycle, *eLIFE* 3:e03372 (2014).

Supplementary figures and tables

Figure A2.1 Three-dimensional (3D) classification and refinement of the dynein and dynein-Lis1 reconstructions

(a) SDS-PAGE of dynein and Lis1, affinity purified from *S. cerevisiae*. **(b)** Comparison between re-projections of the dynein and dynein-Lis1 reconstructions and the best-matching reference-free class averages (no nucleotide conditions). **(c)** Fourier Shell Correlation plots for all EM maps presented. The plots are shown as a function of resolution (1/frequency). The thresholds for the 0.5 FSC and 0.143 FSC criteria are shown. **(d)** and **(e)** Class averages of monomeric dynein in complex with dimeric (d) or monomeric (e) Lis1, with a schematic representation alongside each. **(f – h)** 3D classification of linker positions in the dynein-Lis1 (no nucleotide) dataset. **(f)** A reconstruction using the entire dataset without sorting out linker conformations. The N-terminus of the linker is mostly averaged out in this map. **(g)** 3D class average of a subset of dynein motors whose linkers are located on the AAA5 proximal side of Lis1. The purple arrow points to the N-terminus of the linker. **(h)** The linker density from (g) was overlaid on the dynein-Lis1 structure (Figure 3.2A) to highlight the different positions adopted by the linker in the presence of Lis1. The purple and grey arrows point to the N-terminus of the linker domain in the two conformations. The Lis1 density is indicated in all three maps. **(i)** A side view of the dynein motor domain in surface representation with the linker domain colored by conservation (100%, purple; 11%, white). The alignment was carried out using cytoplasmic dynein from the following species: *M. musculus, H. sapiens, S. cerevisiae, C. albicans, A, fumigatus, A. nidulans, D. discoideum, D. melanogaster, and C. elegans* using Muscle (Edgar, 2004). For orientation, a cartoon representation of the view is shown bottom right. The truncation site for the short linker dynein is marked with a dashed line and scissors (see Figure 3.7).

Figure A2.1 (continued)

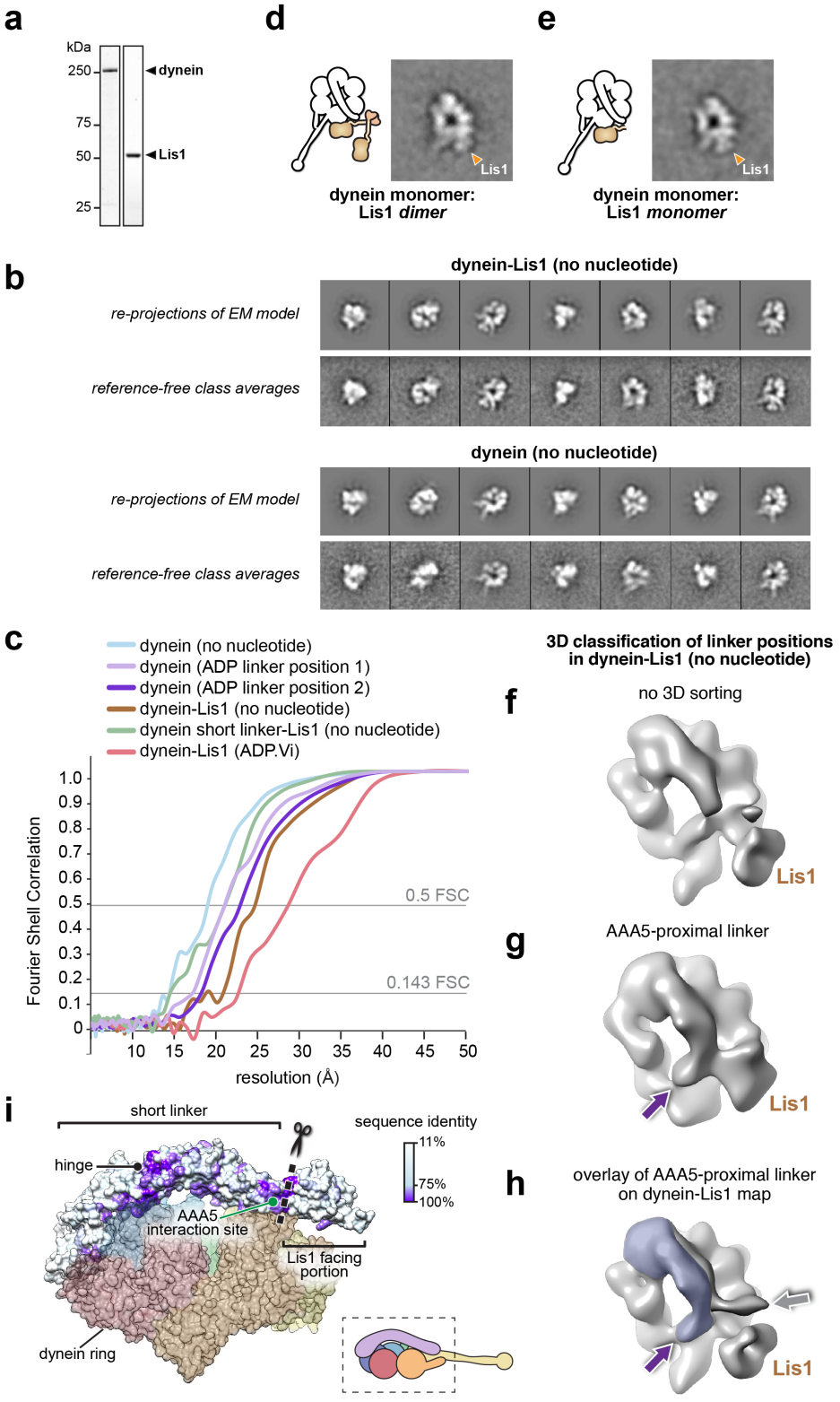

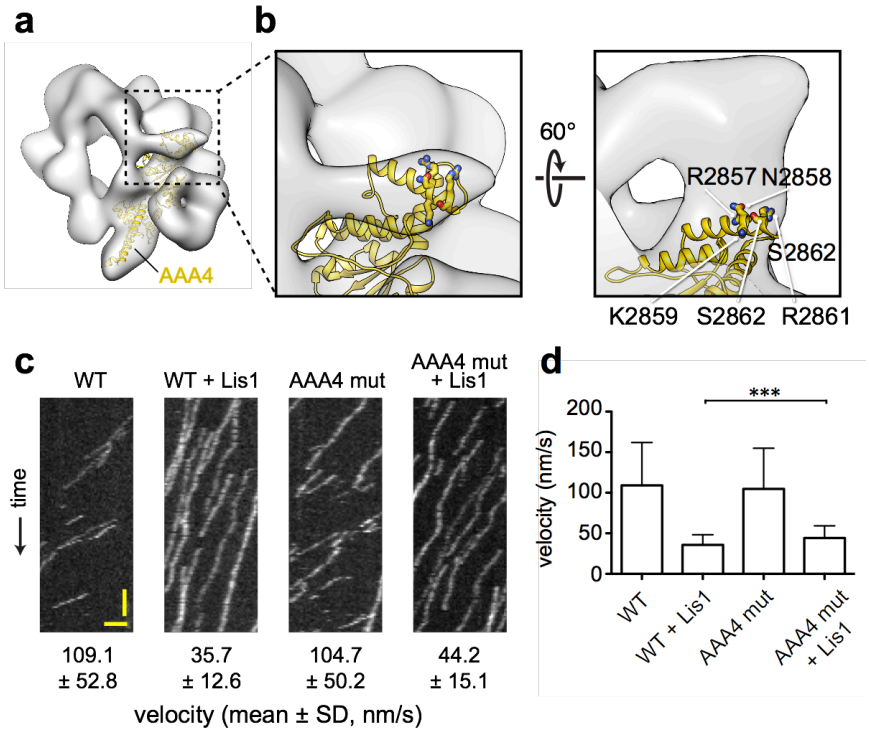

Figure A2.2 The linker's displaced position in the presence of Lis1 does not appear to involve a specific interaction with AAA4

(a) Zoomed out view of dynein-Lis1; only the portion of the crystal structure corresponding to AAA4 is displayed, in yellow (PDB ID: 4AKG (Schmidt et al., 2012)). **(b)** Close-up of the N-terminal portion of the linker (left), and a view rotated by 60º (right). The latter shows a density connecting the linker and AAA4. Residues in a AAA4 helix that are located in the density connecting AAA4 to the linker are shown in atomic representation, colored by element and labeled. **(c)** Kymographs of *in vitro* motility experiments with TMR-labeled wild-type GST-dynein$_{331kDa}$ or mutant GST-dynein$_{331kDa}$ with the 5 residues labeled in (c) changed to alanine (AAA4 mut). Assays were performed with dynein alone or in the presence of 200 nM Lis1. Horizontal scale bar = 2 µm, vertical = 30 s. **(d)** Histogram of mean velocities for each experiment ± S.D., N = 228 – 612, ***p < 0.0001.

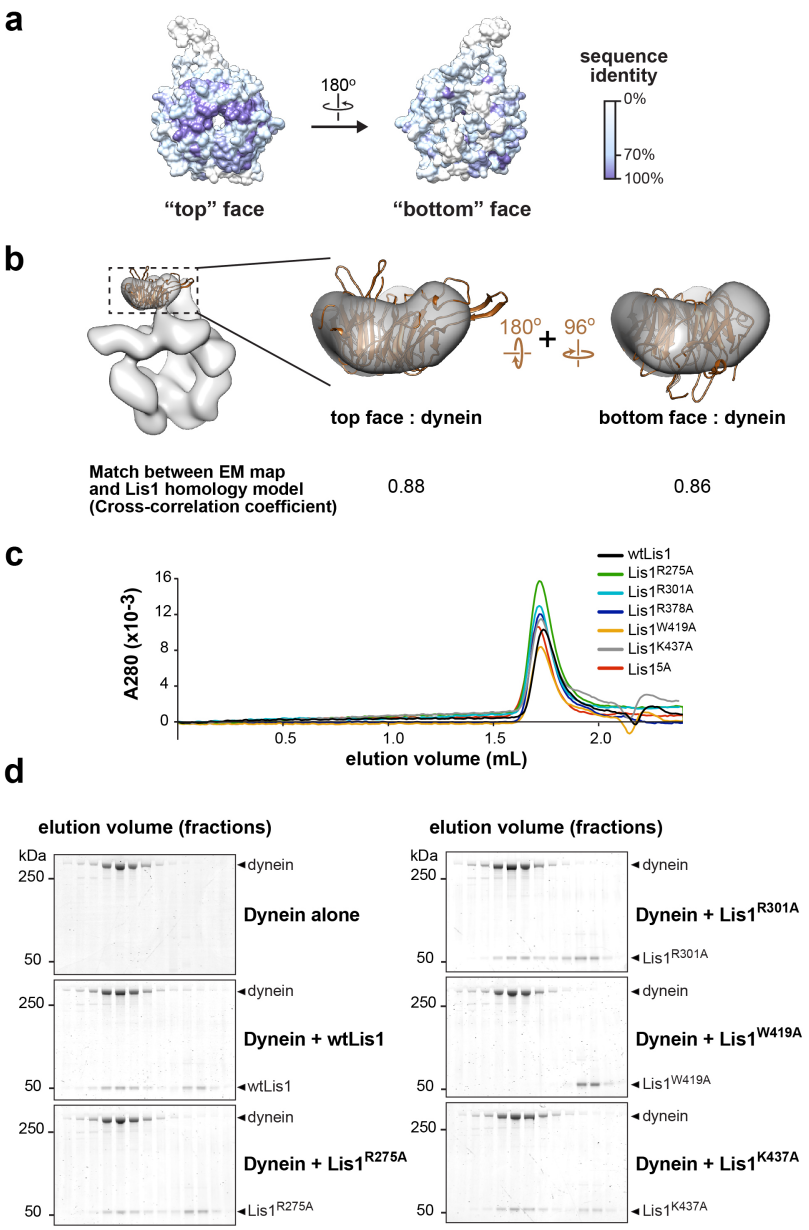

Figure A2.3 Probing of the proposed dynein-Lis1 interface by mutagenesis

(a) Sequence identity (100%, purple; 0%, white) mapped onto the Lis1 homology model. The alignment was carried out with the following species: *M. musculus, H. sapiens, S. cerevisiae, A. nidulans, D. discoideum, D. melanogaster, X. laevis, C. elegans,* and *D. rerio* using Muscle (Edgar, 2004). **(b)** The Lis1 homology model was docked into the dynein-Lis1 map in two possible orientations, with either the top (middle panel) or bottom (right panel) face interacting with dynein. The rotations relating the two orientations are indicated. A cross-correlation coefficient calculated for each fit is shown below the structures. These coefficients were calculated between the Lis1 EM density and the homology model filtered to the same resolution (21Å)(as implemented in UCSF Chimera (Pettersen et al., 2004)). **(c)** Size-exclusion traces for wild-type and Lis1 mutants. **(d)** SDS-PAGE of size-exclusion fractions for GST-dynein$_{331kDa}$ (shortened to 'dynein' in the figure) mixed with wild-type of mutant Lis1.

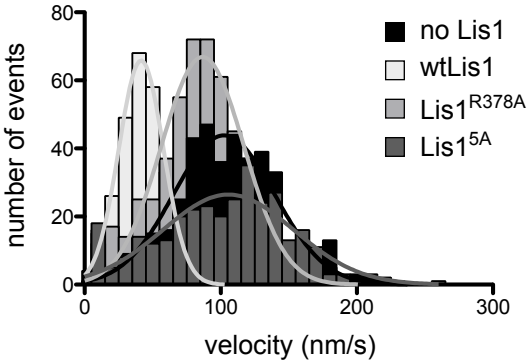

Figure A2.4 Velocity distributions for dynein alone or in the presence of wild-type or mutant Lis1

Histogram showing the velocity distribution of single TMR-labeled GST-dynein$_{331kDa}$ molecules in the absence of Lis1 (black) and with 200 nM wild-type Lis1 (light grey), Lis1^{R378A} (medium grey) and Lis1^{5A} (dark grey). Velocity distributions were unimodal and could be well fit by a single Gaussian (R^2 values between 0.8221 and 0.9937).

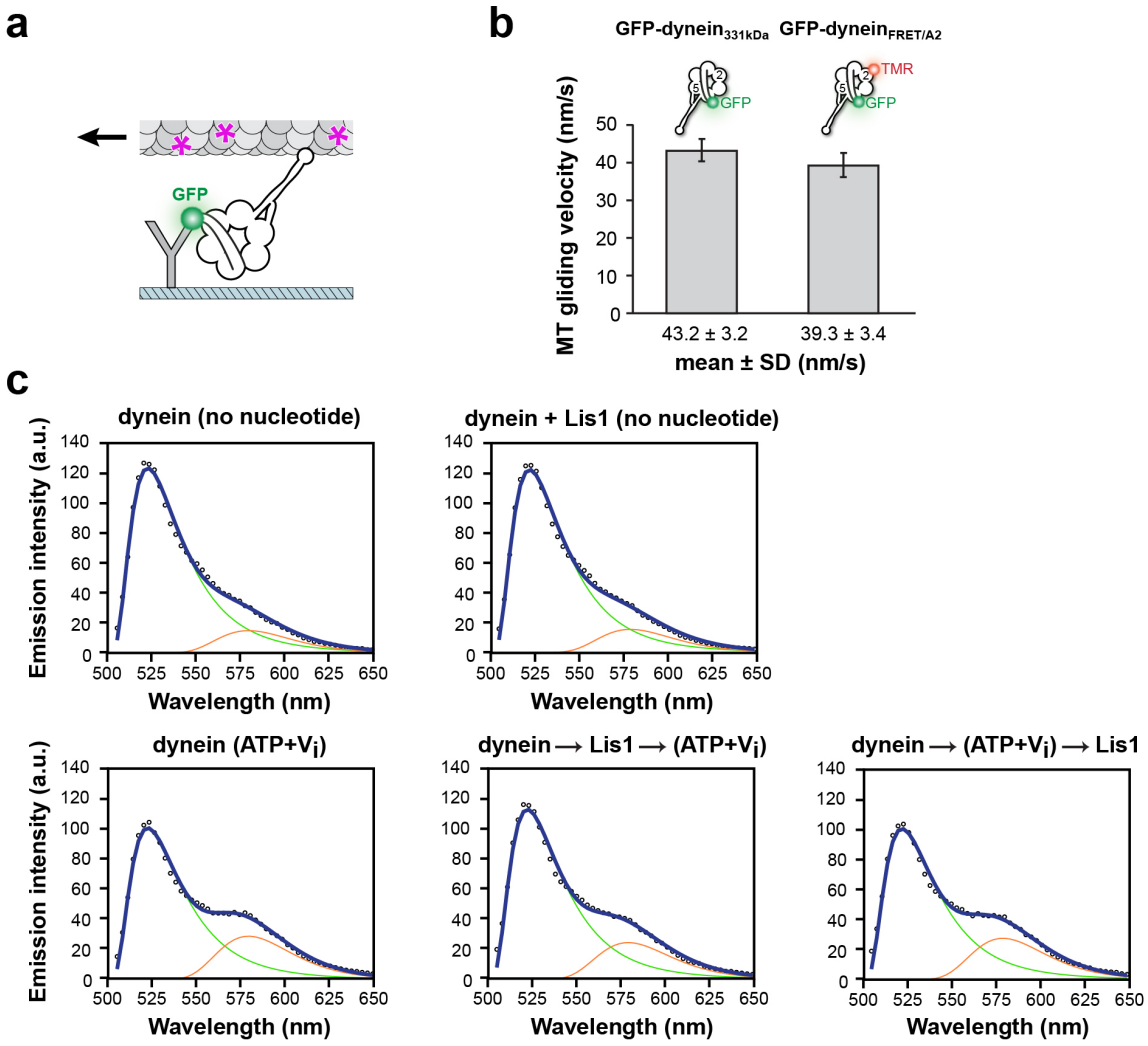

Figure A2.5 FRET analysis of linker movement towards the pre-powerstroke position in the presence of Lis1

(a) Diagram of a microtubule-gliding assay. Monomeric GFP-dynein molecules are immobilized on the coverslip via anti-GFP antibodies (Y shape). Dynein-driven gliding of fluorescently labeled (purple asterisks) microtubules is visualized using TIRF microscopy. **(b)** A dynein FRET construct with CoA-TMR inserted into its AAA2 domain (GFP-dynein$_{FRET/A2}$) has a microtubule gliding activity similar to that of a control construct lacking it (GFP-dynein$_{331kDa}$). **(c)** Fitted FRET emission spectra for dynein in different nucleotide conditions (no nucleotide or 200 μM ATP+V_i) and with 0 nM or 840 nM Lis1. Arrows indicate the order of addition for the last two plots. Emission spectra for eGFP and TMR used for the fit are shown as green and red traces, respectively.

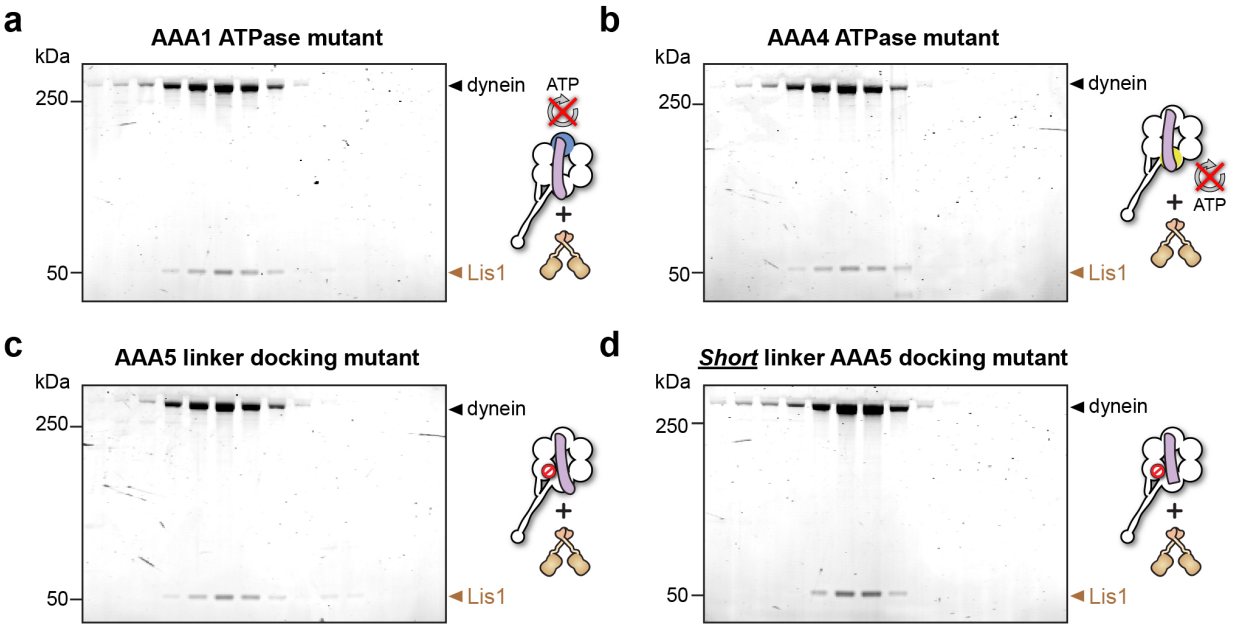

Figure A2.6 Lis1 binds to dynein ATPase mutants

(a – d) SDS-PAGE of fractions eluted from size exclusion chromatography runs of Lis1 mixed with each of the dynein constructs used in the ATPase assays. Lis1 co-elutes with all of the constructs.

Figure A2.7 The short linker dynein construct shows robust motility, hydrolyzes ATP and binds Lis1

(a) Single-molecule motility assays. Kymographs of GST-dimerized full-length and short linker dyneins. Horizontal scale bar = 2 μm, vertical = 30 s **(b)** Velocity and run length for short linker and full-length linker dyneins. Similar values are seen for the two constructs, N = 265 – 333. **(c)** SDS-PAGE of elution fractions from size exclusion chromatography of monomeric short linker dynein mixed with Lis1. Lis1 co-migrates with short linker dynein. **(d)** Microtubule-stimulated ATPase activity of short linker dynein with either wild-type AAA+ modules (left) or with mutations (K3438E, R3445E, F3446D) that prevent linker docking at AAA5 (Schmidt et al., 2012)(right). ATPase traces are of dynein alone (light green) or in the presence of 140 nM Lis1 (brown). Measurements were done in triplicate (wild type) or duplicate (AAA5 mutant) from one preparation. Diagrams of the dynein constructs used to generate the plots are shown next to them. **(e)** Addition of buffer lacking ATP to flow chambers containing TMR-labeled full-length or short linker dynein does not cause microtubule detachment. Scale bar = 5 s. **(f)** The short linker construct used in Figure 5 contains an N-terminal GFP connected to the short linker via 3 HA tags. We expected the GFP to be flexible in its location relative to dynein based on previous EM studies (Roberts et al., 2009) and the fact that it is averaged out in our 3D reconstruction of dynein (Figure 3.2B). However to rule out interference from GFP, we also carried out the microtubule release assays with a GFP-less construct. We observed the same results: addition of ATP to GFP-less dyneins in the presence of 300 nM Lis1 caused short-linker dyneins to release from the microtubule while full-length dyneins remain attached. Scale bar = 5 s. **(g)** Quantification of the kymographs in (f), showing the duration of microtubule attachment of full-length (light brown) or short linker (dark brown) dynein molecules after addition of ATP, in the presence of 300 nM Lis1. Data was binned into 1 s intervals and the histograms show alternating full-length and short linker dynein bars. Rare attachments longer than 10 s, were excluded from the analysis and plot, N = 141 – 197.

Figure A2.7 (Continued)

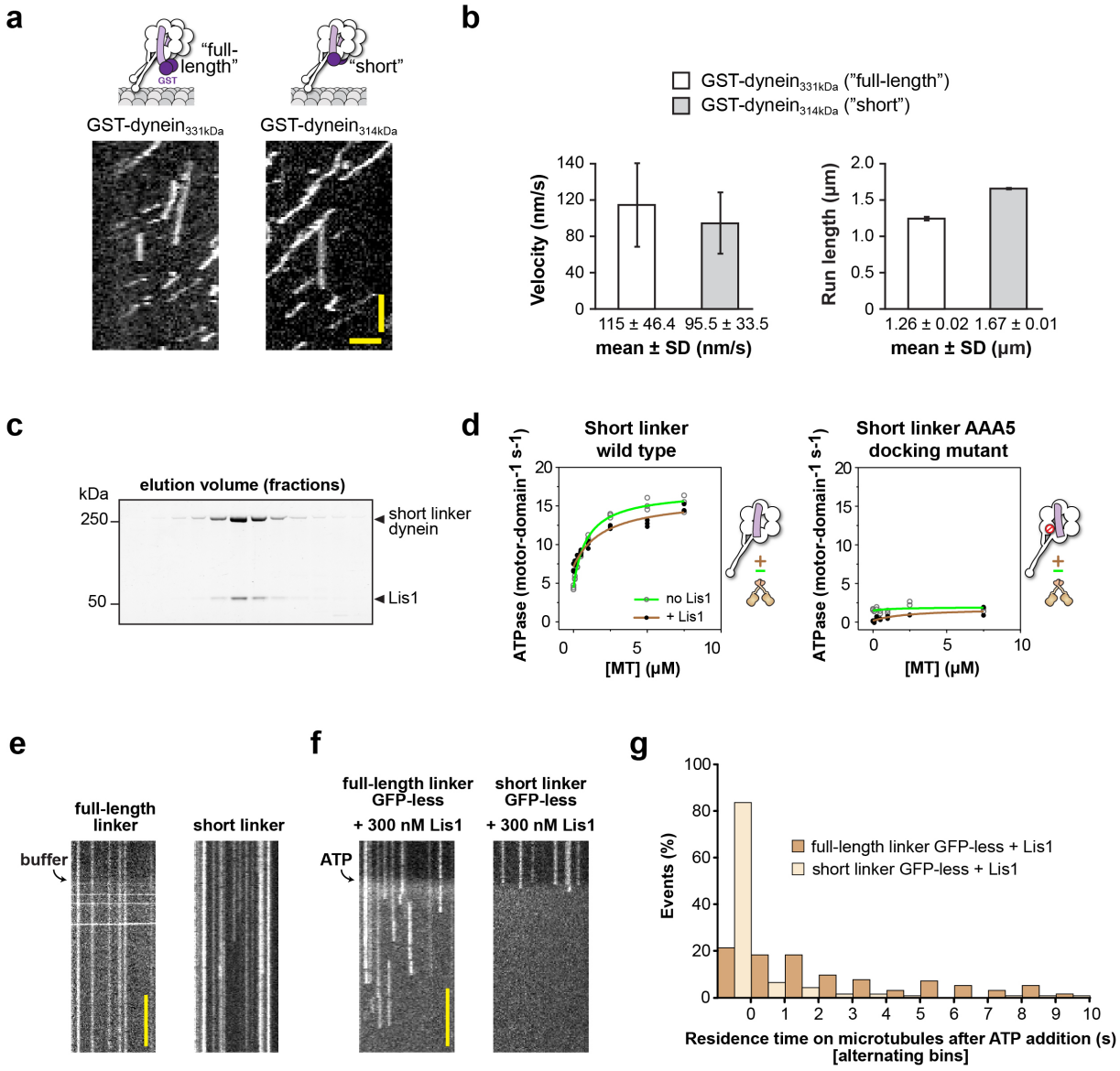

Table A2.1 Yeast strains

Strain	Genotype	Figure(s) Reference
RPY753	MATa, *his3-11,15, ura3-1, leu2-3,112, ade2-1, trp1-1, pep4Δ::HIS5, prb1Δ, P_{GAL1}-ZZ-Tev-GFP-3xHA-GST-DYN1$_{331\ kDa}$-gs-DHA, pac1Δ::URA3, ndl1Δ::cgLEU2*	Figure 2, Figure 2 – figure supplement 1,2, Figure 5 – figure supplement 1 Huang et al., 2012
RPY816	MATa, *his3-11,15, ura3-1, leu2-3,112, ade2-1, trp1-1, pep4Δ::HIS5, prb1Δ, P_{GAL1}-ZZ-Tev-PAC1, dyn1Δ::cgLEU2, ndl1Δ::Hygro^R*	Figure 1 – 5, Figure 2 – figure supplement 1,2, Figure 1,4,5 – figure supplement 1 Julie Huang, Harvard Medical
RPY842	MATa, *his3-11,15, ura3-1, leu2-3,112, ade2-1, trp1-1, pep4Δ::HIS5, prb1Δ, P_{GAL1}-ZZ-Tev-PAC1-g-1xFLAG-ga-SNAP-Kan^R, dyn1Δ::cgLEU2, ndl1Δ::Hygro^R*	Figure 3,5, Figure 3,5 – figure supplement 1 Huang et al., 2012
RPY844	MATa, *his3-11,15, ura3-1, leu2-3,112, ade2-1, trp1-1, pep4Δ::HIS5, prb1Δ, PAC11-13xMYC-TRP1, P_{GAL1}-ZZ-Tev-GFP-3xHA-DYN1$_{331\ kDa}$, pac1Δ::Hygro^R*	Figure 1,4, Figure 1,3 – figure supplement 1 Huang et al., 2012
RPY1198	MATa, *his3-11,15, ura3-1, leu2-3,112, ade2-1, trp1-1, pep4Δ::HIS5, prb1Δ, PAC11-13xMYC-TRP1, P_{GAL1}-ZZ-Tev-GFP-3xHA-DYN1$_{331\ kDa}$-gs-DHA-Kan^R, pac1Δ::Hygro^R*	Figure 5, Figure 5 – figure supplement 1 Huang et al., 2012
RPY1245	MATa, *ura3-52, lys2-801, leu2-Δ1, his3-Δ200, trp1-Δ63, SPC110-GFP::TRP1, HXT1-tdTomato::HIS3*	Figure 2 Jeff Moore, University of Colorado

Table A2.1 (Continued)

RPY1248	MATa, *ura3-52, lys2-801, leu2-Δ1, his3-Δ200, trp1-Δ63, SPC110-GFP::TRP1, HXT1-tdTomato::HIS3, dyn1Δ::URA3*	Figure 3.3 This work
RPY1302	MATa, *his3-11,15, ura3-1, leu2-3,112, ade2-1, trp1-1, pep4Δ::HIS5, prb1Δ, PAC11-13xMYC-TRP1, P_{GAL1}-ZZ-Tev-$DYN1_{331\ kDa}$, pac1Δ::$Hygro^R$*	Figure 3.1-2, 3.4-5 This work
RPY1400	MATa, *his3-11,15, ura3-1, leu2-3,112, ade2-1, trp1-1, pep4Δ::HIS5, prb1Δ, PAC11-13xMYC-TRP1, P_{GAL1}-ZZ-Tev-GFP-3xHA-$DYN1_{331\ kDa}$-L2441ybbR, pac1Δ::$Hygro^R$*	Figure 3.4-5, Figure A2.5 This work
RPY1422	MATa, *his3-11,15, ura3-52, leu2-3,112, ade2-1, trp1-1, pep4Δ::HIS5, prb1Δ, P_{GAL1}-ZZ-Tev-GFP-3xHA-$DYN1_{314\ kDa}$-gs-DHA, pac1Δ::$Hygro^R$*	Figure 3.6-7 Figure A2.6-7 This work
RPY1436	MATa, *his3-11,15, ura3-52, leu2-3,112, ade2-1, trp1-1, pep4Δ::HIS5, prb1Δ, PAC11-13xMYC-TRP1, P_{GAL1}-ZZ-Tev-$DYN1_{314\ kDa}$, pac1Δ::$Hygro^R$*	Figure 3.7 This work
RPY1439	MATa, *his3-11,15, ura3-1, leu2-3,112, ade2-1, trp1-1, pep4Δ::HIS5, prb1Δ, P_{GAL1}-ZZ-Tev-GFP-3xHA-GST-$DYN1_{314\ kDa}$-gs-DHA-Kan^R, pac1Δ:URA3, ndl1Δ::cgLEU2*	Figure A2.7 This work

Table A2.1 (Continued)

RPY1509	MATa, *his3-11,15, ura3-1, leu2-3,112, ade2-1, trp1-1, pep4Δ::HIS5, prb1Δ, PAC11-13xMYC-TRP1,* P_{GAL1}*-ZZ-Tev-*$DYN1_{331\ kDa}$*-gs-DHA-*Kan^R*, pac1Δ::*$Hygro^R$	Figure A2.7 This work
RPY1510	MATa, *his3-11,15, ura3-1, leu2-3,112, ade2-1, trp1-1, pep4Δ::HIS5, prb1Δ, PAC11-13xMYC-TRP1,* P_{GAL1}*-ZZ-Tev-*$DYN1_{314\ kDa}$*-gs-DHA-*Kan^R*, pac1Δ::*$Hygro^R$	Figure A2.7 This work
RPY1523	MATa, *ura3-52, lys2-801, leu2-Δ1, his3-Δ200, trp1-Δ3, SPC110-GFP::TRP1, HXT1-tdTomato::HIS3, pac1Δ::URA3*	Figure 3.3 This work
RPY1524	MATa, *ura3-52, lys2-801, leu2-Δ1, his3-Δ200, trp1-Δ63, SPC110-GFP::TRP1, HXT1-tdTomato::HIS3,* $PAC1^{R378A}$	Figure 3.3 This work
RPY1525	MATa, *ura3-52, lys2-801, leu2-Δ1, his3-Δ200, trp1-Δ63, SPC110-GFP::TRP1, HXT1-tdTomato::HIS3,* $PAC1^{R275A,R301A,R378A,W419A,K437A}$	Figure 3.3 This work
RPY1543	MATa, *his3-11,15, ura3-1, leu2-3,112, ade2-1, trp1-1, pep4Δ::HIS5, prb1Δ,* P_{GAL1}*-ZZ-Tev-*$PAC1^{R275A}$*, dyn1Δ::cgLEU2, ndl1Δ::*$Hygro^R$	Figure A2.3 This work

Table A2.1 (Continued)

RPY1544	MATa, *his3-11,15, ura3-1, leu2-3,112, ade2-1, trp1-1, pep4Δ::HIS5, prb1Δ, P_{GAL1}-ZZ-Tev-PAC1^{R378A}, dyn1Δ::cgLEU2, ndl1Δ::Hygro^{R}*	Figure 3.3, Figure A2.3-4 This work
RPY1545	MATa, *his3-11,15, ura3-1, leu2-3,112, ade2-1, trp1-1, pep4Δ::HIS5, prb1Δ, P_{GAL1}-ZZ-Tev-PAC1^{W419A}, dyn1Δ::cgLEU2, ndl1Δ::Hygro^{R}*	Figure A2.3 This work
RPY1546	MATa, *his3-11,15, ura3-1, leu2-3,112, ade2-1, trp1-1, pep4Δ::HIS5, prb1Δ, P_{GAL1}-ZZ-Tev-PAC1^{K437A}, dyn1Δ::cgLEU2, ndl1Δ::Hygro^{R}*	Figure A2.3 This work
RPY1547	MATa, *his3-11,15, ura3-1, leu2-3,112, ade2-1, trp1-1, pep4Δ::HIS5, prb1Δ, P_{GAL1}-ZZ-Tev-PAC1^{R275A,R301A,R378A,W419A,K437A}, dyn1Δ::cgLEU2, ndl1Δ::Hygro^{R}*	Figure 3.3, Figure A2.3-4 This work
RPY1548	MATa, *his3-11,15, ura3-1, leu2-3,112, ade2-1, trp1-1, pep4Δ::HIS5, prb1Δ, P_{GAL1}-ZZ-Tev-PAC1^{R301A}, dyn1Δ::cgLEU2, ndl1Δ::Hygro^{R}*	Figure A2.3 This work
RPY1553	MATa, *his3-11,15, ura3-1, leu2-3,112, ade2-1, trp1-1, pep4Δ::HIS5, prb1Δ, PAC11-13xMYC-TRP1, P_{GAL1}-ZZ-Tev-GFP-3xHA-DYN1$_{331\ kDa}^{E1849Q}$, pac1Δ::Hygro^{R}*	Figure 3.6 Figure A2.6 This work

Table A2.1 (Continued)

RPY1554	MATa, *his3-11,15, ura3-1, leu2-3,112, ade2-1, trp1-1, pep4Δ::HIS5, prb1Δ, PAC11-13xMYC-TRP1, P_{GAL1}-ZZ-Tev-GFP-3xHA-DYN1$_{331\ kDa}^{E2819Q}$, pac1Δ::Hygro^R*	Figure 3.6, Figure A2.6 This work
RPY1555	MATa, *his3-11,15, ura3-52, leu2-3,112, ade2-1, trp1-1, pep4Δ::HIS5, prb1Δ, P_{GAL1}-ZZ-Tev-GFP-3xHA-DYN1$_{314\ kDa}^{K3438E,R3445E,F3446D}$-gs-DHA, pac1Δ::Hygro^R*	Figure A2.6-7 This work
RPY1557	MATa, *his3-11,15, ura3-1, leu2-3,112, ade2-1, trp1-1, pep4Δ::HIS5, prb1Δ, PAC11-13xMYC-TRP1, P_{GAL1}-ZZ-Tev-GFP-3xHA-DYN1$_{331\ kDa}^{K3438E,R3445E,F3446D}$-gs-DHA-Kan^R, pac1Δ::Hygro^R*	Figure 3.6, Figure A2.6 This work
RPY1623	MATa, *his3-11,15, ura3-1, leu2-3,112, ade2-1, trp1-1, pep4Δ::HIS5, prb1Δ, P_{GAL1}-ZZ-Tev-GFP-3xHA-GST- DYN1$_{331\ kDa}^{R2857A,N2858A,K2859A,R2861A,S2862A}$-gs-DHA, pac1Δ::URA3, ndl1Δ::cgLEU2*	Figure A2.2 This work

DYN1, PAC11, PAC1 and NDL1 encode the dynein heavy chain, dynein intermediate chain, Lis1 and Nudel orthologs, respectively. *DHA*, *SNAP* and *ybbR* refer to the HaloTag (Promega), SNAP-tag (NEB) and ybbR tag (Yin et al., 2005), respectively. *TEV* indicates a Tev protease cleavage site. P_{GAL1} denotes the galactose promoter, which was used for inducing strong expression of Lis1 and dynein motor domain constructs. Genes encoding proteases Pep4 and Prb1 were deleted as noted. Amino acid spacers are indicated by *g* (glycine), *ga* (glycine-alanine), and *gs* (glycine-serine).

Table A2.2 Dynein:Lis1 ratios in complexes purified by size-exclusion chromatography

In relation to Figure 3.3 and Figure A2.3. Fractions were run on SDS-PAGE, stained with SYPRO red and the bands corresponding to GST-dynein$_{331kDa}$ and wild-type/mutant Lis1 were quantified using ImageJ. The quantification was done using three adjacent lanes corresponding to the peak from size-exclusion. Values are averages of the three lanes ± SD. The ratio for each mutant normalized against that of wild-type Lis1 is also shown.

	GST-dynein$_{331kDa}$	Lis1	Lis1 (normalized to WT ratio)
WT Lis1	0.82 ± 0.01	0.18 ± 0.01	1.00
Lis1^{R275A}	0.85 ± 0.01	0.15 ± 0.01	0.80
Lis1^{R301A}	0.88 ± 0.01	0.12 ± 0.01	0.62
Lis1^{R378A}	1.00 ± 0.00	0.00 ± 0.00	0.00
Lis1^{W419A}	1.00 ± 0.00	0.00 ± 0.00	0.00
Lis1^{K437A}	0.85 ± 0.01	0.15 ± 0.01	0.80
Lis1^{5A}	1.00 ± 0.00	0.00 ± 0.00	0.00

Table A2.3 ATPase assay rate measurements.

Sample	K_m(MT)(μM)	k_{basal} (motor domain^{-1}.$^{s-1}$)	k_{cat} (motor domain^{-1}.$^{s-1}$)
Full-length linker	1.06 ± 0.16	3.51 ± 0.31	16.75 ± 0.49
+ Lis1	1.09 ± 0.20	4.36 ± 0.30	15.06 ± 0.49
Short linker	0.92 ± 0.10	4.45 ± 0.22	16.98 ± 0.32
+ Lis1	2.05 ± 0.44	7.14 ± 0.21	16.12 ± 0.61
Full-length linker, AAA4 ATPase mutant (E2819Q)	1.55 ± 0.14	4.53 ± 0.17	18.80 ± 0.38
+ Lis1	1.10 ± 0.15	4.60 ± 0.19	13.93 ± 0.31

Data were fit to the following equation: $k_{obs} = (k_{cat} - k_{basal}) - [MT]/(K_m(MT) + [MT]) + k_{basal}$. K_m(MT) is the microtubule concentration that gives half-maximal activation. Values are the averages of triplicate readings ± SE of the fit.

References

Edgar, R.C. (2004). MUSCLE: multiple sequence alignment with high accuracy and high throughput. Nucleic Acids Res *32*, 1792–1797.

Huang, J., Roberts, A.J., Leschziner, A.E., and Reck-Peterson, S.L. (2012). Lis1 acts as a “clutch” between the ATPase and microtubule-binding domains of the dynein motor. Cell *150*, 975–986.

Pettersen, E.F., Goddard, T.D., Huang, C.C., Couch, G.S., Greenblatt, D.M., Meng, E.C., and Ferrin, T.E. (2004). UCSF Chimera--a visualization system for exploratory research and analysis. J Comput Chem *25*, 1605–1612.

Roberts, A.J., Numata, N., Walker, M.L., Kato, Y.S., Malkova, B., Kon, T., Ohkura, R., Arisaka, F., Knight, P.J., Sutoh, K., et al. (2009). AAA+ Ring and linker swing mechanism in the dynein motor. Cell *136*, 485–495.

Schmidt, H., Gleave, E.S., and Carter, A.P. (2012). Insights into dynein motor domain function from a 3.3-Å crystal structure. Nat Struct Mol Biol *19*, 492–497.

Yin, J., Straight, P.D., McLoughlin, S.M., Zhou, Z., Lin, A.J., Golan, D.E., Kelleher, N.L., Kolter, R., and Walsh, C.T. (2005). Genetically encoded short peptide tag for versatile protein labeling by Sfp phosphopantetheinyl transferase. Proc Natl Acad Sci U S A *102*, 15815–15820.